

# SAPO-11 as a catalyst for the production of chemicals from methanol

Diamanta Ibishi



[Master Thesis]  
Department of Chemistry  
60 credits

Faculty of mathematics and natural science

UNIVERSITY OF OSLO

November 2019



## Acknowledgments

In the work of my masters degree, I have been introduced to two different fields of science. I spent the first year in the electrochemistry group before deciding to write my thesis in the catalysis group. It has been a joyful experience and I want to thank the entire catalysis group as well as the electrochemistry group for a good work environment, fun lunch break talks, and nice get-togethers.

I would especially like to thank my main supervisor for the thesis, Prof. Stian Svelle. During my thesis in catalysis, you have taught me the importance of applying good systematics and precision to research, and not to forget the challenging skill of being patience in the lab. You have motivated me to dear to be creative and choose pathways of my own. I would also like to thank Co-supervisor Prof. Karl Petter Lillerud for providing support and excellent training in HSE whenever needed. To Co-supervisor Prof. Unni Olsbye, a special thanks for all support and suggesting sending me to the Winter school on innovation, catalysis, and sustainability in Bardonecchia. I appreciate all of your acknowledgments throughout this thesis. And when times were tough, the advice from all of you was plenty.

From the catalysis group I would like to give a special thanks to Daniel Firth and Chris Affolter for always wanting to discuss both scientific and other fun topics in the lab. I would like to thank David Wragg for excellent XRD training, Martin Jensen for SEM training, Chris Affolter for TGA training, Sharmala Aravinthan for training in both N<sub>2</sub> adsorption and MP-AES, Andrea Lazzarini and Chiara Negri for IR-training and interpretation, Georgios Zopoulos and Jingxiu Xie for training and supervision on catalytic testing. You guys are great.

I also wish to thank Prof. Truls Norby from electrochemistry. Even though you have not been a part of this particular thesis, you provided me with excellent supervision, great scientific inspiration and support during my time in the electrochemistry group.

Lastly, I would like to thank my family and friends for reminding me there is a life outside of the chemistry world. Thank you for all support and for not minding getting strange SEM images of my synthesized particles as Christmas gifts. You are the best and I value you in a big deal!

© Forfatter

År

Tittel

Forfatter

<http://www.duo.uio.no/>

Trykk: Reprosentralen, Universitetet i Oslo

# Abstract

The conversion of methanol to olefins reaction has been tested over synthesized and commercial SAPO-11, where the supplied and synthesized materials inhibit different morphology, surface area, and acid sites density. The synthesized samples were synthesized with the hydrothermal method and the effect of static and rotational crystallization in a temperature range of 150 to 180 °C were investigated for prepared synthesis mixtures. All samples were characterized by PXRD, SEM, TGA, N<sub>2</sub> physisorption, MP-AES, EDS, and CO-FTIR. The results obtained, indicated a systematic decrease in the measured diameter (μm) for the synthesized SAPO-11 aggregates. The trend was reported as a function of increased temperature under both static and rotational conditions. This screening also revealed that the most uniform SAPO-11 aggregates were obtained at high crystallization temperature. Elemental analysis showed the silicon content for the as-synthesized SAPO-11 was 10 times lower than the supplied SAPO-11. This finding was linked to the difference in catalytic activity observed between commercial SAPO-11 and synthesized SAPO-11 at 180 °C.

Performance test revealed methanol to olefins conversion was feasible for both supplied and synthesized samples. The supplied SAPO-11 sample showed an initial higher methanol conversion towards hydrocarbon formation, whilst the in-house synthesized samples inhibited a similar behavior at lower conversion percentages. All tested samples obtained highest selectivities toward C<sub>5+</sub> hydrocarbons. Nevertheless, synthesized samples proved to be more stable and selective towards the C<sub>2</sub>-C<sub>4</sub> hydrocarbons compared to the commercial sample.

# List of abbreviations used in this thesis

AEL	IZA code for zeotype framework of SAPO-11
a.u	Arbitraty units
ALPO	Aluminophosphate
BET	Brunauer-Emmett Teller
BSE	Backscattered electrons
CHA	IZA code for the zeotype framework of Chabazite
EDS	Energy dispersive X-ray spectroscopy
DME	Dimethyl ether
FT-IR	Fourier transform infrared spectroscopy
GC-MS	Gas chromatography
GOF	Goodness of fit
MeOH	Methanol
MS	Mass spectrometry
MTO	Methanol to olefins
PXRD	Powder X-ray diffraction
R <sub>WP</sub>	The weighed profile
SAPO	Silicoaluminophosphate
SE	Secondary electrons
SEM	Scanning electron microscopy

SM	Substitution mechanism
TGA	Thermogravimetric analysis
TOS	Time on stream
WHSV	Weight hourly space velocity

# Contents

Acknowledgments .....	III
Abstract .....	V
List of abbreviations used in this thesis .....	VI
1 Project motivation and aim .....	1
2 Introduction .....	5
2.1 Microporous materials .....	5
2.2 What are zeolites and zeotypes? .....	5
2.3 Historical development of zeolites .....	6
2.4 Defining the framework.....	8
2.5 Properties .....	11
2.5.1 Acid sites .....	11
2.5.2 Shape selectivity.....	13
2.6 Catalysis and application of zeolitic materials .....	15
2.6.1 SAPO-11 as a heterogeneous catalyst for the conversion of methanol to olefins 19	
3 Theory and Methodology .....	20
3.1 Kinetics and thermodynamics of crystal growth .....	20
3.1.1 Nucleation theory .....	20
3.1.2 Crystal growth theory – Conventional and recent published theory .....	22
3.1.3 Nucleation and growth in zeolitic materials.....	22
3.2 Zeolite synthesis .....	24
3.2.1 Hydrothermal method and HSE aspects.....	24
3.2.2 Theoretical effect of important synthesis parameters .....	26
3.2.3 Published work on synthesis of SAPO-11 .....	28
3.3 Theory of characterization techniques.....	31
3.3.1 Powder X-ray diffraction .....	31



3.3.2	Scanning electron microscopy .....	32
3.3.3	Thermogravimetric analysis .....	35
3.3.4	Gas–physisorption .....	35
3.3.5	Fourier transformed Infrared spectroscopy .....	37
3.3.6	Microwave Plasma atomic emission spectroscopy .....	39
3.3.7	Simulations for surface area determination.....	40
4	Experimental .....	43
4.1	Methodology for the screening of SAPO-11 synthesis .....	43
4.1.1	Determining a method for synthesis approach.....	43
4.1.2	Initial synthesis approach .....	43
4.1.3	Modified synthesis approach – tuning the kinetics .....	45
4.1.4	Calcination .....	49
4.2	Characterization.....	50
4.2.1	Powder X-ray diffraction .....	50
4.2.2	Scanning electron microscopy .....	50
4.2.3	Thermogravimetric analysis .....	50
4.2.4	N <sub>2</sub> -physisorption.....	51
4.2.5	Fourier transformed infrared spectroscopy .....	51
4.2.6	Microwave plasma atomic emission spectroscopy .....	51
4.3	Catalytic testing for methanol to olefins conversion.....	52
4.3.1	Experimental setup.....	52
4.3.2	Test conditions .....	53
5	Results .....	56
5.1	Mapping the synthesis route for the synthesis of SAPO-11 .....	56
5.1.1	Synthesis methodology .....	56
5.1.2	Yield calculations for the modified synthesis approach.....	56
5.2	Standard Characterization.....	58

5.2.1	Powder X-ray diffraction .....	58
5.2.2	Scanning electron microscopy .....	63
5.2.3	Size distribution.....	69
5.2.4	Calcination .....	71
5.2.5	Thermogravimetric analysis.....	74
5.3	Selective characterization for acidity and framework .....	75
5.3.1	N <sub>2</sub> - physisorption and surface area simulations .....	75
5.3.2	Elemental analysis with MP-AES and EDS.....	78
5.3.3	CO probing with FT-IR.....	79
5.4	Performance tests.....	81
5.4.1	Activity.....	81
5.4.2	Selectivities .....	82
6	Discussion .....	84
6.1	Screening of the synthesis route for SAPO-11 .....	84
6.2	Acidity and framework aspects of the SAPO-11 materials.....	87
6.3	Performance tests for the MTO reaction .....	90
7	Conclusion.....	95
8	Perspectives.....	97
	Appendix .....	98
	Appendix A - Molar ratios calculation.....	98
	Appendix B – Initial synthesis of SAPO – 11.....	100
	Appendix C – Yield Calculations.....	102
	Appendix D – Reproducibility and impurities .....	105
	References .....	107





# 1 Project motivation and aim

## Background on alternative pathways to olefin production

Olefins are building blocks widely applied in the petrochemical industry. Light olefins (C<sub>2</sub>-C<sub>4</sub>) provide chemicals to cover the range from plastic production to the textile industry. Conventionally the production is based on thermal cracking of Naphta (1). While the conventionality does its purpose to produce essential basic chemicals, the need for chemical production independent of oil cannot be overlooked. In Norway, the country where this thesis is written, oil and gas industry have a significant contribution to the national pollution emissions in air. The environmental agency in Norway (miljødirektoratet) publishes yearly statistics on national emissions from industry. In 2018 13 million tons of CO<sub>2</sub> were emitted from oil and gas (2). Although precautionary efforts have been applied to lower environmental harmful releases, covering the demand for essential chemicals independently of the oil industry is an ongoing target. To reach the 1.5 °C global warming goal presented in the special report by IPCC, CO<sub>2</sub> removal efforts have to be implemented by 2100 (3). Carbon capture and utilization (CCU) is a novel technology that is being developed to provide the opportunity to extract CO<sub>2</sub> either from air or direct exhaust sources and further utilize it to essential components. Prototype power plants for the direct capture from air has already been implemented by carbon engineering in British Columbia and are in operation since 2015. Each unit is estimated to capture one million tons of CO<sub>2</sub> yearly (4). Applying CCU to develop a the market independent of oil industry, provides an environmental effort in lowering the CO<sub>2</sub> footprint while gradually replacing the industrial source to produce fuels and basic chemicals such as light olefins. A detailed representation of a tentative cycle where CO<sub>2</sub> is captured, further processed to olefins in a reaction with hydrogen attained from water electrolysis, utilized and returned to its initial form is presented in Figure 1-1.

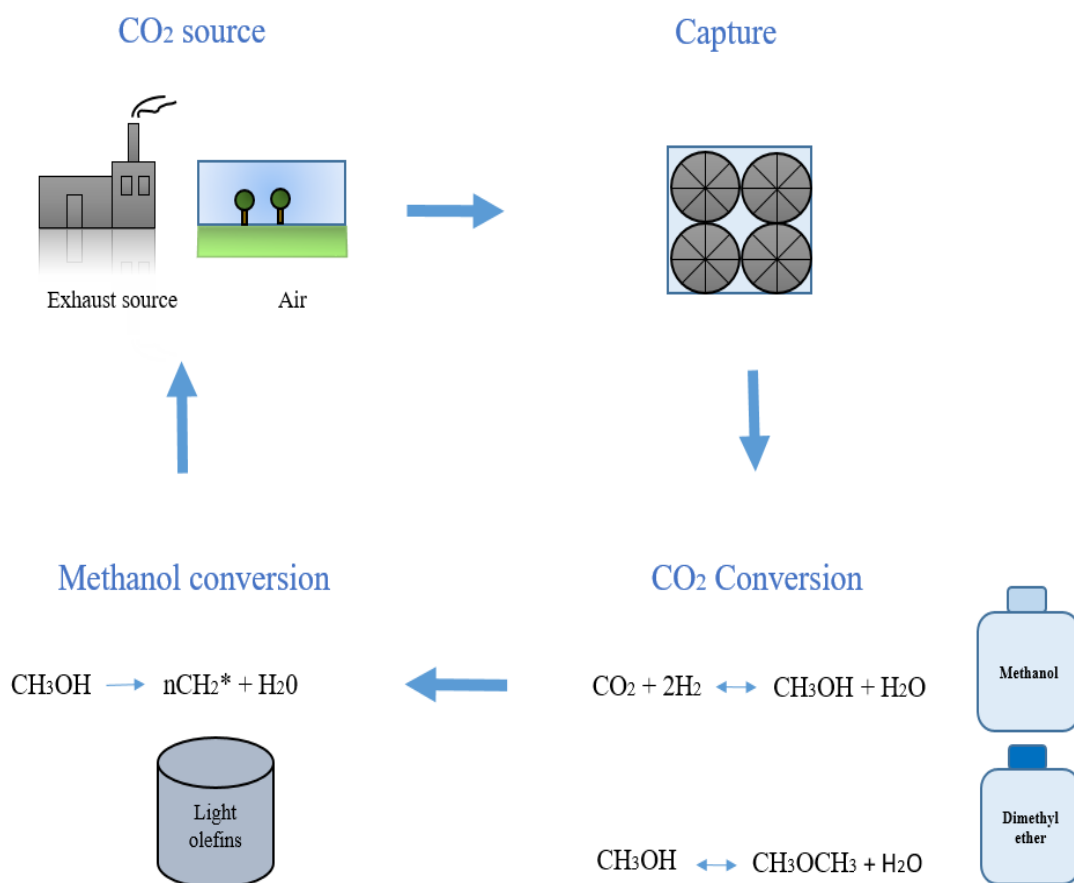


**Figure 1-1** The cycle of CO<sub>2</sub> utilization is presented. CO<sub>2</sub> is captured direct from air or exhaust gases. Further collected and converted to methanol. The methanol can further be dehydrated to form dimethyl ether or be applied for conversion to form light olefins. Application of light olefins results in new emissions, which brings CO<sub>2</sub> back to the cycle. Produced by the author.

CO<sub>2</sub> hydrogenation has been attempted with K-promoted bulk Fe-catalyst resulting in selectivity towards low olefins at 40 % and the undesired methane formation at 19 % (5). However, there are few extensive studies covering the step-wise reaction from CO<sub>2</sub> to olefins over zeotypes. The reaction has been studied over the bifunctional catalyst In: Zr over SAPO-34 achieving a hydrocarbon selectivity towards 65- 80 % with a 2.5% selectivity towards methane (6). Studies of SAPO-11 as a bifunctional catalyst for the conversion are however briefly studied. The lack of extensive studies on CO<sub>2</sub> conversion over zeotypes, motivates further research on i) CO<sub>2</sub> to olefins, ii) the separated study of the partial reaction methanol to olefins over SAPO-11.

## **Motivation and aim for this study**

In the catalysis research group at the Department of Chemistry, University of Oslo, research on new materials are often investigated by combining both fundamental and applied studies. Controlled and systematic studies on zeotype synthesis are performed to approach fundamental knowledge of catalysts properties in advance of their application for catalytic testing.

This master thesis forms a subpart of the larger CASCADE-X project in the group. Tentatively the objective of this project covered the synthesis of conventional and bifunctional SAPO-11 catalyst under different synthesis conditions. The AEL zeotypes would further be tested in the two-step conversion from CO<sub>2</sub> to hydrocarbons. The first step of the reaction is the direct conversion of CO<sub>2</sub> to methanol operated at 250°C at 50 bar. Performance tests were planned to be done by the supervision of Dr. Elisa Borfecchia. The second step is the conversion of methanol to light olefins/paraffins. Due to the unforeseen resignation of Co-supervisor Elisa Borfecchia, the objective got shifted to emphasize the second step of the reaction, namely the methanol to hydrocarbon reaction over a conventional SAPO-11 catalyst.

Previous work on the synthesis of SAPO-11 reveals the challenges of successfully synthesizing a regular catalyst with a surface area  $> 180\text{m}^2/\text{g}$ . The reader is referred to Table 3-1 for a systematic study on previous synthesis work. With several studies operating at crystallization temperatures 200°C and crystallization time between 24-48 h, the majority of studies result in irregular particle size and variable surface areas. It became quite interesting to systematically investigate the synthesis route for the conventional SAPO-11 catalyst.

The aim of this thesis consists of two essential parts. The first part is to obtain a fundamental understanding of the effect of different synthesis conditions and develop a synthesis method that provides a zeotype catalyst with good homogeneity, crystallinity and high surface area. To provide the required analysis, catalysts are characterized by various methods. The second part is to explore the potential of SAPO-11 as a catalyst for the methanol to olefins reaction. As SAPO-11 is briefly studied in literature and not previously synthesized or tested in the catalysis group, a commercialized SAPO-11 sample was

purchased as a comparison for catalyst behavior. The screening presented in this thesis is valuable in terms of covering the fundamental synthesis approach and catalyst behavior. In the larger scope, it forms a part of getting closer to investigating the application of SAPO-11 as a unidirectional microporous catalyst for the direct conversion of CO<sub>2</sub> to hydrocarbons.



## 2 Introduction

### 2.1 Microporous materials

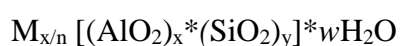
According to IUPAC, porous materials can be classified into three different categories determined by pore diameter. Materials with a pore diameter above 50 nm are called macroporous. Pore diameters between 2 and 50 nm are named mesoporous. The smallest pore diameters, below 2 nm, are categorized as microporous. The criteria for a material to be in the nano range is determined by the size of the material. The upper limit for a nanomaterial, is approximately 100 nm, while the lower limit is approximately 1 nm for one or more external dimensions. Therefore, all of the above categories of porous materials can be designated as nanoporous materials.

Conventional microporous materials such as zeolites have properties such as large surface areas and uniform sieve-like pore structures. These materials are commonly employed as adsorbents, carriers, catalysts and ion-exchange agents. The development of microporous materials has proven to be an important branch in industry for inorganic chemistry, including also catalytic applications (7).

### 2.2 What are zeolites and zeotypes?

Zeolites are microporous, crystalline aluminosilicates with three-dimensional framework structures. They have uniform pores of various sizes and dimensions depending on the framework. The building blocks are typically  $[\text{AlO}_4]^-$  and  $[\text{SiO}_4]$  tetrahedra linked together by the sharing of oxygen atoms. The inclusion of  $[\text{AlO}_4]^-$  leads to a negative charge on the framework. To preserve electronic neutrality of the zeolite, loosely held cations sit within the cavities. The fact that cations can be ion-exchanged makes zeolites a unique sorbent with selective properties.

A common representation of zeolites and other molecular sieves is expressed by a structural formula for the crystallographic unit cell as seen below:



For the formula above, M is the cation of valence n, w is the water content in numbers of molecules. The number of total tetrahedra in structure is denoted by (x + y) (8, 9).

Zeotypes are closely related to zeolites, with zeolites and zeotypes sharing the same framework structure, but zeotypes typically containing T-atoms other than aluminum and silicon, such as gallium, boron, germanium and phosphorous. In this thesis, the terms zeolite, zeotype and zeolitic materials will be used interchangeably. An important breakthrough in zeolitic materials was the synthesis of microporous aluminophosphates solids (ALPO), containing  $[\text{AlO}_4]^{5-}$  and  $[\text{PO}_4]^{3-}$  tetrahedra. Another group, SAPOs have gained great attention. These zeotypes contain silicon, or silicon and a metal, that partially replace phosphorus and aluminum in the ALPO framework. Zeotype materials display a greater diversity in chemical composition, and can frequently form frameworks currently unknown for zeolites. Therefore there has been great interest in these materials as potential heterogeneous catalysts as their performance can be different than zeolite catalysts (9, 10).

## **2.3 Historical development of zeolites**

The word “zeolite” is derived from two Greek words, “*zeo*” and “*lithos*” meaning to “boil” and “stone”. In 1756 the first zeolite mineral, stilbite, was discovered by the Swedish mineralogist Cronstedt. The zeolites were recognized as a new class of minerals consisting of hydrated aluminosilicates of the alkali and alkaline earths (11). Figure 2-1 shows a systematic timeline of the most significant discoveries in early zeolite science.

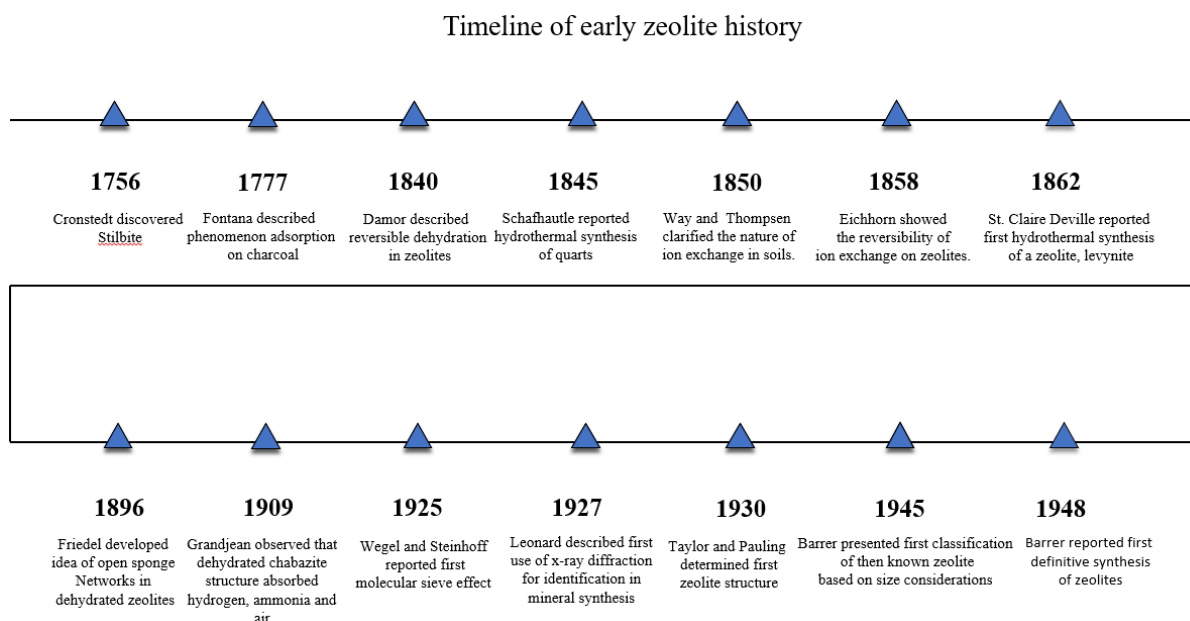


**Figure 2-1 Timeline showing important discoveries in zeolite science. The figure is constructed based on reference (11).**

## Natural zeolites

Naturally occurring zeolites are formed through a geothermal hydrothermal process. They are generally found as large crystals and vary in colors and morphology depending on the zeolite phase. Until the 1940s zeolites were considered to be minerals. Mineralogical studies shed light on understanding environments and crystallization conditions rather than practical uses. In 2017, 67 different species of natural hydrothermal zeolites were reported (12).

## Synthetic zeolites

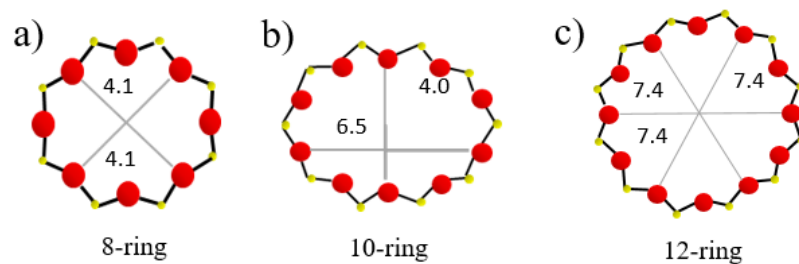
After the work by Barrier, zeolite synthesis was initiated by the Union Carbide Corporation in the search of approaches for the purification and separation of air. Between the end of the 1940s and the start of 1950s, a number of synthetic zeolites were discovered, including X, A and Y. This research contributed to shifting the emphasis towards more practical applications of zeolites. Synthetic zeolites were commercialized in 1954 as a new class of materials for separation and purification, the earliest application was as refrigerant gas. A complete definition of the term zeolite, applicable to not only mineral phases but also synthetic materials, was defined in its final by the subcommittee of the commission of New Minerals and Mineral Names of the International Mineralogical Association in 1997 (13).

## 2.4 Defining the framework

An increasing number of newly discovered zeolite materials has made it clear that similar materials can be produced by different laboratories under varying synthesis conditions. To classify the many different materials, Meier and Olson produced the first edition of the Atlas of Zeolite Structure types. This was a compilation of all the known framework types. Each type is designated a three-letter code which is described and defined based on published data. The most recent up-to-date database of framework types is only available online at <http://www.iza-structure.org/databases/> and to date contains 245 codes as of April 2019 (12, 14).

### Channels

Structures of zeolites are commonly described in terms of their pore size and dimensionality. Channels are classified by the number of T atoms that define the smallest pore openings, designated an n-ring, where n is the number of T-atoms in the ring. They are divided into different categories where 8-rings with a free diameter of ~4.0 Å are considered small pores, 10-rings (~5.5 Å) are considered medium and 12-rings (~7.0 Å) are large pores. Channels consisting of more than 12 T-atoms are rare and denoted extra-large. The free diameters are calculated using an oxygen radius of 1.35 Å. Distortion might occur because of the symmetry of the surrounding T-atom, which vary in size. Due to its inaccuracy, pore size is usually given by minimum and maximum dimensions (15, 16). A systematic representation of small, medium and large channels are found below in Figure 2-2.



Structure type	Example
8-ring	Heulandite, HEU
10-ring	SAPO-11, AEL
12-ring	Faujasite, FAU

**Figure 2-2** Examples of zeolite materials and framework types illustrating small pores (a), medium pores (b) and large pores (c). Figure is adapted from reference (10).

### Building units

The structures of zeolites are described by building blocks. Basic building units, BBU's are the common building blocks in all zeolites, namely the corner-sharing  $TO_4$  tetrahedra. These can always be applied to form the framework of a zeolite. A general ball-stick illustration of a two tetrahedra covalently linked by oxygen atoms is seen in Figure 2-3, where blue indicates T-atoms, and red represents oxygen atoms.

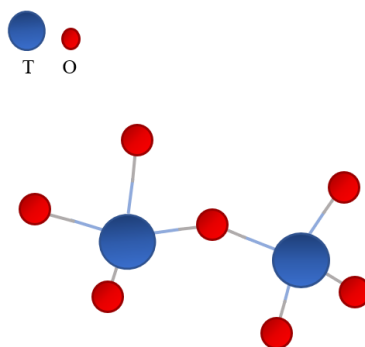


**Figure 2-3** Zeotype-building units. Two  $TO_4$  tetrahedra linked by corner-sharing. Adapted from (10).

To classify structural features where the BBUs fall short, higher-order schemes including SBUs, CBUs and NBUs are applied.

Secondary building units, SBUs, are non-chiral units containing up to 16 T-atoms. The rapid growth in zeolite science has led to the synthesis of many complex materials that require more than only one SBU to provide a full structural description of the framework. Due to this SBUs are no longer generated for newer frameworks in the Database of Zeolite structures.

Composite building units, CBUs, have replaced SBUs due to their flexibility and ability to highlight relationships between different frameworks. CBUs can overlap and do not necessarily describe the entire framework. CBUs represent common structural properties that are present in several zeolites. This includes, channels, chains, layers and cages. They are assigned codes corresponding to one of the framework types they are featured in and must be present in two or more framework types to be given a code.

Natural tiles or natural building units (NBUs) break down the zeolite framework to its natural tiling also described as primitive cages. They are applied when SBUs or CBUs are inadequate to describe the zeolite framework. The main characteristic of NBUs are that they can be applied to many frameworks regardless of the complexity. They fill the entire space and enumerate all small cavities in the framework (15). Below a selection of building units are visualized, Figure 2-4.

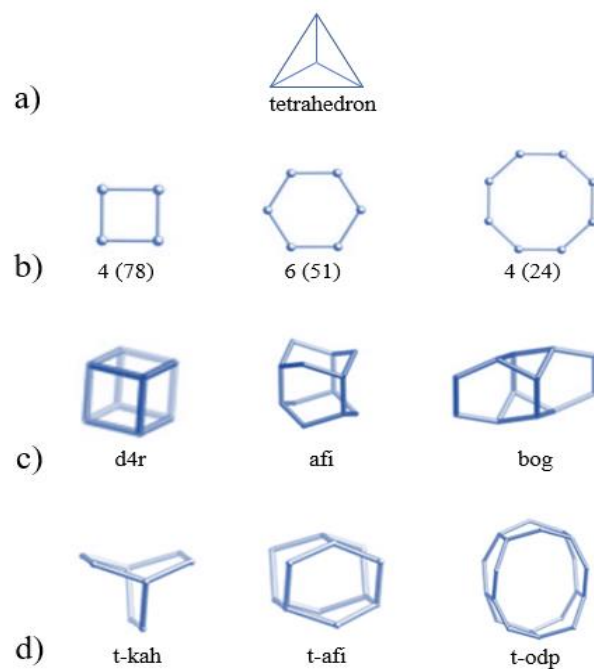


**Figure 2-4** An overview of building units, where a) indicates BBUs, b) indicates SBUs and frequency of occurrence given in parentheses, c) gives a common selection of SBUs and d) gives a selection of NBUs present in SAPO-11. The figure is constructed based on reference (16).

## 2.5 Properties

### 2.5.1 Acid sites

The catalytic activity of zeolites is commonly ascribed to active sites in the framework. The active sites can be linked to their redox properties when substituted with transition metals (17) or in terms of acidic sites (10). We will here, describe the latter. Acid sites are created to charge compensate for the substitution of  $[\text{AlO}_4]^-$  into the framework. There are two different types of acidity present in zeolitic materials, Brønsted acidity and Lewis acidity.

Brønsted acidity can occur due to direct reaction with acid during synthesis. Protons from the acid will react with the negatively charged oxygens in the framework, resulting in surface hydroxyl groups which are denoted Brønsted sites. It is also possible to generate this form of acidity through ion exchanging common ions with ammonium. The zeolite can then be heated to drive off ammonia, leaving a proton. A scheme explaining the structure of Brønsted sites in zeolites is shown in Figure 2-5a).

Lewis acidity is obtained when a zeolite material is heated to a temperature high enough to remove water molecules from the Brønsted sites. This usually occurs at temperatures above 600°C. When this happens the material will get electron-pair acceptor properties due to the lack of the hydroxyl group. Lewis acidity formation is represented in Figure 2-5b (10).

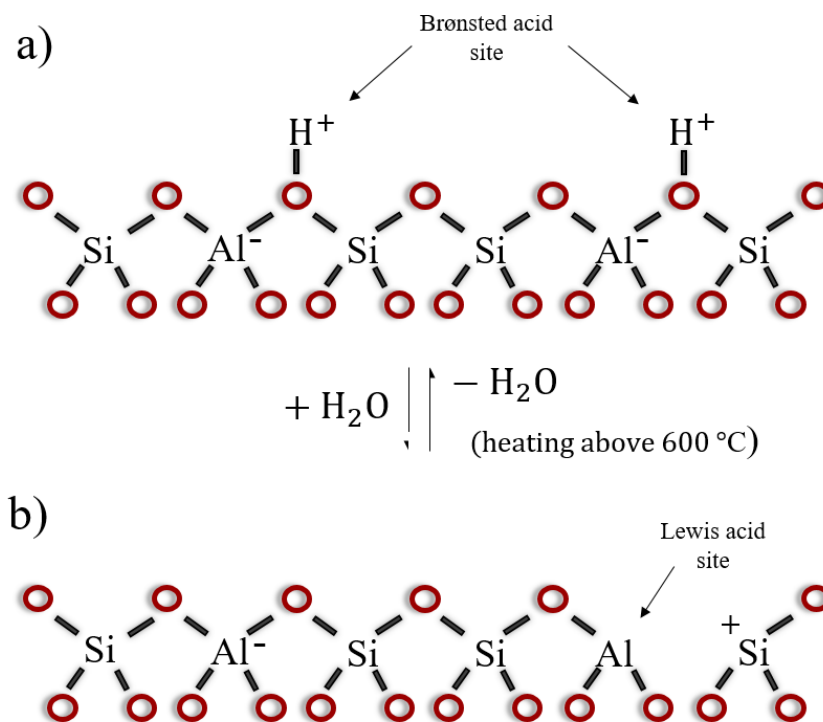


**Figure 2-5 Schematic illustration for the formation of a) Brønsted and b) Lewis sites in zeolites. Adopted from reference (10).**

In SAPOs the amount of Brønsted sites and their strength are dependent on both the Si content and its distribution in the framework. In principle, there are three substitution mechanisms describing how Si is incorporated into the structure. They are denoted SM1, SM2, and SM3. SM1 is the substitution of one Si for one Al. This leads to Si-O-P bonds and is not favorable. In SM2 one Si substitutes one P by isomorphous substitution, leaving negative charges in the framework. When the negative charge is compensated by a proton, Brønsted acidity occurs. In the SM2 mechanism, Si (4Al) sites are formed.

The last mechanism, SM3, proposes that adjacent Al and P are simultaneously substituted by two Si atoms. This leads to Si islands being formed. The mechanisms are presented in Figure 2-6. Commonly, SM2 accompanies SM3 due to the instability of Si-O-P structure. It



is speculated that the Brønsted acidity is higher at the edges of the Si islands created by SM3, rather than SM2 where Si is isolated (18).

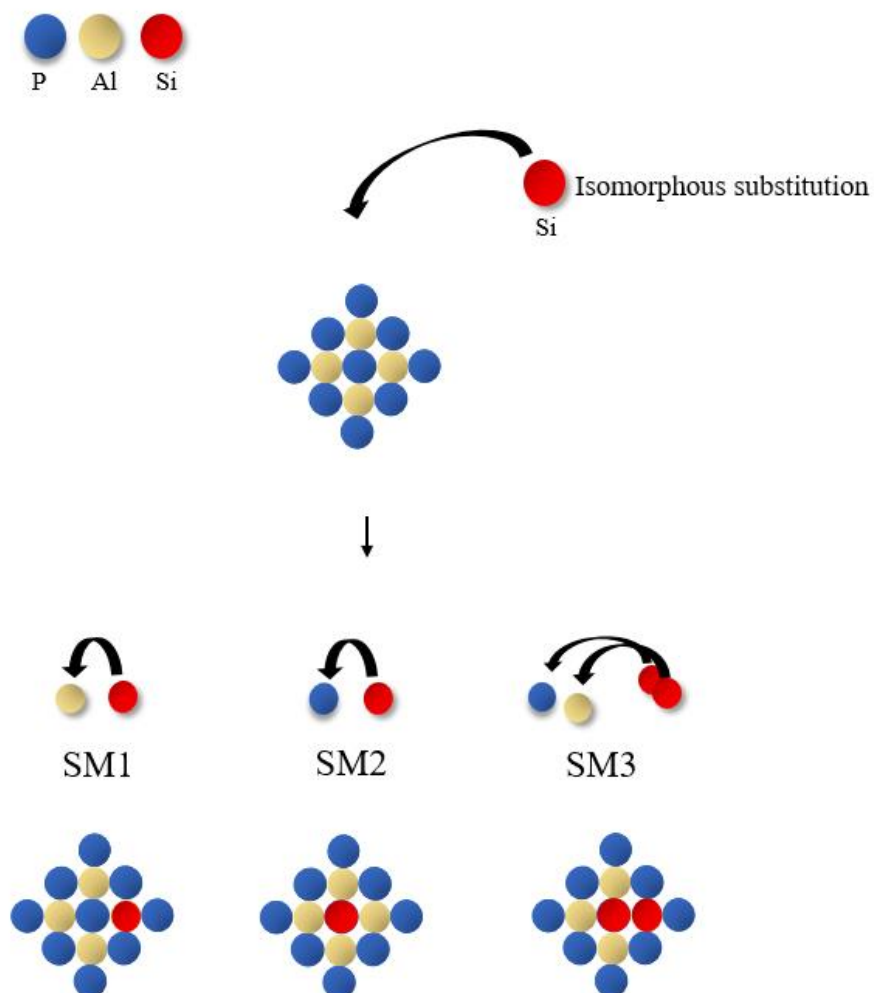


**Figure 2-6 Scheme for the generation of SM1, SM2 and SM3 mechanism present in SAPOs. Produced by author and inspired from (18).**

## 2.5.2 Shape selectivity

Shape selectivity was first introduced in the 1950s and describes how pore shape and size determine the chemical transformations that can occur inside a zeolite (19). Its application is valuable for reducing undesirable byproducts formed in a reaction while also increasing the amount of the desired products. A highly shape-selective catalyst can not only be seen as an environmental investment, but by reducing the number of undesired byproducts it also reduces economic costs related to the handling, separation, and disposal of waste.

In principle, there are 3 types of shape selectivity frequently described in the field of catalysis. (Figure 2-7). Their description is based on diffusion limitations and the steric requirements of the transition states of the reactions.

Reactant shape-selectivity occurs when molecules are restricted from entering the pores. The restriction is due to their size not fitting the pore openings. This means that only molecules with a dimension smaller than a critical size can reach the catalytic sites as indicated in Figure 2-7a).

Product shape selectivity indicates that while molecules are allowed to enter the pores and react at catalytic sites, not all molecules can leave the channels. Some of the molecules formed in the catalytic sites may be of such dimensions that they are unable to diffuse out. (Figure 2-7b).

Transition-state shape-selective catalysis arises when there are certain transition states occurring that require more space than what is available in the cavities. The overall reaction will favor less bulky intermediates (Figure 2-7c) (10).

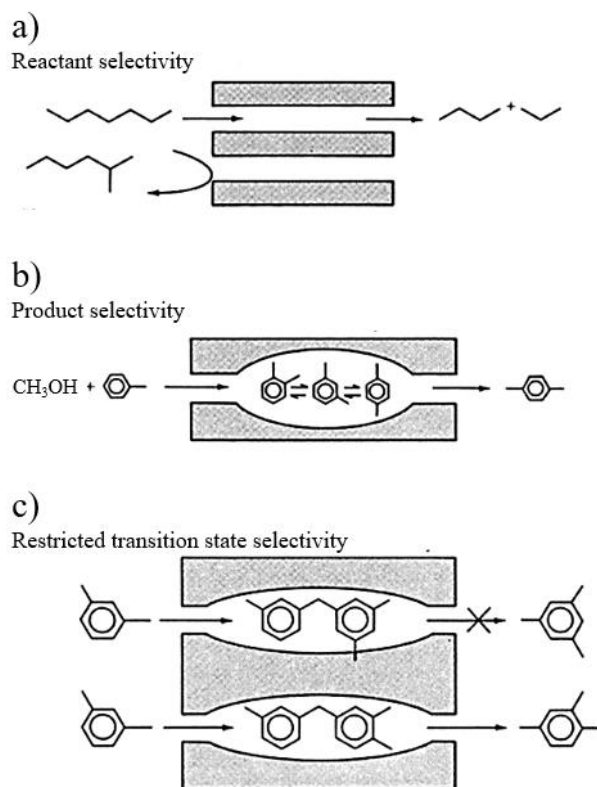


Figure 2-7 Shows the different types of shape-selective catalysis. a) reactant selectivity, b) product selectivity and c) transition state selectivity. Adopted from (10).

## 2.6 Catalysis and application of zeolitic materials

The term catalysis comes from ancient Greek and consists of two words, “*κατα*” and “*λύω*” translated to “down” and “loosening” or “dissolving.” A catalyst is a kinetic phenomenon and is commonly defined as something that makes a reaction go faster without being consumed in the process (20). A catalyst will affect the kinetics of a reaction, without changing the reaction thermodynamics. The kinetic effect is obtained by offering an alternative reaction mechanism to the desired product. Simplistically, this is done by lowering the activation energy for the current reaction. In principle, a catalyst works by accelerating a chemical reaction. It occurs by an adsorption process on the catalyst, where the reactants react to form a product. The products then leave the catalyst, which is denoted desorption. In this

matter, the catalyst is left unchanged and will be available for participating in another reaction. Due to this, catalysts are commonly described as reacting in a cyclic manner (Figure 2-8) (21, 22).

Catalysis is often subdivided into three disciplines: homogeneous, bio and heterogeneous catalysis. Homogeneous catalysis occurs when both reactants and the catalysts are in the same phase, for example in a gas phase or as more commonly seen in a liquid phase. This form of catalysis is also typically found in organometallic chemistry. Biocatalysis describes nature's catalytic processes. Enzymes are specific catalysts with properties that are present in many living organisms. Reactions with enzymes are life essential, and scientists today work on mimicking their behavior in synthetic materials. In heterogeneous catalysis, the catalyst and reactant are in different phases. The catalyst is often a solid, while the reactants are either liquid or gas, facilitating easy separation of chemicals from the catalyst. One common application of heterogeneous catalysis is in hydrogenation processes, in case of  $\text{CO}_2$  hydrogenation to chemicals. Figure 2-8 illustrates an energy diagram for a heterogeneous catalytic reaction with gaseous reactants and products while the catalyst is a solid. This demonstrates how the activation energy is considerably lowered for the catalytic process compared to the uncatalyzed reaction (22).

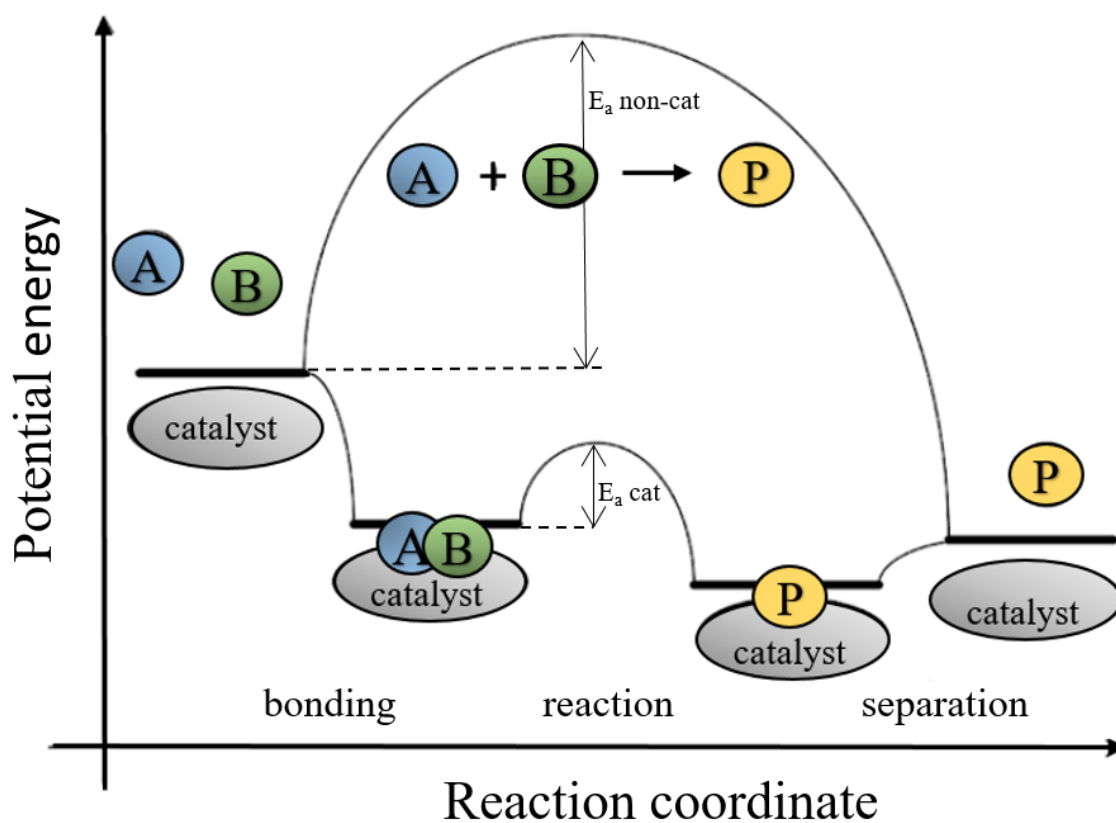


**Figure 2-8** Potential energy diagram for non-catalyzed reaction and catalyzed reaction with gaseous reactant and products and a solid catalyst. The term  $E_a$  is the activation energy. Adopted from (22).

Zeolitic materials are applied in large quantities in the industry. They are mostly used as detergent products and in refining processes. Both natural and synthetic zeolites are applied. However, for catalysis synthetic zeolites are preferred due to their improved quality and tunable properties. Figure 2-9 illustrates the common catalytic application of synthetic zeolites in industry, including the Methanol-to-olefins, which is the scope of this thesis.

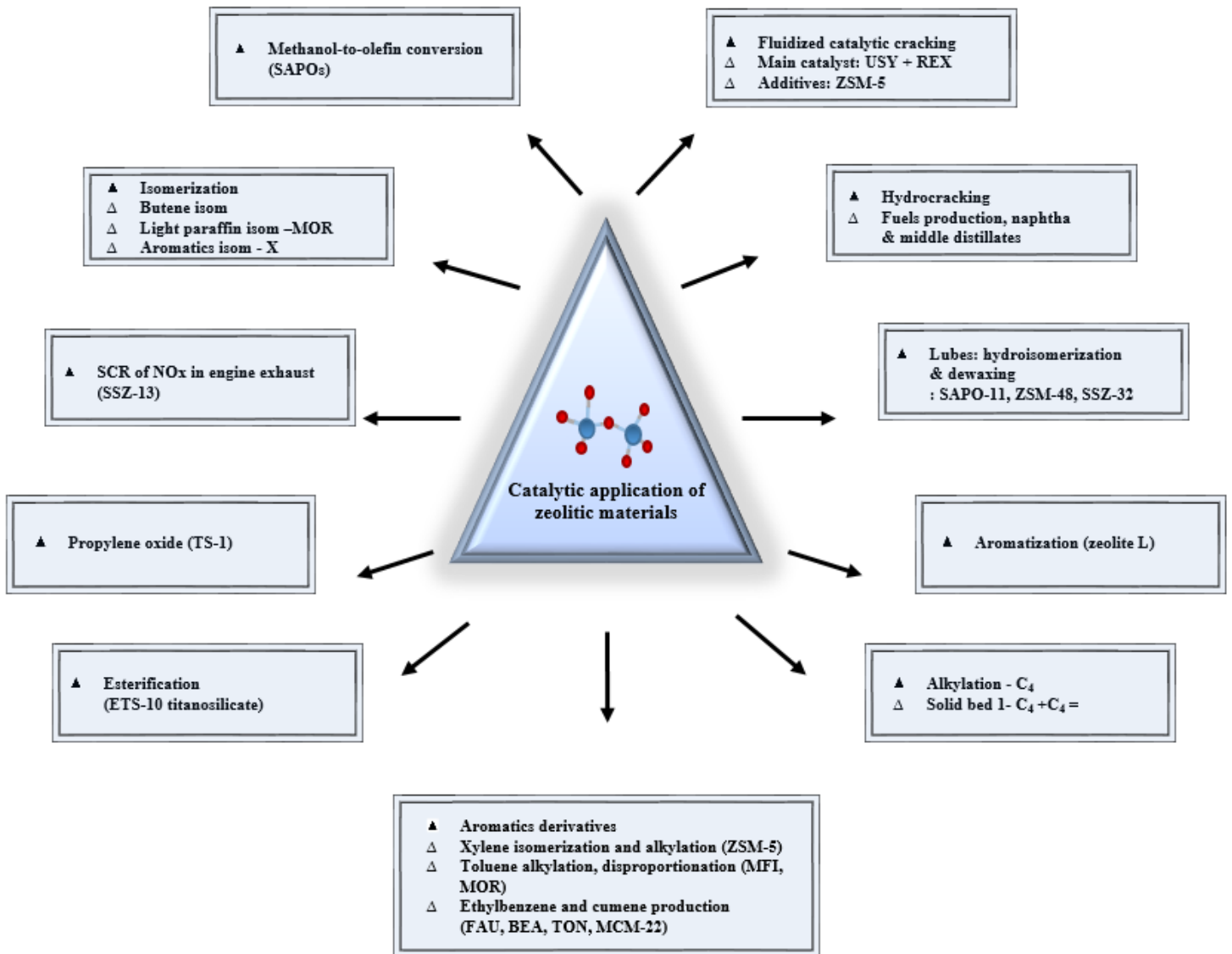
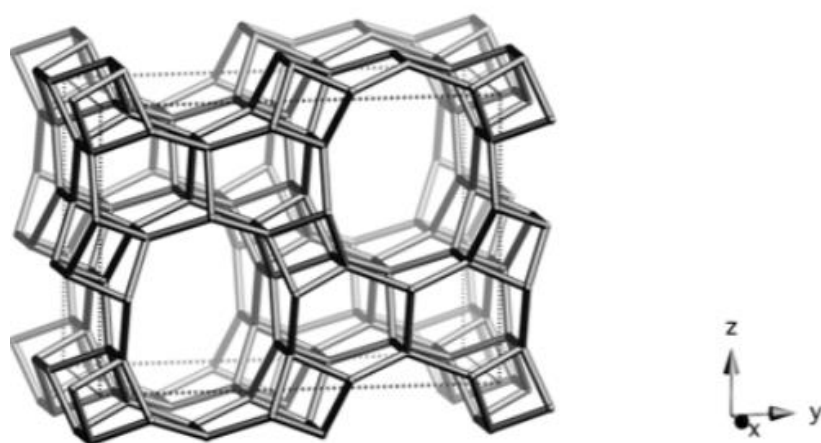


Figure 2-10 Produced by author. Literature is found in reference (23).

## 2.6.1 SAPO-11 as a heterogeneous catalyst for the conversion of methanol to olefins

SAPO-11 is a microporous zeolite of the AEL structure consisting of 10, 6 and 4 rings with one-dimensional, medium pore structure as seen in Figure 2-11 (16). Its mild acidic properties and molecular sieve actions can be exploited to enhance catalytic control (10).



**Figure 2-11** Illustrates the AEL framework with 10, 6 and 4 rings. The framework is viewed along [001]  
Figure taken from reference (16)

As a heterogeneous catalyst SAPO-11 has already been applied in various research such as n-alkane isomerization (24), lubricant dewaxing (25) and briefly methanol to olefins. (1) While the SAPO-34 analog of the Chabazite zeolite is largely covered in literature, the investigation of the unidirectional SAPO-11 for methanol to olefins is limited. Zhu et al. studied the conversion of methanol to olefins over synthesized SAPO-11 with a Si/Al = 0.3. They reported selectivity towards ethene and propene at 400 °C. The highest selectivity was 45 % obtained at 10 min TOS, before a rapid decrease to 25 % at 70 min (1). Wang et al. reported in 2015, the catalytic behavior of supplied SAPO-11 for methanol conversion at various reaction temperatures (350-550 °C) (26). Investigations show Selectivity towards hydrocarbons is favorable at higher temperatures, most stable at 400 °C with the highest selectivity towards C<sub>5+</sub> hydrocarbons.

The previous studies show the need for further and more extensive studies on methanol conversion for SAPO-11 providing fundamental information regarding its activity and selectivity towards lower olefins.

# 3 Theory and Methodology

## 3.1 Kinetics and thermodynamics of crystal growth

To synthesize a zeolite, two steps are necessary to consider. First a nucleus must be formed, and secondly the nucleus must grow into a crystal. For zeolite synthesis we consider solution–solid phase and the processes are divided into;

- 1) Nucleation
- 2) Growth

### 3.1.1 Nucleation theory

Nucleation is the initial step in crystal formation, where a number of atoms self organize to form a new phase. The process is homogeneous if nucleation occurs in the absence of foreign particles. If foreign particles are present in solution acting as points of nucleation, it is denoted heterogeneous nucleation. Both types are known as primary nucleation. If the process, however, is induced by the presence of crystals of the same substance, it is denoted secondary nucleation.

In a nucleation process, the atoms and molecules (growth units) are assumed to form small, spherical clusters, and the driving force for this is supersaturation. Supersaturation is commonly described as the difference in chemical potential ( $\Delta\mu$ ) between a molecule in solution ( $\mu_s$ ) and a molecule in the bulk in the crystal phase ( $\mu_c$ ). When  $\Delta\mu > 0$ , the solution is supersaturated allowing nucleation to take place, whereas when  $\Delta\mu < 0$ , solution is undersaturated and dissolution will occur (27, 28). Equation. (3-1) gives;

$$\Delta\mu = \mu_s + \mu_c \quad (3-1)$$

The total amount of work needed to form a nucleus can be described by two terms. The first term is a volumetric term. It relates to the difference in free energy of the system in the initial and final state. The second term is a surface energy term which is a result of the interface between nucleus and solution. Equation (3-2) gives

$$\Delta G_T = -\frac{4}{3}\pi * \frac{r^3}{V} \Delta\mu + 4\pi * r^2 \sigma \quad (3-2)$$



Here  $\Delta G_T$  is the total free energy,  $V$  is the atomic volume,  $r$  is the radius of the spherical cluster,  $\Delta\mu$  is the difference in chemical potential and  $\sigma$  is the surface free energy.

By plotting the total free energy ( $\Delta G_T$ ) as a function of the radius, (Figure 3-1), it can be visualized how the function will reach a maximum. The maximum value of  $\Delta G_T$  corresponds to a value of  $r^*$  which is denoted the critical radius. Hence,  $r^*$  must be reached for nucleation to occur.

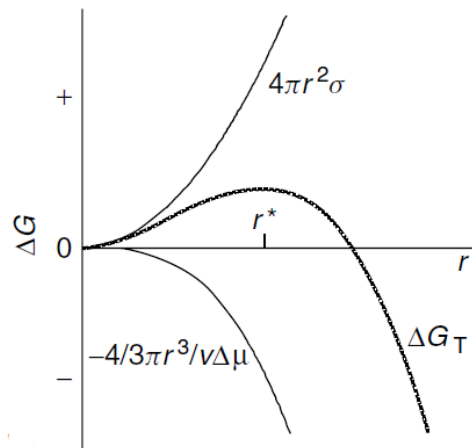


**Figure 3-1** Total free energy as a function of cluster size. Taken from (28).

The rate of nucleation must be considered to understand the nucleation process. It describes the number of nuclei formed per unit time per unit volume. This is commonly expressed by an Arrhenius-type of equation.

$$J = A \exp \left( \frac{-\Delta G^*}{kT} \right) \quad (3-3)$$

Here  $J$  is the rate of nucleation,  $\Delta G^*$  is the Gibbs free energy,  $A$  is a pre-exponential factor depending on the supersaturation,  $k$  is Boltzmann constant and  $T$  is the absolute temperature (28).

### **3.1.2 Crystal growth theory – Conventional and recent published theory**

Crystal growth is a process where an atom or a molecule gets incorporated into the crystal surface. The different processes involved will include; i) Atoms that are transported through the solution; ii) The atoms attach at the surface; iii) Movement of atoms on the surface and; iv) Atoms attach to edges and kinks in the crystal. The transport process is related to the first step, while step ii - iv are surface-related processes. The overall crystal growth is controlled by the slowest occurring steps, which could be either.

The Kossel model is conventionally applied to consider crystal growth. The model assumes the surface of a crystal is made of cubic units which will form layers of monoatomic heights. Such a crystal surface contains multiple kinks and terraces where growth units attach leading to different bonding (28). Recent studies from the University of Manchester present two different methodologies on gaining more knowledge on zeolitic crystallization. i) A methodology that applies the dissolution of zeolitic materials for atomic force microscopy (AFM) measurements to study crystal growth (29), and ii) A computational method that predicts the crystal growth of material with Monte Carlo simulations (30). Since zeolitic materials crystallize at high temperatures and not from a clear solution, it is not possible to study growth in situ with AFM. Instead, the study purposes to investigate the reversed reaction where the materials are studied under dissolution. The second methodology gives rise to a new model that uses the natural tiling in zeolitic materials to reconstructs its crystal structure through Monte Carlo algorithms. Both methodologies have been applied for the chabazite structure in SAPO-34 and show mechanisms related to spiral growth. This has the potential to become a valuable tool in understanding crystal growth for zeolitic materials and illustrates that the more idealized models might not be strictly applicable to zeolite growth.

### **3.1.3 Nucleation and growth in zeolitic materials**

The process of nucleation and growth in zeolites and zeotypes is complex. Crystal size and morphology are dependent on multiple parameters and vary for different structures. However, the process of forming a zeolitic crystal has some common steps (Figure 3-2). The first step is the mixing of amorphous reactants. Here a heterogeneous amorphous primary phase is formed. Heating results in the formation of a second amorphous phase. After an induction period, the process of nucleation takes place. Finally, growth occurs at the expense

of the amorphous phase. These steps have been studied during the last years, but its complexity makes it yet difficult to generalize (28).

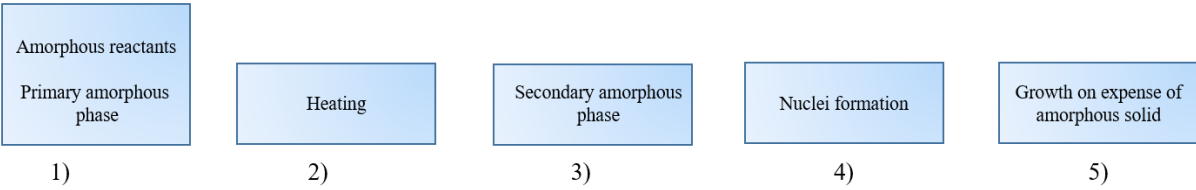


**Figure 3-2 Steps for nucleation and growth in zeolitic materials. Adapted from literature found in (28).**

A typical crystallization curve for a zeolitic material as a function of time is presented in Figure 3-3. It describes how the nucleation rate rapidly increases before decreasing to zero. In addition, the crystal sizes and supersaturation are plotted as a function of time.

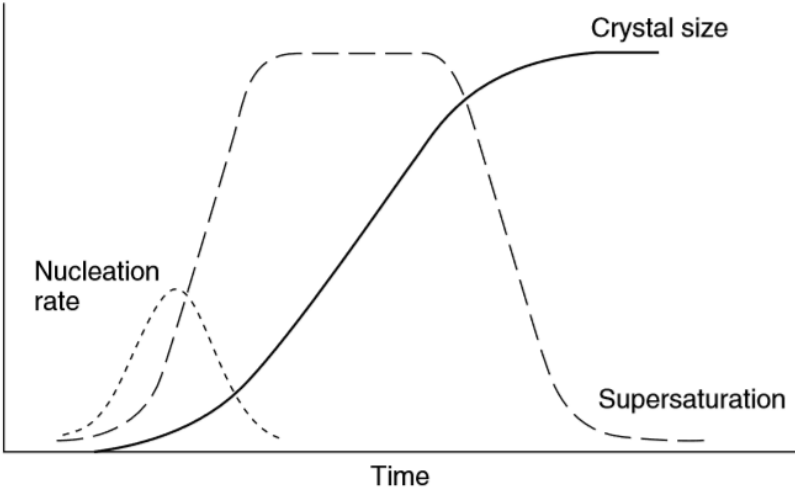


**Figure 3-3 Evolution of nucleation, growth, and supersaturation as a function of time (28).**

## 3.2 Zeolite synthesis

### 3.2.1 Hydrothermal method and HSE aspects.

The hydrothermal method refers to the placing of reactants in water (hence hydro) and heating to a temperature above its boiling point. A homogeneous solution of a reaction mixture is transferred to a non-reactive liner, commonly Teflon. The liner is placed inside a closed vessel, denoted an autoclave (Figure 3-4). The autoclave is commonly constructed from thick layers of stainless steel which are required to withstand the pressure that arises upon heating (31).

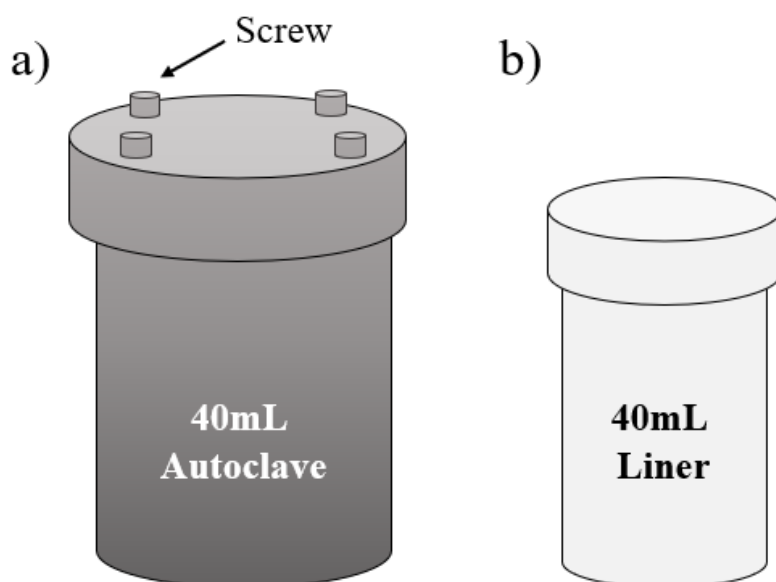


**Figure 3-4 Shows a typical used autoclave a) and a Teflon liner b) Produced by author.**

Since the reaction is carried out in a closed vessel, the pressure, volume and temperature dependencies of water are important.

Figure 3-4 shows a V-T diagram where volume/density is plotted as a function of temperature. This type of diagram identifies when the coexistence of the two phases occurs. Liquid and vapor are visualized in the closed two-phase region indicated by the saturated liquid and saturated vapor line. The dotted lines in the figure are lines of constant pressure, namely isobars. As the temperature increases the volume increases while the density decreases. If the temperature reaches 374.15 °C corresponding to a pressure of 221.2 bar the critical point is reached. At this point, the phases no longer coexist and a single-phase denoted a supercritical fluid is formed (31, 32).

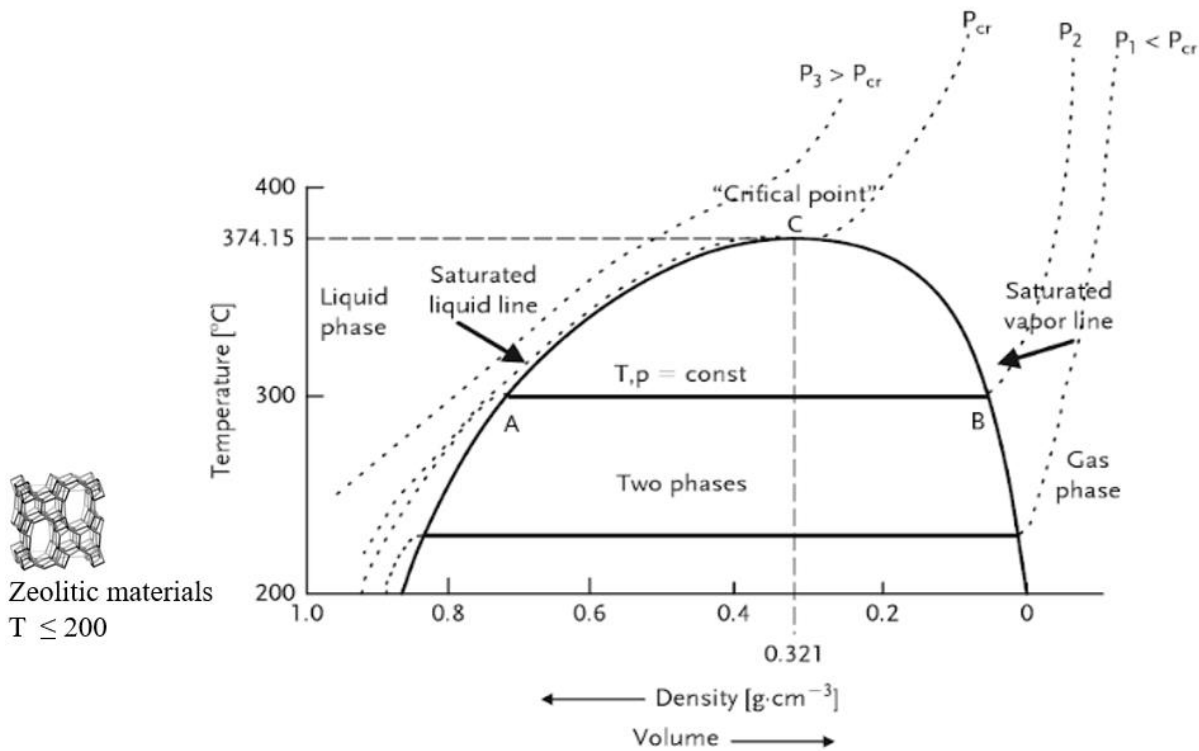
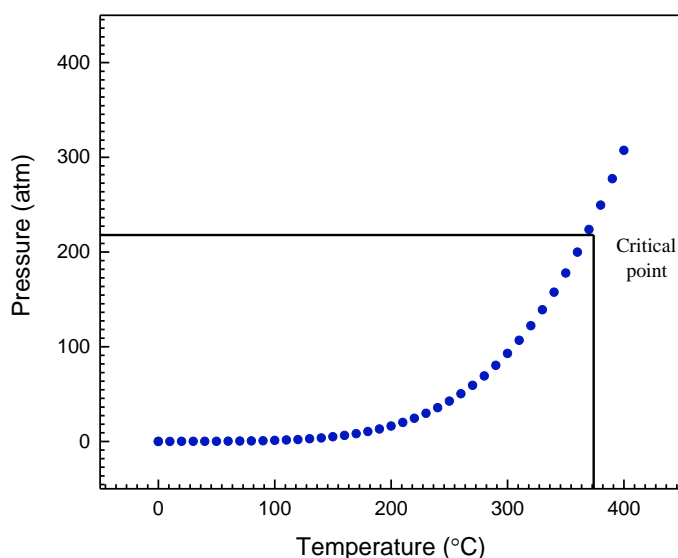


Figure 3-5 Volume/density temperature dependence of water. Adapted from (32)

To estimate the dependency of pressure related to temperature for the synthesis of zeolitic materials a P-T plot for the low-temperature region is convenient (Figure 3-6). At low temperature, the water vapor pressure is 0. However, as the temperature exceeds 200 °C, the pressure increases rapidly. The hydraulic effect is clearly illustrated at 218 atm with the temperature being 374.15 °C at the critical point. Therefore, zeolitic synthesis is operated at 200 °C or below (31, 32).



**Figure 3-6 Pressure /temperature dependence of water vapor calculated with Teten's equation. The critical point is highlighted at 218 atm and 374.15 °C. Produced by author.**

In terms of HSE considerations taken in this thesis, pressure, volume and temperature dependencies are crucial. The autoclaves are equipped with a safety mechanism in case of overpressure. This lies in the screw design. If the autoclave is exposed to higher pressures than it can withstand, the screws will break, loosening the lid avoiding an uncontrolled explosion.

### **3.2.2 Theoretical effect of important synthesis parameters**

The synthesis of zeolitic materials have many features and complexity connected to it. In an attempt to understand their interference and how to establish a proper synthesis route, it is important to mention the effect of important parameters independently. Below a selection of critical parameters will be described, with theoretical expectations considered. The different parameters will follow in *italic* and are based on the literature of Cejka et al (33) considering zeolite synthesis. Nevertheless, it is important to note that the materials synthesized in this thesis are SAPOs and not zeolites. The effect of synthesis parameters for SAPOs are not yet fully explored. Therefore, one does not expect identical behavior for zeolites and zeotypes. However, this comparison is useful when exploring observed behavior in the synthesized SAPO- 11 samples.

### ***Si/Al ratio***

The ratio between silicon and aluminum are important in means of determining structure and composition. Certain trends related to preparation methods in regards to ratios have been established. For instance, zeolites with low Si/Al ratio (Below 5) are often synthesized with strong alkalinities, such as A (LTA) and X (FAU). On the contrary, zeolites with high Si/Al ratios (above 5) are often synthesized from a gel with low alkalinity, such as zeolite beta (BEA) and ZSM-11 (MEL).

However, there is no significant correlation between Si/Al ratios in an initial reaction mixture compared to the final solid system, this might be determined by several parameters.

### ***Temperature***

An increase in temperature increases the rate of both nucleation and growth. In literature, it is stated that the crystal growth rate will increase more than the nucleation. This means that one expects the crystal size to increase with increasing temperature. The effect can also affect the morphology of the system.

### ***Alkalinity***

Studies on alkalinity for zeolitic materials have revealed that the solubility of Si and Al sources increases with a higher level of alkalinity. As a result, the induction time is reduced as well as the nucleation. Overall it will lead to an increase in the rate of crystallization.

### ***Stirring***

Zeolites are commonly, but not exclusively, synthesized under static conditions. Stirring increases the rate of crystallization as it increases the rate of mass transfer, and decreases the time to supersaturation. This leads to the formation of smaller crystals. Stirring has also been shown to affect the selectivity towards a specific phases.

### ***Ageing***

Ageing is the period from when the reactants are homogeneously mixed until the mixture is heated to the crystallization temperature. Several studies indicate that ageing has an important effect on the gel chemistry. The complexity is yet not fully understood. However, it is speculated that ageing might lead to an increase in the nucleation rate and a reduction in induction time and crystallization time. In addition, it is empirically determined that ageing results in a reduction in crystal size.

### *Crystallization time*

For zeolitic materials, the crystallinity commonly increases as a function of time. Therefore the crystallization time is highly relevant. The metastable properties of such compounds are however relevant to consider when choosing the crystallization time. First, a metastable phase occurs. As time increases the most stable, denser, phases will replace the temporary ones.

### *Structure directing agent*

The addition of a template to a synthesis mixture is believed to enhance the structure for the dominating phase. In the work of Davis and Lobo, it was defined that the roles of inorganic and organic hosts are to behave as space-filling species, structure-directing agents and templates. By the term structure-directing it is meant that it is possible to synthesize a specific structure with a single organic species. The term template refers to the adoption of geometric and electronic configurations that are specific to the templating molecule. As the molecule is removed from the host, the shape of the guest molecule is retained.

### **3.2.3 Published work on synthesis of SAPO-11**

In the work of this thesis, a secondary study on synthesis methods for SAPO-11 was conducted. The purpose of the study was to investigate and gain knowledge regarding the establishment of a promising synthesis route for SAPO-11. 20 published articles were systematically chosen and ordered with regards to the published date. The synthesis method of interest was the conventional hydrothermal treatment. For comparative reasons 3 different, novel synthesis methods from 2018 were also chosen and examined.

This study shows development in synthesis methods from 1982 to 2018. It is primarily used as an aid in the development of the synthesis route presented in this thesis. Chosen parameters to investigate are synthesis method, gel composition, crystallization temperature and time. The results chosen for comparative reasons are; particle size, distribution, and porosity measured in terms of specific surface area. The study is presented in Table 3-1.



**Table 3-1 Previous work on the synthesis of SAPO-11 with DPA present as a template. In this table reference and published year are given for each study. The conditions for the synthesis are given in means of synthesis method, medium, reactants, gel composition, crystallization temperature ( $t_{\text{crystal}}$ ) and time. The individual methods are characterized and investigated by particle size, shape, distribution and specific surface area. Highlighted in bold are studies who attained SAPOs with promising regularity and surface area Glossary of explanation is represented at the bottom of the table.**

Reference	Published Year	Synthesis method	Medium	Reactants	Gel composition <i>Al<sub>2</sub>O<sub>3</sub>:P<sub>2</sub>O<sub>5</sub>:SiO<sub>2</sub>:SDA:H<sub>2</sub>O</i>	$t_{\text{crystal}}$ (°C)	Time (h)	Particle size ( $\mu\text{m}$ )	Particle shape	Specific surface area ( $\text{m}^2\text{g}^{-1}$ )
Zhang <i>et al.</i> (34)	2018	Two step CHT	Water	H <sub>3</sub> PO <sub>4</sub> , AlO(OH), TEOS, DPA	1.0 : 0.74: 0.3: 0.93: 41	150 185	6 24	<b>≈ 10</b>	<b>Pseudo spherical, regular</b>	<b>207</b>
Lyu <i>et al.</i> (18)	2018	DGC HT	Water	H <sub>3</sub> PO <sub>4</sub> , AlO(OH), 30%SiO <sub>2</sub> , DPA	1.0 : 1.1: 0.4: 1.1: 50	200	24	-	irregular	-
Du <i>et al.</i> (35)	2018	SF HT	None	AlO(OH), fumed SiO <sub>2</sub> , DPA* H <sub>3</sub> PO <sub>4</sub> CTAB	-	200	24	2-3	Circular aggregates, partly regular	132 209
Liu <i>et al.</i> (36)	2018	GSM HT	Water	H <sub>3</sub> PO <sub>4</sub> , AlO(OH), 30%SiO <sub>2</sub> , DPA	1.0: 1.1: 0.4: 0.8: 30	200	4-24	< 5	Irregular	211
	2018	CHT	Water	H <sub>3</sub> PO <sub>4</sub> , AlO(OH), 30%SiO <sub>2</sub> , DPA	1.0 : 1.1: 0.4: 0.8: 30	200	4-24	>10	irregular	198
Wu <i>et al.</i> (37)	2015	CHT	Water	H <sub>3</sub> PO <sub>4</sub> , AlO(OH), TEOS, DPA	1.0 : 1.0: 0.3: 1.2: 120	185	48	≈ 2	Circular aggregates, partly regular	160
Liu <i>et al.</i> (38)	2013	CHT	Water	H <sub>3</sub> PO <sub>4</sub> , AlO(OH), 26.9%SiO <sub>2</sub> , DPA	1.0 : 1.0: 0.2: 1.0: 40	180	48	≈ 2	<b>Pseudo spherical regular</b>	<b>239</b>
Bing <i>et al.</i> (39)	2013	CHT	Water	H <sub>3</sub> PO <sub>4</sub> , AlO(OH), 27.5%SiO <sub>2</sub> , DPA	0.86: 1.0: 0.4: 1.1: 55	200	17.83	-	irregular	-
Song <i>et al.</i> (40)	2012	CHT	Water	H <sub>3</sub> PO <sub>4</sub> , AlO(OH), 40%SiO <sub>2</sub> , DPA	1.0 : 1.0: 0.6: 1.2: 50	200	48	≈ 10	Circular aggregates -	-
Zhang <i>et al.</i> (41)	2009	CHT	Water	H <sub>3</sub> PO <sub>4</sub> , AlO(OH), 25%SiO <sub>2</sub> , DPA,DIPA	1.0 : 1.0: 0.4: 1.0: x	190	24	<b>7-10</b>	<b>Circular aggregates, regular</b>	<b>212</b>
Lopez <i>et al.</i> (42)	2008	CHT	Water	H <sub>3</sub> PO <sub>4</sub> , Al(O-i-Pr) <sub>3</sub> , 99% precipitated SiO <sub>2</sub> , DPA	0.9 : 1.0: 0.1: 0.3: 40	150	6	-	Spherical aggregates, irregular	124
Liu <i>et al.</i> (43)	2008	Two step CHT	Water	H <sub>3</sub> PO <sub>4</sub> , AlO(OH), 28%SiO <sub>2</sub> , DPA,DIPA	1.0 : 1.0: 0.5: 0.5: 49	120 190	4 20	-	Irregular	95.9
Zhang <i>et al.</i> (44)	2007	CHT	Water	H <sub>3</sub> PO <sub>4</sub> , AlO(OH),	1.0 : 1.0: 0.4: 1.0: 28	190	24	7-10	Spherical aggregates,	212

				25%SiO <sub>2</sub> , DPA,DIPA				-		
Zhang <i>et al.</i> (45)	2007	Two-step CHT	Water	H <sub>3</sub> PO <sub>4</sub> , AlO(OH), 25%SiO <sub>2</sub> , DPA,DIPA	1.0 : 1.0: 0.4: 1.0: x	150 190	2.25 24	-	Cubic single crystals, regular	211
Blasco <i>et al.</i> (25)	2006	CHT	Water	H <sub>3</sub> PO <sub>4</sub> , Al(O-i-Pr) <sub>3</sub> , 40% SiO <sub>2</sub> , DPA	1.0 : 1.0: x: 0.9: 57	195	48	<b>2</b>	<b>Rods, regular</b>	<b>178</b>
Wang <i>et al.</i> (46)	2006	CHT	Water	H <sub>3</sub> PO <sub>4</sub> , Al(O-i-Pr) <sub>3</sub> , TEOS, DPA	1.0 : 1.0: 0.2:1.0:55	200	48	2-4	Cubic microcrystals, -	173
Hu <i>et al.</i> (47)	2005	CHT	Water	H <sub>3</sub> PO <sub>4</sub> , Al(O-i-Pr) <sub>3</sub> , fumed SiO <sub>2</sub> , DPA	1.0 : 1.0: x: 0.9: 36	175	96	-	-	-
Walendziewski <i>et al.</i> (48)	2003	CHT	Water	H <sub>3</sub> PO <sub>4</sub> , Al <sub>2</sub> O <sub>3</sub> , 98% SiO <sub>2</sub> , DPA	1.0 : 1.1: 0.4: 1.5: 47	200	96	-	-	214
Sinha <i>et al.</i> (49)	1999	CHT	Water	H <sub>3</sub> PO <sub>4</sub> , Al(O-i-Pr) <sub>3</sub> , fumed SiO <sub>2</sub> , DPA	1.0:1.0: 0.2: 1.0: x	160	24	≈5	<b>Spherical, regular</b>	<b>140</b>
Singh <i>et al.</i> (50)	1996	CHT	Water	H <sub>3</sub> SO <sub>4</sub> , Al(O-i-Pr) <sub>3</sub> 28%SiO <sub>2</sub> , DPA	1.0:1.0: 0.5: 1.0: 40	200	24	-	Spherical aggregates	
Lok <i>et al.</i> (51)	1984	CHT	Water	H <sub>3</sub> PO <sub>4</sub> , Al(O-i-Pr) <sub>3</sub> 95%SiO <sub>2</sub> , DPA	1.0:1.0: 0.1: 1.0: 42	150	133	-	-	-
	1984	CHT	Water	H <sub>3</sub> PO <sub>4</sub> , Al(O-i-Pr) <sub>3</sub> 30%SiO <sub>2</sub> , DPA	1.0:1.0: 0.6: 0.9: 57	200	48	-	-	-

**CHT – Conventional hydrothermal treatment**

**DGC – Dry gel conversion method**

**GSM – Grinding synthesis method**

**SF – Solvent-free**

**HT- Hydrothermal treatment**

**CTAB - Cetyl trimethylammonium bromide**

**DIPA – Diisopropylamine**

**DPA – Dipropylamine**

**TEOS – Tetraethyl orthosilicate**

This secondary study shows the influencing parameters from published work on the synthesis of SAPO-11. For all studies, the Al:P ratio is approximately constant at the value of 1. Template ratio in the composition mostly approaches 1 with few deviations. Ratios of Si vary between, 0.1 – 0.6. The water content in the composition is not a constant parameter and alters with the majority containing a H<sub>2</sub>O/Al ratio of between 40 to 50. The synthesis temperature varies from 150 to 200 °C, with a crystallization time being relatively short. The majority of the studies report aggregates of spherical particles, but the level of homogeneity varies with cubic and rod-like particles reported. Only 3 of the 20 studies presented, reported the synthesis of SAPO-11 materials that are both homogeneous and with a surface above 200m<sup>2</sup>/g. (Zhang et al and Liu et al.) From this work, few systematic trends can be obtained. However, it shows that the best crystallization conditions are obtained when the temperature is above 150 and below 200°C and when Si/Al is 0.5 or below.

### **3.3 Theory of characterization techniques**

#### **3.3.1 Powder X-ray diffraction**

Powder x-ray diffraction (PXRD) is an effective method for the determination of crystal structure of materials. In catalysis, this method is a standard method used for material identification

The method is based on the theory of interference. Two waves that travel in the same direction with the same wavelength can reinforce or cancel each other out. This is known as constructive and destructive interference. Constructive interference occurs when the waves traveling are in phase with a phase difference of  $n\lambda$ , where  $n$  is an integer and  $\lambda$  is the wavelength. If the path difference is of  $n\lambda/2$  destructive interference is observed.

When X-ray beams incident on an array of atoms, they will be diffracted by the crystallographic planes, as seen in Figure 3-7. Bragg's law Equation (3-4) states that waves only stay in phase when the following relationship is satisfied,

$$n\lambda = 2d\sin\theta \quad (3-4)$$

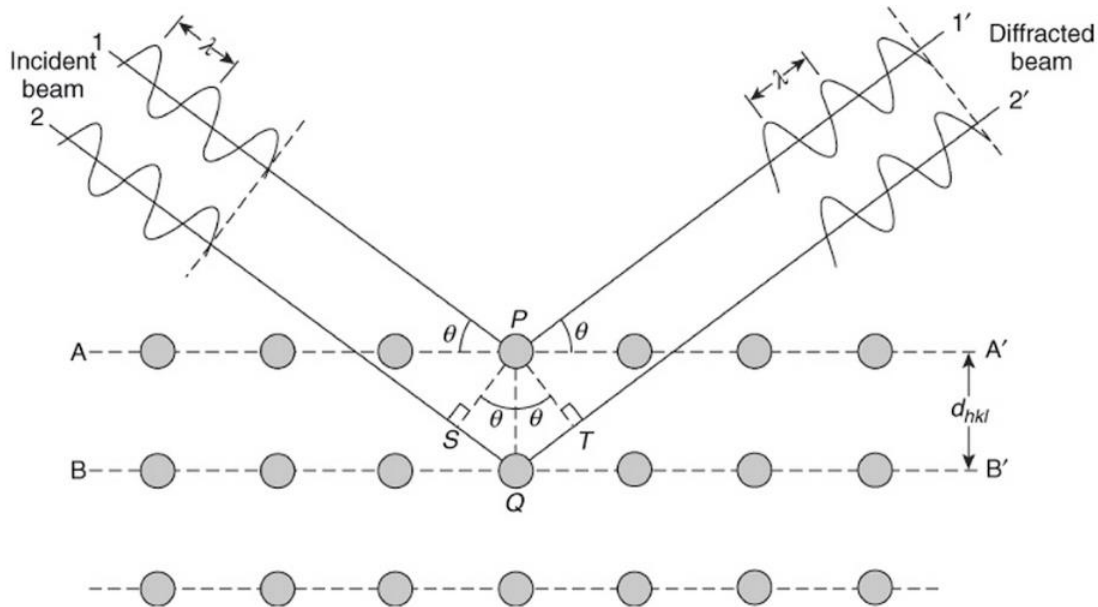


**Figure 3-7 Schematic illustration of the principle behind diffraction. Two beams, beam 1 and 2 are deflected by the crystal planes, A and B. To obtain constructive interference, their path difference  $SQ + QT = 2d\sin\theta$ , must equal  $n\lambda$ . (52) Here  $d$  is the lattice spacing between parallel crystal planes and  $\theta$  is the diffraction angle.**

The information obtained based on Bragg's law provides knowledge on the spacing between the crystal planes. This can be translated to determine crystal structure. A diffractogram shows intensities on Y-axis and diffraction angles ( $2\theta$ ) on X-axis. Peak positions in the diffractogram are related to Miller indices (hkl) and can either be calculated or found published by the International Centre for Diffraction Data (ICDD) (52).

### 3.3.2 Scanning electron microscopy

One of the most common techniques for observing specimen surfaces is the scanning electron microscopy (SEM). A topology image of the surface of the specimen can be constructed by scanning an electron probe along the sample surface. When an electron beam hits the surface, signal electrons are emitted. These can be collected by a detector, further amplified and used to reconstruct a surface image. This technique can provide knowledge regarding particle size, composition, and defects.

A simplified illustration of the instrumentation setup is presented in Figure 3-8. The illustration shows an electron gun which is a thermionic emission gun. It has a filament made

from tungsten wire or  $LaB_6$ . The electron beam is created when the filament is heated up to high temperatures. A condenser lens is used to converge the beam and an objective lens is used to focus the beam on to the specimen. Scanning coils are needed to provide a scanning system for image formation (53).

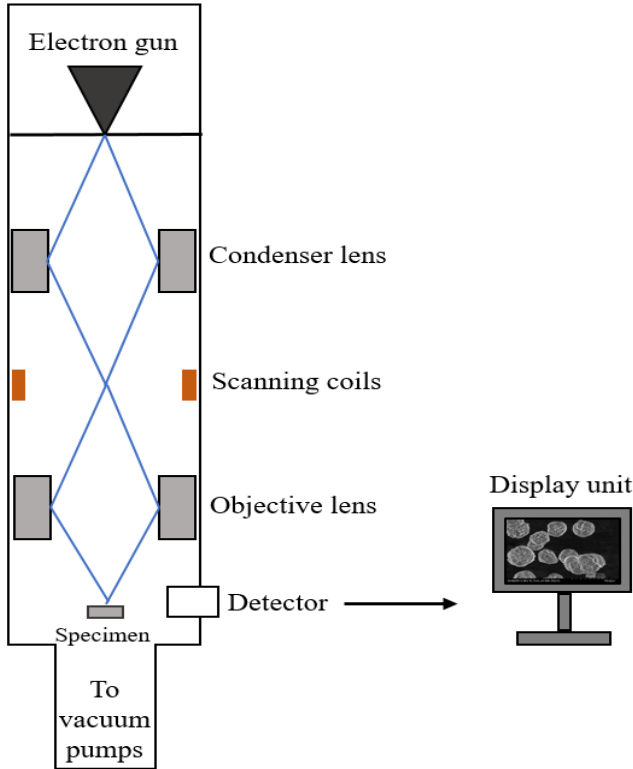
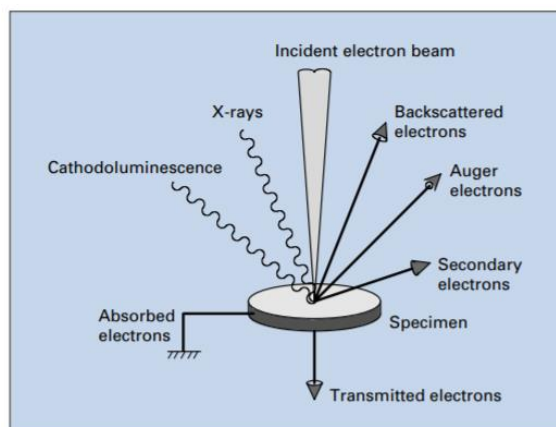


Figure 3-8 Schematics of a scanning electron microscopy. Adapted from (53).

A SEM provides the emission of various electrons and electromagnetic waves. An overview of signals one may obtain and utilize is visualized in Figure 3-9 followed by a short presentation of secondary (SE), backscattered (BSE) electrons and charging for non-conductive samples relevant for this thesis.



**Figure 3-9 Overview of signals possible to obtain by the SEM (54).**

Secondary electrons arise from the atoms in the specimen due to interactions between the electron probe and the specimen followed by inelastic scattering. The electrons have energy less than 50 eV. Low energized electrons do not penetrate deep into the surface (depth of 5-50 nm) (53). Therefore, they collect topology information and are useful in collecting data on specimen edges as they will appear brighter due to more electrons reaching the detector.

Backscattered electrons are electrons that originated in the electron beam. They are backscattered after interacting with specimen atoms and are high energy electrons. Due to the high energy they can penetrate deeper into the specimen (50-300nm) providing compositional information (53). Atoms with a high atomic number will scatter more and will appear brighter than atoms with lower atomic numbers.

Obtaining good imaging of zeolites can be challenging due to their non-conductive nature. Charging is a phenomenon that occurs when the electrons hitting the sample stop at the surface since the electrons cannot flow through the specimen. Accumulation of charge is seen as charging where parts of the image might appear darker or brighter. If the specimen is negatively charged, the difference in voltage between the detector and specimen becomes large, more electrons will reach the detector and the image will appear brighter. If the specimen is positively charged, the voltage difference is smaller leading to fewer electrons reaching the detector. Therefore, the image might appear darker. This can be adjusted by coating the specimen with a conductive material. However, if the amount of charging is not too significant, it is possible to reduce the electron beam hitting the sample. Particle size, specimen stage and sample preparation also influence the charging level and can be attempted modified for desired imaging (54). Excessive build-up of charge on samples can also lead to samples moving and a blurring of any images taken.

Scanning electron microscopy is also applied for elemental analysis. The instrument has an X-ray detector, allowing the collection of energy-dispersive X-rays for element identification. When a sample is irradiated by an incident beam, electrons within the shell of the sample can be excited. If an electron is excited from a shell, an electron-hole is created. The vacant orbits can be filled by electrons of higher energy states, which leads to emissions of x-rays corresponding to the energy difference between the lower and higher energy state. The X-ray energies emitted are characteristic of different elements in the sample. Therefore, this technique allows the elemental analysis of the composition of a specimen (54).

### **3.3.3 Thermogravimetric analysis**

Thermogravimetric analysis (TGA) is a technique used to measure the mass change of a sample as a function of temperature. Its main purpose is to analyze the decomposition and thermal stability of a material. In zeolite science, it is commonly applied to determine dry sample weight due to the materials of a high water affinity. It is also applied to determine at which temperature a structure-directing agent (template) is burnt off. This provides valuable information in determining calcination temperature for the synthesized materials. Another purpose is to determine coke content in spent zeolite catalyst samples.

In principle, the method is based on heating a sample up to temperature with the desired heating rate and ramp while measuring the mass change. This can be done in a reactive or non-reactive atmosphere. TG curves are commonly plotted as percentage mass as a function of temperature or scanning time. The microbalance which measures the mass change commonly has a capacity to measure down to  $\pm 1\mu\text{g}$ , with a maximum mass of 100 mg (55).

### **3.3.4 Gas-physorption**

A valuable tool in determining the amount of gas adsorbed on a solid material at a certain temperature and pressure is gas-physorption. For zeolitic materials, this method has proven to be useful in gaining information on the porous structure because it can provide knowledge about the surface area and pore volume which are important when considering the catalytic activity of a material.

When introducing an adsorbate to the adsorbent, commonly  $\text{N}_2$  or Ar, the gas will be pysisorbed on the zeotype and gradually cover the empty surface (Figure 3-10). After a

monolayer is formed, it is possible to determine the monolayer volume which can further be employed to estimate the surface area (56).

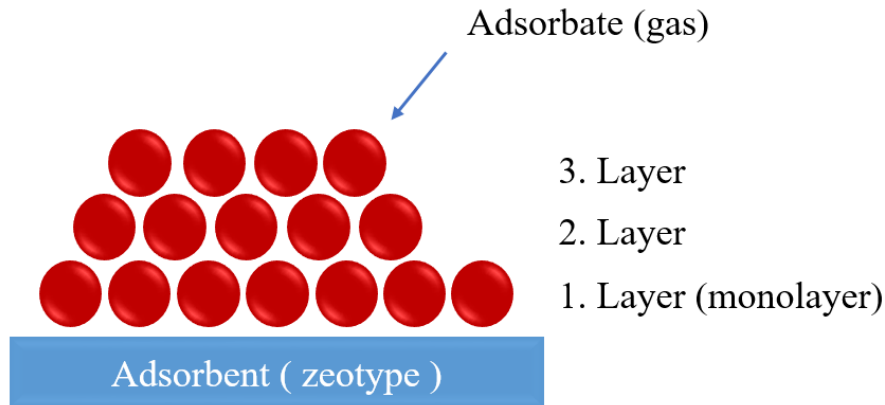


**Figure 3-10 Schematic of physisorption. Produced by author.**

To evaluate the surface area a physisorption isotherm is most commonly converted to a Brunauer – Emmett – Teller (BET) plot. This method was first described in 1938 for non-porous materials and is therefore essentially erroneous when applied to microporous materials (57). However, it provides an evaluation method that is easy to quantify and interpret. It is especially adept for relative comparison between similar materials. The method is applicable when one assumes: (i) all adsorption sites are equivalent. (ii) The adsorbates do not interact with each other, and (iii) each molecule adsorbed in a layer has the potential to function as an adsorption site for the next layer.

The linearized BET-equation is shown below;

$$\frac{P}{V(P_0 - P)} = \frac{I}{cV_m} + \frac{(c - 1)}{cV_m} \left( \frac{P}{P_0} \right) \quad (3-5)$$

Here,  $P$  is the equilibrium pressure,  $P_0$  is the saturated vapor pressure,  $V$  is total volume adsorbed,  $V_m$  is the volume of the monolayer,  $c$  is a constant indicating the adsorbent-adsorbate interactions and  $\frac{P}{P_0}$  is the relative pressure. A typical BET-plot will show a straight



line with  $\frac{P}{V(P_0-P)}$  as a function of  $\frac{P}{P_0}$ .  $V_m$  can be determined from the slope and intercept in the BET-equation. Combined with the known amount of moles of the gas for this volume and the area of the cross-section for one single molecule, the area of the adsorbing surface can be calculated (57).

### 3.3.5 Fourier transformed Infrared spectroscopy

Fourier transformed Infrared spectroscopy (FT-IR) involves the interactions of infrared light with molecules. When molecules are irradiated in the infrared region, molecular vibrations and rotations can be excited, if the dipole moment changes in the action. The excitation of a vibration raises the vibrational level with a quantum number  $n$  to a higher level. These phenomena are exploited in the technique of infrared spectroscopy and provide fundamental information about vibrations and energy transitions in molecules. In the fields of catalysis and zeolite science, IR – measurements have been applied to investigate adsorbed species on catalyst surfaces as well as their interactions. It has also proven to be an applicable method for studying density/concentration of different acid sites by adsorption of probe molecules.

To comprehend how the infrared spectrum is obtained, it is common to consider a simple model derived from classical mechanics. Considering a harmonic oscillator, the vibration frequency of a diatomic molecule is;

$$\nu = \frac{1}{2\pi} \sqrt{\frac{k}{\mu}}, \quad \mu = \frac{m_1 m_2}{m_1 + m_2} \quad (3-6)$$

Where  $\nu$  is the vibrational frequency,  $k$  is a measure of the bond strength between two diatomic molecules (the force constant),  $\mu$  is the reduced mass and  $m_1$  and  $m_2$  are the masses of the two atoms vibrating. Therefore, the vibrational frequency is higher when the force constant is high and the masses of the vibrating atoms are small. (58)

The design of a Fourier transformed infrared spectrometer during measurements consists of light entering the interferometer (the center of the FT-IR spectrometer) directing light to the beam splitter. Then the split beam is directed at both a fixed and moving mirror respectively followed by recombination before it finally reaches the sample cell, as illustrated in Figure 3-11. Compared to conventional techniques it has the advantage of recording light of all frequencies simultaneously in the detector. After reaching the detector the IR radiation is converted to an interferogram by the use of an interferometer. The interferogram shows

intensity on the Y-axis and time on the X-axis. To obtain the IR-spectrum where the X-axis is a function of frequency, it is Fourier transformed by the use of a mathematical operation (59).

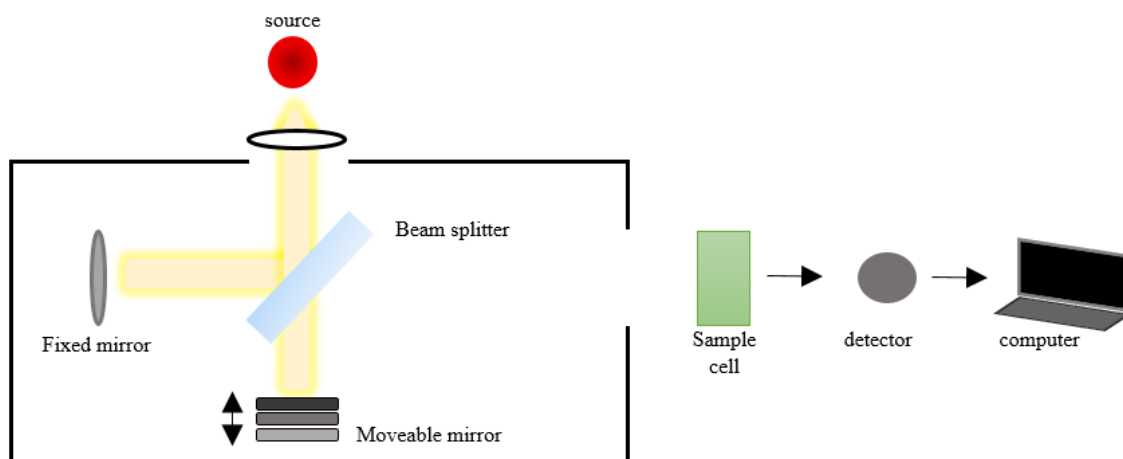
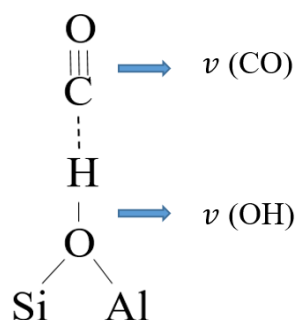


Figure 3-11 Schematic diagram of a Fourier transform spectrometer. Adapted from reference (58).

### CO-probing

CO is commonly applied as a probe molecule for the characterization of oxide surfaces. Carbon monoxide is a weak base and will interact with hydroxyl groups present in the material. The  $\nu$  (OH) stretching is dependent on the acidity of the hydroxyl group but also the cations, which the hydroxyl groups are connected to. Therefore one can expect different OH-stretching frequencies when probing a zeotype with CO. Adsorption measurements are performed at 77K. This is strategic in means that only materials with strongly acidic OH groups can be detected. CO is often preferred as a probe due to its small size, its weak interaction with cations, resulting in a reversible interaction with the sample (60).

The  $\sigma$  orbital in CO has an antibonding character. When CO interacts with the Brønsted sites (Figure 3-12), the CO bond is strengthened due to the donation of  $\sigma$  electrons. The vibrational frequency is therefore shifted towards higher frequencies. Opposite, the OH bond is weakened and the vibrational frequency shifts towards lower frequencies (61).



**Figure 3-12 CO interacting with a Brønsted site (62).**

### 3.3.6 Microwave Plasma atomic emission spectroscopy

Microwave Plasma atomic emission spectroscopy (MP-AES) is an analytical technique applied to determine the elemental composition of a sample. In zeolitic science MP-AES provides an alternative analysis method compared to commonly applied Energy-dispersive X-ray spectroscopy. (EDX) While EDX proves to be valuable and highly used, it suffers the disadvantage of commonly having instrumentation parts included sample holders consisting of aluminum, which is the main building T-atom in zeolitic materials. This knowledge might lead to analysis errors due to sample and instrumentation interference, lowering its credibility. MP-AES provides sample quantification while avoiding this disadvantage.

To determine the concentration of an element in a sample, several steps follow as seen in Figure 3-13. Considering a zeolitic material, the sample is commonly dissolved by hydrofluoric acid (HF) dissolution and further treated to form a homogeneous solution in advance of the analysis. The prepared sample in its liquid form is converted to an aerosol by using a nebulizer and a spray chamber. Formed aerosol is further introduced to the center of hot plasma (6000 K) that is fuelled by a nitrogen generator. In the plasma, the aerosol will dry and decompose before atomizing leading to electron excitation. When excited electrons return to lower energy states, light is emitted at characteristic, element wavelengths. After emission, a photon detector collects the data at a selected wavelength range. The instrument determines the concentration of the sample by comparing measured samples towards a plotted calibration curve. The calibration curve is constructed by measuring standard solutions prepared in an expected ppm range of desired elements (63).

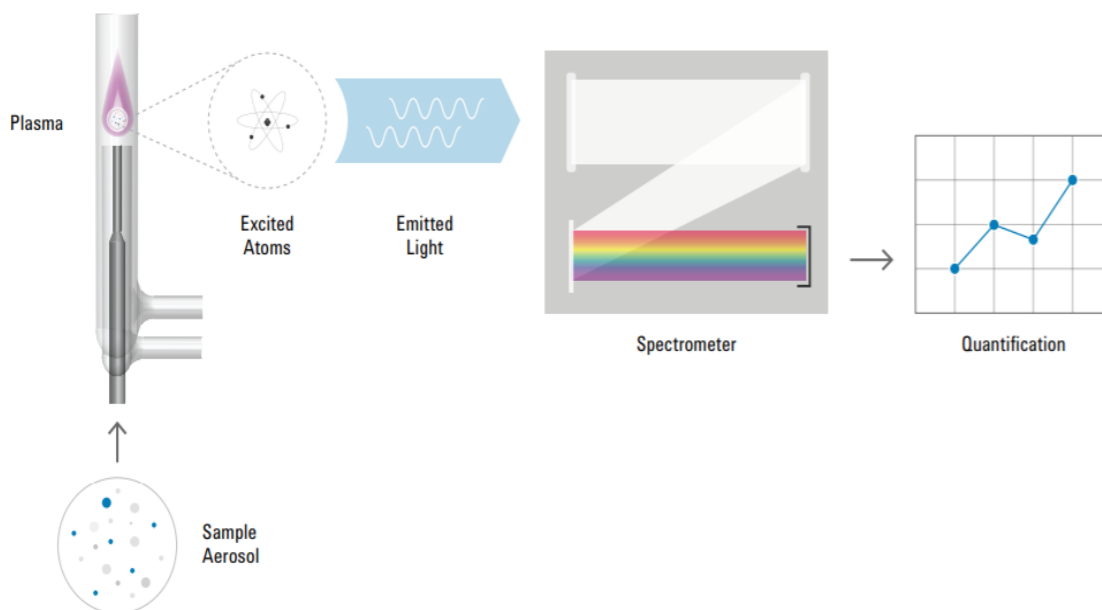


Figure 3-13 Schematic of MP-AES adapted from (63).

### 3.3.7 Simulations for surface area determination

The surface area of a material can be simulated with Monte Carlo approaches. Monte Carlo calculations are based on randomized probability distributions. The mathematical techniques are integrated into the software of use. While experimental methods for surface area determination are appreciated, computational chemistry is a valuable supplement.

To calculate the surface area directly from structural features, a geometric approach may be applied by the simple Monte Carlo integration technique. Two different surfaces can be calculated from a given structure.

- i) Connolly surface area
- ii) Solvent accessible surface area

The Connolly surface area is calculated from the bottom of a probe molecule rolling on a surface and the solvent accessible surface area is calculated from the center of the probe molecule rolling on the surface. This is visualized in Figure 3-14. It has been argued that the solvent accessible surface area is more accurate for surface area calculations on porous materials compared to Connolly surface area (64). In this thesis, computational simulations are used as a supplement to empirical measurements for comparative purposes and not as an

independent research topic. Therefore, the reader is referred to the work of Düren et al. (64) for further elaboration. It will not be further discussed here.

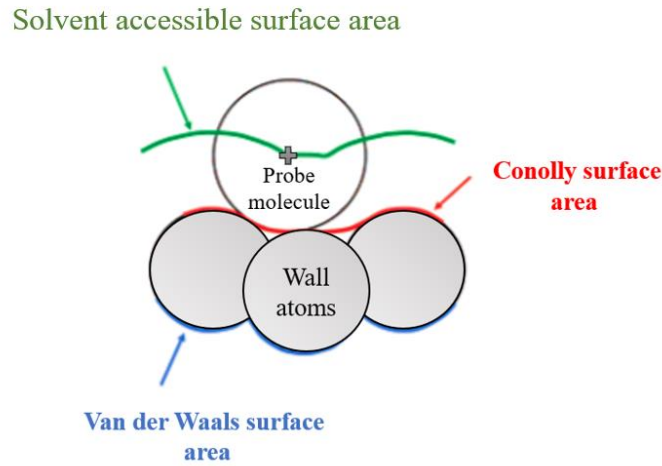


**Figure 3-14 Illustration of different surface areas adapted from (60).**

An adsorption isotherm for the desired material can also be simulated by grand canonical Monte Carlo simulations. This type of simulations estimates sorbate loading at a certain temperature at a fixed pressure. Simulation experiments will result in a plot of sorbate loading as a function of fugacity. Using the maximum loading and unit cell composition of the material one can calculate the specific surface area. The calculations will be described in the next paragraph.

Defining Maximum loading as  $X$  and knowing the area of one  $N_2$  molecule is  $1.62 \times 10^{-19} \text{ m}^2$ , surface area (SA) is  $1.62 X \times 10^{-19} \text{ m}^2$ . The molar mass of an unit cell ( $M_U$ ) in grams/mole can be calculated by

$$M_U = \sum_{i=1}^n M_i n_i \quad (3-7)$$

where  $M_i$  is the molar mass of element  $i$ , and  $n_i$  is the number of atoms for element  $i$  in the unit cell. Specific surface area (SSA) in  $\text{m}^2/\text{g}$  can be obtained by

$$SSA = \frac{SA \times N_A}{M_U} \quad (3-8)$$

Here  $N_A$  is the Avogadro's constant at value  $6.022 \times 10^{23} \text{ mole}^{-1}$ .

# 4 Experimental

## 4.1 Methodology for the screening of SAPO-11 synthesis

### 4.1.1 Determining a method for synthesis approach

In advance of the laboratory work, synthesis routes were investigated and selected. SAPO-11 was successfully synthesized by Blasco et al. (25) as previously shown in Table 3-1. The synthesis referenced to the patent of Lok et al (51). However, Blasco did not describe the method chosen nor the number of reactants mixed for the synthesis gel. While investigating the patent of Lok et al, example 18 was the only route corresponding well to the molar ratios for synthesis gel given in the article of Blasco. Blasco *et al.* gave 195 °C as synthesis temperature, while the patent stated 200 °C. In advance of choosing this method, the molar ratios in example 18 were recalculated. This revealed an error in molar ratios of calculated water content (Appendix A). Therefore, this synthesis approach was disregarded. On the search for a valid synthesis route, example 15 (51) was finally chosen from the work of Lok et al.

### 4.1.2 Initial synthesis approach

In the initial crystallization attempts, a simplified synthesis route adapted from Lok et al. was applied (51). In the original recipe, a large synthesis mix with desired chemicals was mixed. Then one-third of this mixture was mixed with the template and further used. For the first attempts of this synthesis route applied in this thesis, the original recipe was scaled down to one third directly with the purpose of avoiding chemical waste. Chemicals were mixed with the amount described in Table 4-1. First water and Aluminum isopropoxide were mixed. Phosphoric acid was then added to the solution followed by the addition of silica. After mixing for some time, the template was added. No fixed stirring time was set. The gel was transferred to four liners as visualized in Figure 4-1. 4 liners were used to investigate the reproducibility and if there is a difference in which part of the synthesis mix used. Liners were enclosed in autoclaves and were heated statically under autogenous pressure for 133 h at 150 °C. Products were washed with distilled water and centrifugation before dried.

**Table 4-1 List of chemicals for initial synthesis route.**

<b>Chemicals</b>	<b>Amounts weighed in (g)</b>
H <sub>2</sub> O type II	53.3
Phosphoric acid (85%)	17.1
Aluminum isopropoxide	30.23
95% Fumed silica	0.47
Dipropylamine	7.4

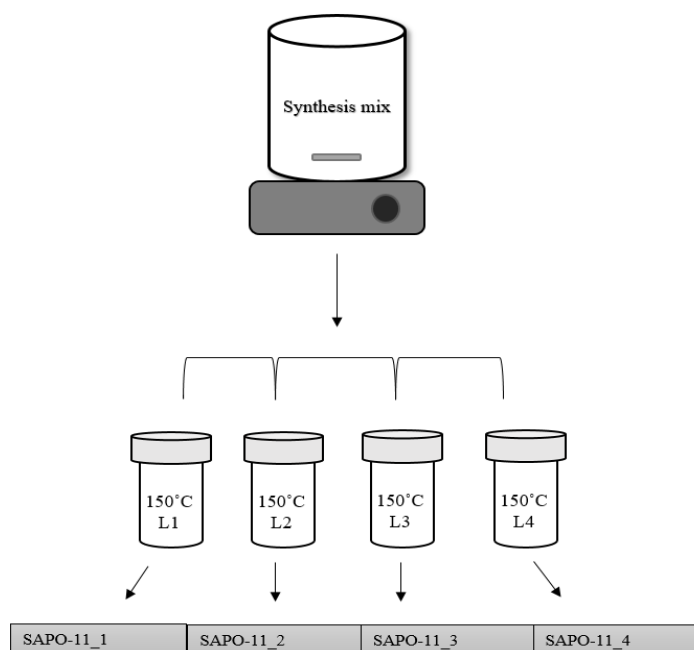


**Figure 4-1 Initial synthesis approach scheme. Chemicals were purchased from Sigma Aldrich. The synthesis mix is equally divided and transferred to four liners for further treatment. Produced by the author.**



### 4.1.3 Modified synthesis approach – tuning the kinetics

With the purpose of developing a successful synthesis approach for the development of SAPO-11, a modified synthesis route was developed based on the work of Lok. The final aim was to map out at what region SAPO-11 crystals had the highest crystallinity and regularity. 4 parameters were investigated in the synthesis route.

- i) Difference between upper and lower parts of the synthesis mix.
- ii) Influence of temperature
- iii) Influence of static crystallization
- iv) Influence of rotational crystallization

Chemicals applied in this experiment were purchased from Sigma Aldrich and the amounts weighed out are listed in Table 4-2. For reproducibility purposes, the experiments were also carried out with a different aluminum isopropoxide purchased from Fluka.

**Table 4-2 Modified synthesis list of chemicals**

Chemicals	Amounts weighed in (g)
H <sub>2</sub> O type II	160
Phosphoric acid (85%)	51.3
Aluminum isopropoxide	90.7
95% Fumed silica	1.4
Dipropylamine added to one-third	7.4
Dipropylamine added to two-third	14.8

All reactants were mixed as illustrated in Figure 4-2. For this approach, a fixed stirring time was set for each step of mixing of reactants. Aluminum isopropoxide was ground in a mortar before stepwise addition of water. The phosphoric acid was diluted with 1/3 of total water content and added dropwise to the system to avoid rapid gel formation. Then the silica source was added to the mixture and stirred. After the desired stirring time two-thirds of the gel by weight was transferred to an empty beaker. Template was added stepwise to the two-thirds of the synthesis mixture as well as for the one-third. The two mixtures were left for stirring overnight.

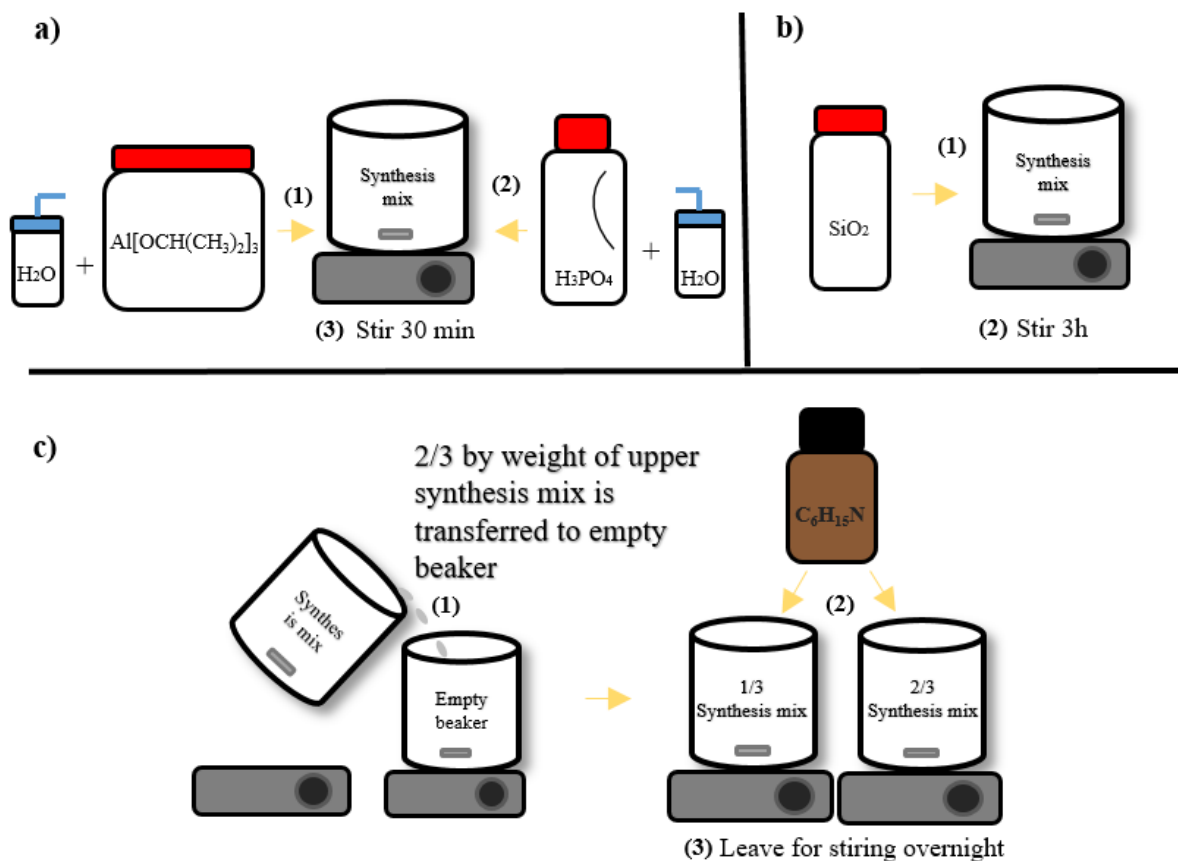


**Figure 4-2 Synthesis route scheme for the modified synthesis. Produced by the author.**

To investigate why it is beneficial to divide the synthesis mix as proposed in the original recipe, the top two-thirds of the mixture was kept and further treated. The synthesis mixtures were treated hydrothermally at the temperatures 150,160,170 and 180 °C, both under static and rotating conditions. Figure 4-3 shows a step by step illustration of how the mixtures were treated. For each experiment, four routes were investigated and labeled as followed by the notation in the figure.

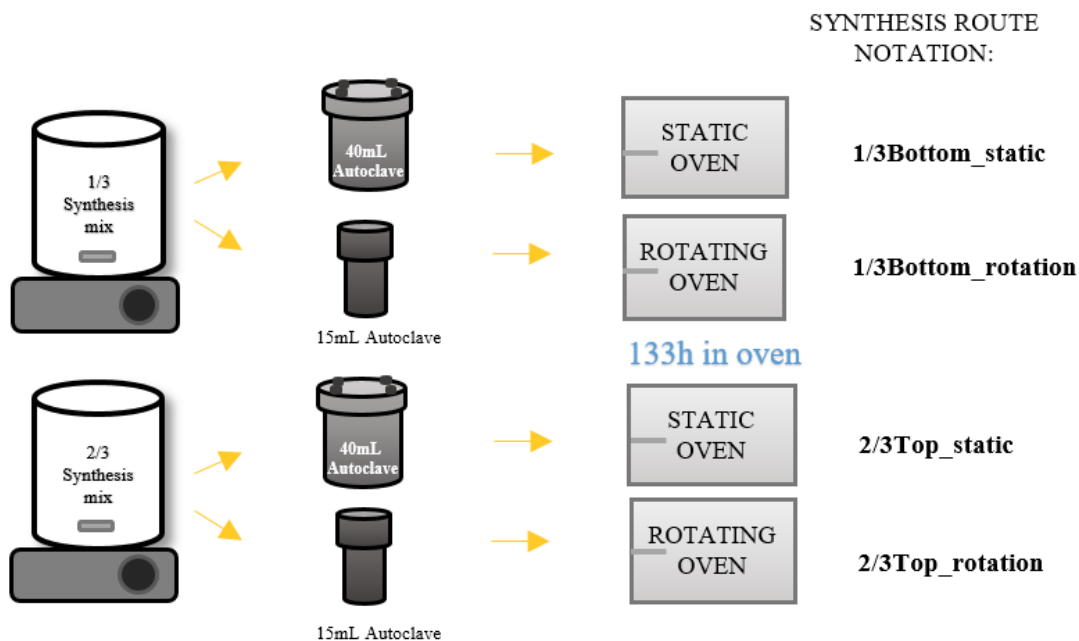


**Figure 4-3 Scheme of further treatment for the prepared synthesis mixture for one experiment. Produced by the author.**

After hydrothermal treatment, samples were collected and transferred to 125 ml plastic bottles. The bottles were filled with distilled water (type II) and stirred with a spatula before vigorous shaking by hand. When the product was fully suspended, samples were centrifuged 10 minutes at 3000-3500 rpm. After centrifuging the precipitate was kept and the solvent was decanted. This procedure was repeated 3 times. Following the washing procedure, precipitant was collected and transferred to a porcelain crucible and left for drying in a heating cabinet at 40 °C overnight.

The samples collected were labeled after experiment number and heating conditions and are for clarity presented below in Table 4-3.

**Table 4-3 Sample names for recovered samples after synthesis. The experiments are labeled from 1-4 with regards to crystallization temperature. For each experiment at one desired temperature, the upper part (2/3top) of the synthesis mixture is heated both statically and with rotation. The lower part of synthesis mix (1/3bottom) is also heated similarly, statically and with rotation.**

<b>Experiment nr.</b>	<b>Temperature (°C)</b>	<b>Sample name SAPO-11</b>
1	150	1-1/3Bottom_static
		1-2/3Top_static
		1-1/3Bottom_rotation
		1-2/3Top_rotation
2	160	2-1/3Bottom_static
		2-2/3Top_static
		2-1/3Bottom_rotation
		2-2/3Top_rotation
3	170	3-1/3Bottom_static
		3-2/3Top_static
		3-1/3Bottom_rotation
		3-2/Top_rotation
4	180	4-1/3Bottom_static
		4-2/3Top_static
		4-1/3Bottom_rotation
		4-2/3Top_rotation

#### 4.1.4 Calcination

Calcination was performed to remove the template from the structure of the zeotype. SAPO-11 has one-dimensional pore structures. The zeotype is vulnerable to mass transfer limitations due to pore blocking, (65) Different routes for calcination were attempted. Figure 4-4 shows the calcination route performed in ambient air (Figure 4-4a) and under oxygen flow (Figure 4-4b) at temperature  $T_1$  and  $T_2$ . The instrument used for calcination in air atmosphere, was static air calcination oven (Nabertherm GmbH). A range of samples between 200 - 400 mg were crushed in a mortar and transferred to a crucible before heating. Calcination in oxygen flow was performed in an oxygen tubular calcination oven (Temperature vacuum tube furnace GSL-1100) with a flow of 59 ml/min.

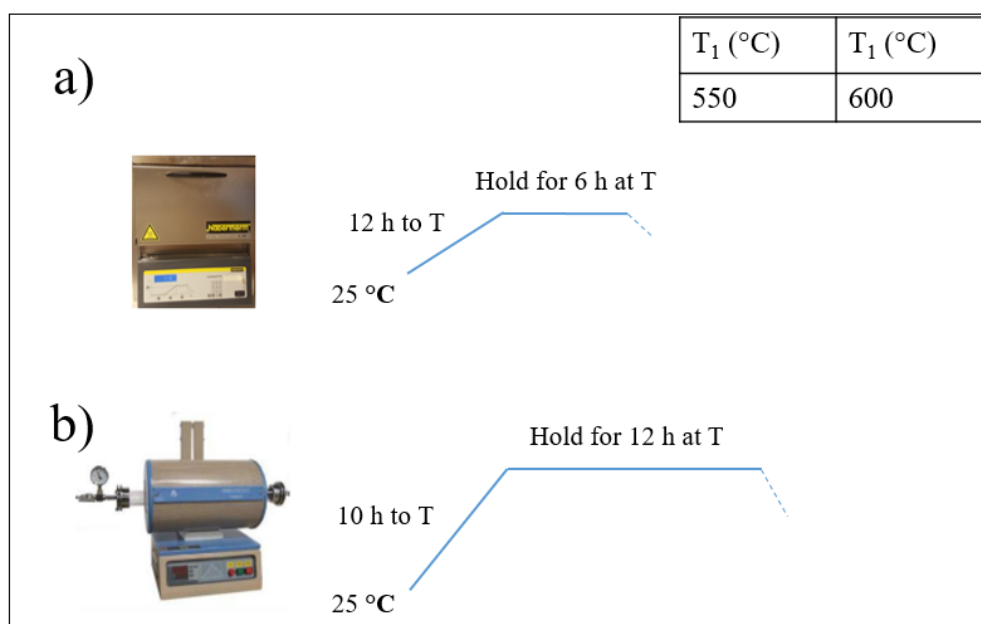


Figure 4-4 Calcination routes, where a) is in air atmosphere and b) is in oxygen atmosphere.

## **4.2 Characterization**

### **4.2.1 Powder X-ray diffraction**

Powder x-ray diffraction was applied as a characterization technique to investigate the material phase and effect of temperature upon template removal. Diffractograms were collected measured in a  $2\theta$  range of 2-40, with a timescale of 2. Samples were prepared in deep sample holders. All samples were measured on a Bruker D8 Discover Diffractometer, using a Cu  $K\alpha$  radiation where  $\lambda$  was 1.5406 Å. Data were processed with the software Topas 5.0 and further treated in Origin 2017.

### **4.2.2 Scanning electron microscopy**

Scanning electron microscopy was used for imaging. Images were taken in normal mode to obtain particle shape information for SAPO -11 samples obtained with different synthesis conditions. Data collected was used to determine particle diameter by further processing in the software Image J. Deceleration mode was applied for high magnification imaging for crystal topology determination.

The samples were prepared on carbon tape using a multiple sample holder. All data were collected on a Hitachi SU8230 instrument with an acceleration voltage between 1 and 5 kV. Images were obtained at 5 kV with 700 and 5000 magnification to obtain comparative data. The influence of heating treatment upon calcination was imaged at a magnification of 3000 for clear visualization. Images taken in deceleration mode were taken at low acceleration voltage (1 kV) for topology purposes and magnified to the nanoscale.

In advance of EDS measurements, the samples were pressed to pellets at 1 ton and placed on carbon tape on a multiple sample holder. The acceleration voltage was set to 10 kV.

### **4.2.3 Thermogravimetric analysis**

Thermogravimetric analysis was applied to determine the decomposition temperature of the template in the materials synthesized in different conditions. It was also used to study the water content of the SAPO-11 samples. The method was employed to set the appropriate calcination temperature and to determine the degree of template removal in the SAPO-11 materials after calcination. For each measurement 30 – 35 mg sample was weighed out and placed in  $Al_2O_3$  crucible and placed on a multiple sample holder for running. All samples

were measured in NETZSCH STA 449F3. The measurements were run with atmospheric gas flows of 5/20 mL/min of N<sub>2</sub>/O<sub>2</sub> and 20 ml/min N<sub>2</sub> as protective gas. The heating conditions were 30°C (5 °C/ml) up 900 °C and cool down with an identical ramp. All data were first processed with NETZSCH thermal analysis before further treatment in Origin 2017.

#### **4.2.4 N<sub>2</sub>-physisorption**

N<sub>2</sub>-physisorption was used to investigate the porosity of the materials in terms of surface area. All sample cells were weighed before and after measurement. The sample mass weighed out for one measurement was 30 mg. Measurements performed on BelSorp MINI and samples were pretreated for 3 hours in a vacuum. (0.1 µbar). First hours of pretreatment were done at 80 °C, the remaining two hours were heated at 200 degrees °C. Before measurement, the heater connected to the instrument was replaced with a dewar filled with liquid nitrogen (77 K). For the first measurement, a blank cell was used to measure the dead volume of the cell. BET data was found from the adsorption isotherm constructed from the measurement. A linear fitting was performed from a p/p<sub>0</sub> range of 0.0-0.1.

#### **4.2.5 Fourier transformed infrared spectroscopy**

Approximately 5 mg self-supporting pellets were pressed at 1 ton and placed in a gold envelope inside the IR cell (KBr windows). Prior to measurements, samples were pretreated in situ at temperatures up to 400 °C to remove adsorbed water and other impurities. Low-temperature FT-IR was performed at 100 K on a Bruker Vertex 80 with a DTGS detector. Spectra were collected with 64 scans and 4 cm<sup>-1</sup> resolution.

#### **4.2.6 Microwave plasma atomic emission spectroscopy**

5 standards and one blank sample were made for the elements Si, Al and P from 100 and 1000 ppm stock solutions (Table 4-4). Commercial SAPO-11 as well as selected synthesized samples were dissolved in HF\* in advance of measurement. 50 mg of sample was dissolved in 1 ml 25 % HF and neutralized with 10 ml of 10 wt% Boric acid and filled with distilled water to form a 50 ml solution. 10 ml from the 50 ml solution was pipetted out and diluted in a 100 ml polypropylene, volumetric flasks to correspond with standards concentrations prepared.

**Table 4-4 Standard concentrations for prepared standards.**

Standard nr	Standard concentration (ppm)		
	Si	Al	P
1	1	15	10
2	3	20	15
3	5	25	20
4	7	30	25
5	9	35	30

**\*Special precautions and HSE considerations were taken in advance of working with hydrogen fluoride (HF). The corrosive acid is considered a health hazard and a strict procedure was followed during all HF treatment**

The analysis was carried out with an Agilent 4100 MP-AES instrument with a Plasma temperature of 6000 K and a pump speed of 15 rpm. The photon detector was a charge-coupled device.

## **4.3 Catalytic testing for methanol to olefins conversion**

### **4.3.1 Experimental setup**

Catalytic tests for the conversion from methanol to olefins were performed on a suitable testrig. (Figure 4-5) In advance of the experiment, the samples were pressed at 4.5 tons and sieved into fractions of 425-250  $\mu\text{m}$ . 200 mg of sieved sample was introduced to a fixed bed flow quartz reactor with an 8 mm bed diameter. The reactor was mounted in an oven and connected to the gas manifold. A thermocouple was introduced into a 3 mm wide quartz sleeve into the catalyst bed for temperature monitoring. Gas flows were controlled by mass flow controllers for selected gases (line 1, 3 and 5). Helium was bubbled through liquid methanol and was fed to the reactor through line 3. The gases used for this experiment is Ar, He, N<sub>2</sub> and O<sub>2</sub>. After each experiment, the reactor was dismantled and cleaned thoroughly with acetone three times.



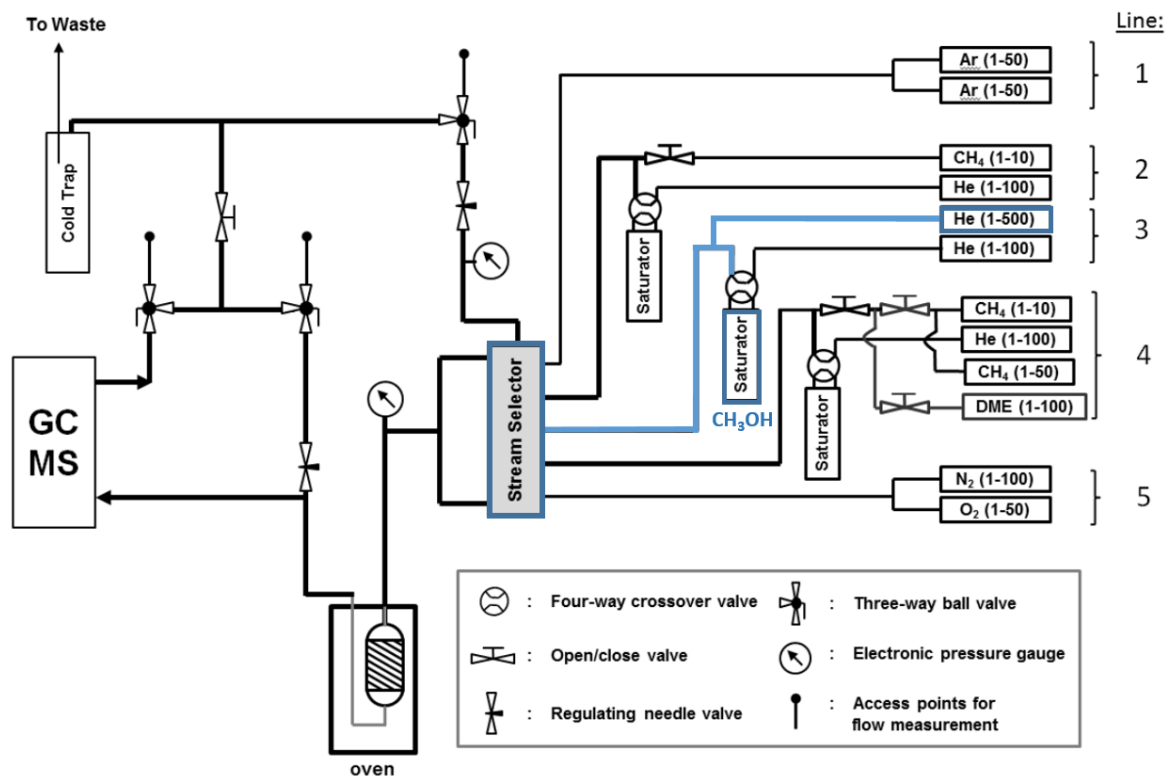


Figure 4-5 Testrig design for the methanol to olefins reaction. Blue line indicates the methanol feed.

### 4.3.2 Test conditions

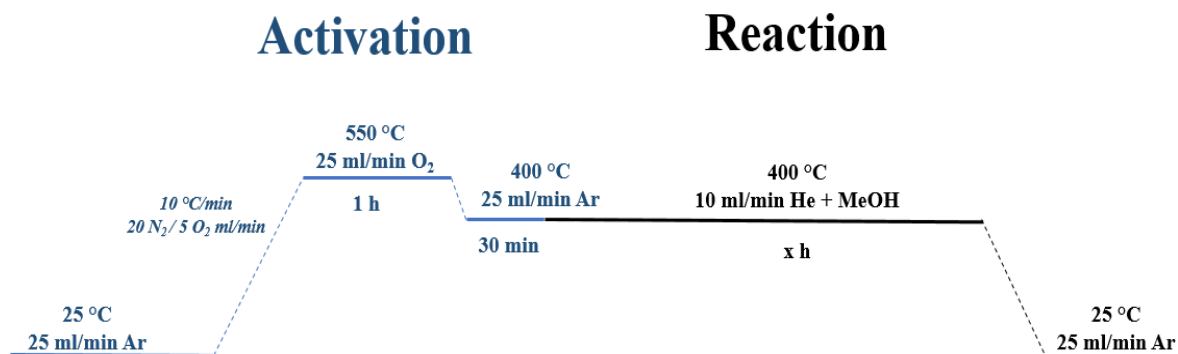
Reaction conditions are presented in Table 4-5. The conditions were selected to be comparable to the work of Pinilla-Herrero et al, where a selection of SAPOs was investigated for their catalytic performance (66).

Table 4-6 Test conditions for the methanol to olefins reaction during experiment. The conditions were kept constant for all samples measured.

$t_{\text{Reaction}}$ (°C)	$P_{\text{Reaction}}$ (bar)	WHSE (h <sup>-1</sup> )	Flow <sub>He+MeOH</sub> (mL/min)	$t^*_{\text{MeOH}}$ (°C)	$P_{\text{MeOH}}$ (bar)
400	1	0.5	10	20	0.13

\*Temperature was controlled by a waterbath.

Each experiment was performed during a timescale of 24 h and required an activation step in which the sample was treated in pure oxygen before being flushed with argon to remove residuals of oxygen. Figure 4-6 shows a diagram of the activation and reaction process for the experiment with corresponding flows, temperatures and relevant timescales.



**Figure 4-7 Temperature profile and conditions for activation and reaction of the MTO reaction. In blue, activation process, and in black the reaction process. Produced by the author.**

### Effluent analysis

Effluent analysis was performed by an on-line GC-MS instrument (Agilent 7890 with a flame ionization detector and a 5975C MS detector). Two Restek Rtx-DHA-150 columns were used. Hydrogen (Praxair purity 6.0) was applied as the carrier gas. Figure 4-8 shows the GC method applied. Response factors were given for methanol and DME. The effluent from the reactor was analyzed after 5 minutes of reaction and after every 45 minutes. Each reaction was left for 28 runs.

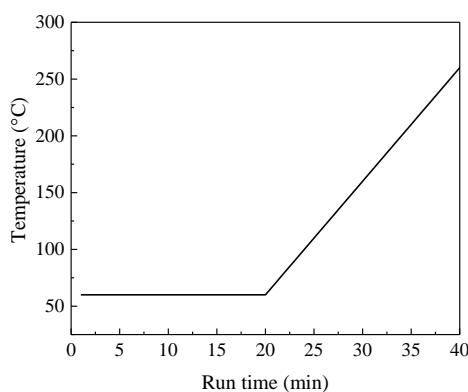


**Figure 4-8 Temperature profile for GC. The initial temperature is 60 °C and holds for 20 minutes. After 20 minutes the temperature is increased to 260 °C with a ramp rate of 10 °C/min.**

## Quantitative analysis

The conversion was calculated from integrated peak area determined from the GC, where  $A_{\text{Tot}}$  is the area of total hydrocarbon products and  $A_{\text{MeOH+DME}}$  is the area of the feed methanol and dimethyl ether (Equation (4-1)).

$$\text{Conversion} = \frac{A_{\text{Tot}} - A_{\text{MeOH+DME}}}{A_{\text{Tot}}} \times 100\% \quad (4-1)$$

Selectivity was calculated from the area of the fraction of hydrocarbon ( $A_X$ ) divided by area of products ( $A_{\text{products}}$ ) (Equation (4-2)).

$$\text{Selectivity} = \frac{A_X}{A_{\text{products}}} \times 100\% \quad (4-2)$$

# 5 Results

All results will be presented in this section. This chapter will cover the applied methodology of determining the synthesis method, initial and modified synthesis results and standard characterization with various techniques. Promising samples identified from standard characterization are further characterized for acidity and framework investigation. Lastly, catalytic testing will be presented for selected samples.

## 5.1 Mapping the synthesis route for the synthesis of SAPO-11

### 5.1.1 Synthesis methodology

The initial synthesis method presented in this thesis at 150°C in static air turned out to be non-successful. The experiment was repeated 3 times, with little success. Samples were examined by PXRD and SEM. The product collected was mostly amorphous. This method was disregarded as a good synthesis route and is presented in Appendix B.

The modified synthesis approach including synthesis mixture separation, (Lok et al. example 15 (51)) and different synthesis conditions was examined by PXRD and SEM. The samples were compared with commercial SAPO-11 purchased from Alfa Chemistry. Yield calculations were performed to investigate the amount of product collected. Further on, selected samples were attempted calcined. Thermogravimetric analysis was applied to investigate template removal.

### 5.1.2 Yield calculations for the modified synthesis approach.

Yield calculations were done for all 4 experiments to obtain information regarding the efficiency of the synthesis. The results are presented in Table 5-1 and imply that there is a general high yield in this synthesis method (Appendix C).

**Table 5-1 Yield calculations for the modified synthesis approach.**

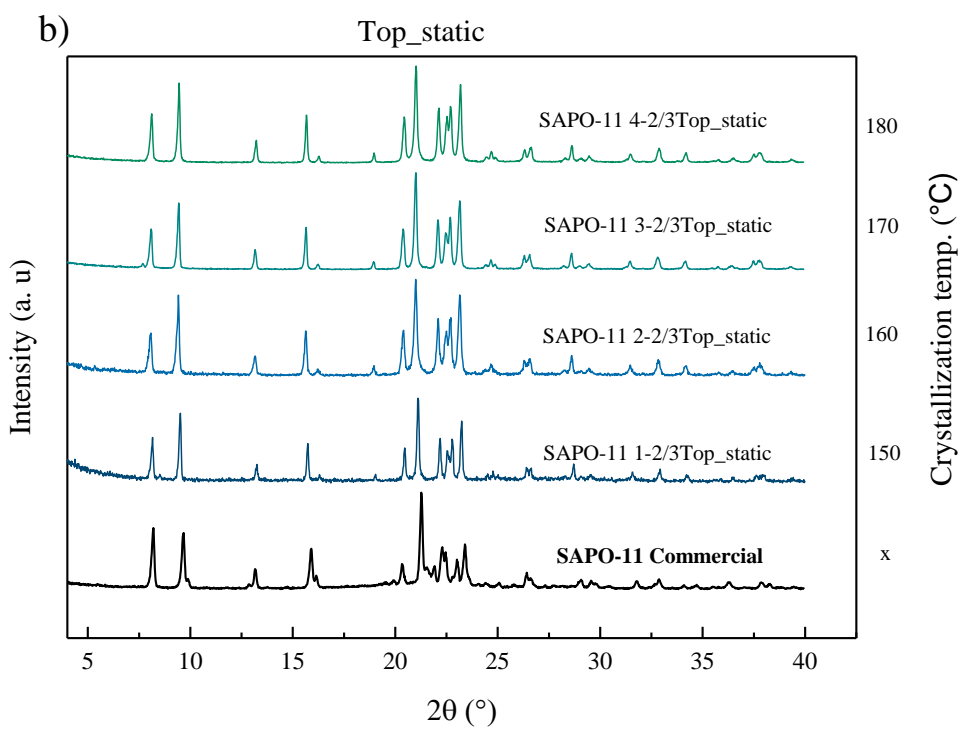
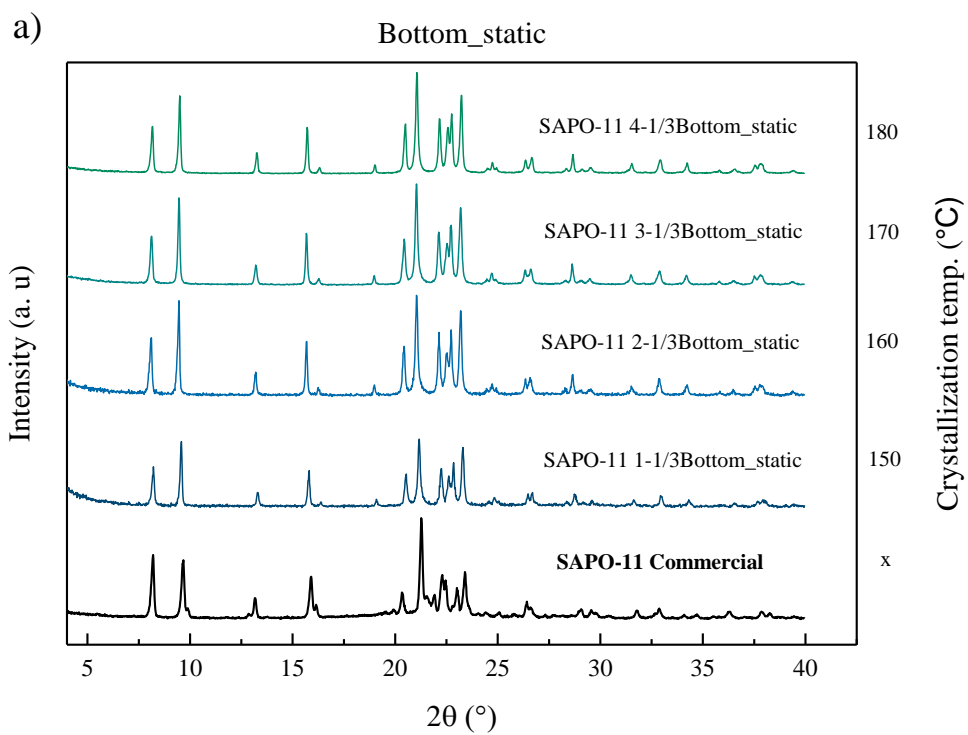
<b>Experiment nr.</b>	<b>Temperature (°C)</b>	<b>Sample name: SAPO-11</b>	<b>Yield (%)</b>
1	150	1-1/3 Bottom_static	64
		1-2/3 Top_static	45
		1-1/3 Bottom_rotation	82
		1-2/3 Top_rotation	73
2	160	2-1/3 Bottom_static	91
		2-2/3 Top_static	59
		2-1/3 Bottom_rotation	60
		2-2/3 Top_rotation	84
3	170	3-1/3 Bottom_static	83
		3-2/3 Top_static	61
		3-1/3 Bottom_rotation	83
		3-2/3 Top_rotation	83
4	180	4-1/3 Bottom_static	75
		4-2/3 Top_static	85
		4-1/3 Bottom_rotation	65
		4-2/3 Top_rotation	69

## 5.2 Standard Characterization

### 5.2.1 Powder X-ray diffraction

Diffraction patterns for the synthesized samples of SAPO-11 are shown in Figure 5-1. The commercial sample of SAPO-11 was set as a reference to evaluate the diffraction patterns, and is hence presented together with the synthesized samples. From the diffraction patterns, one initially observes clear differences in the reflections for the commercial sample compared to the synthesized samples. While it appears that the peaks appear at comparable  $2\theta$  values, the commercial sample exhibits a diffraction pattern that is less well defined. An indication of a peak at  $2\theta$  angle of  $34.8^\circ$  is also visible, but not observed for the synthesized samples. Peaks observed in the commercial sample are clearly broader. Peak width can be linked to crystal size, and is inversely related to the crystal size. That means a broader peak can indicate a smaller crystal size (52). Furthermore, the diffraction pattern for the commercial sample contains shoulders, and the peaks are not well distinguished from the background. It gives reasons to believe the commercial sample shows the presence of different phases. Differences in the diffraction patterns between the synthesized samples are also observed. However, all peaks are clearly more defined compared to the commercial sample. Samples prepared hydrothermally under static conditions (Figure 5-1 a) and c) show an increase in intensity as a function of temperature. The peaks are narrower compared to diffraction patterns collected from samples with rotational synthesis conditions. For the synthesis pursued with rotational conditions, not all samples display the diffraction pattern corresponding to SAPO-11. The trend deviates for sample SAPO-11 1-2/3Top\_rotation synthesized at  $150^\circ\text{C}$  (Figure 5-1 d). Here, the diffraction pattern is clearly not SAPO-11. Therefore, this finding was disregarded for further investigation. From the initial observation, samples synthesized with static conditions have the clearest diffraction patterns. To verify that the framework structure of the synthesized samples actually is SAPO-11 (AEL), some samples were investigated by performing Rietveld refinement (Figure 5-2). In this case, the sample SAPO-11 4-1/3Bottom\_static is presented. This selection is based on the diffraction patterns presented, where the sample showed a reasonable quality of peak definition and had the highest intensity. The refinement in Figure 5-2 shows a good fitting where the difference in the calculated and observed diffraction pattern is small. This finding supports the argument of commercial SAPO-11 being of poorer quality. The somewhat higher value of weighted profile R-factor ( $R_{wp}$ ) can be linked to the limitation of the applied refinement technique itself (67). The Goodness of fit (GOF) gives a value of 1.95 ( $R_{wp}/R_{exp}$ )

and supports this argument. Nevertheless, we take note that R factors are not a direct indication of a good or bad fitting. I refer to the work of Brian et al. for a detailed explanation (68).





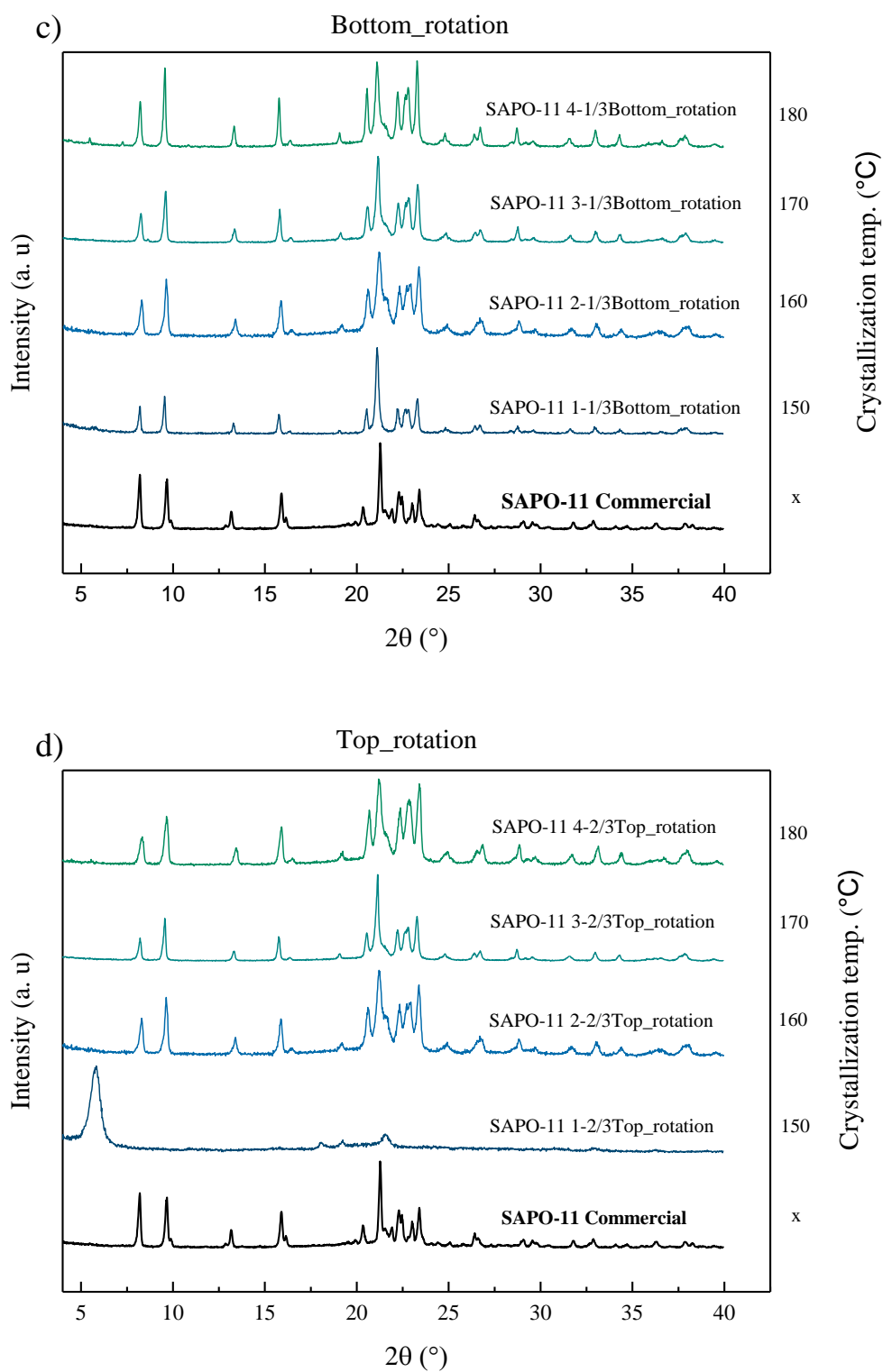


**Figure 5-1** X-ray diffractogram collected from the different synthesis pathways. a,b) are crystallized static from top and bottom of synthesis mixture. b, c) are crystallized rotational from top and bottom of synthesis mixture. Broad peak at  $2\theta = 22,5$  is due to plastic foil from glas plate sample holder applied for samples measured from rotational synthesis conditions. The diffractogram of the commercial SAPO-11 is presented for comparative purposes.

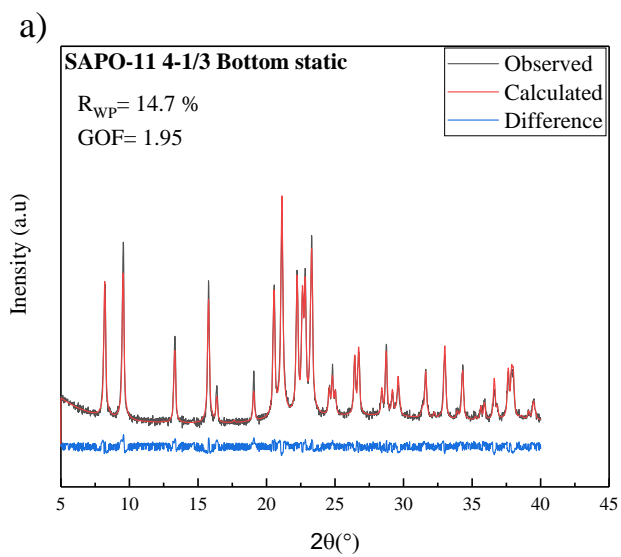


**Figure 5-2 Rietveld refinement for a selected sample, SAPO-11 4-1/3Bottom\_static. In overlapping red is the calculated value from AEL structure, black is measured diffractogram and blue is the difference between calculated and measured.**

## 5.2.2 Scanning electron microscopy

All samples from the modified synthesis were analyzed with SEM. Commercial SAPO-11 was imaged as a reference. The commercial sample of SAPO-11 did not have the characteristic morphology as presented in the literature review in this thesis (Table 3-1). The sample consists of small crystals in the nano range and a minority of crystal aggregates in the micro range as seen in Figure 5-3.

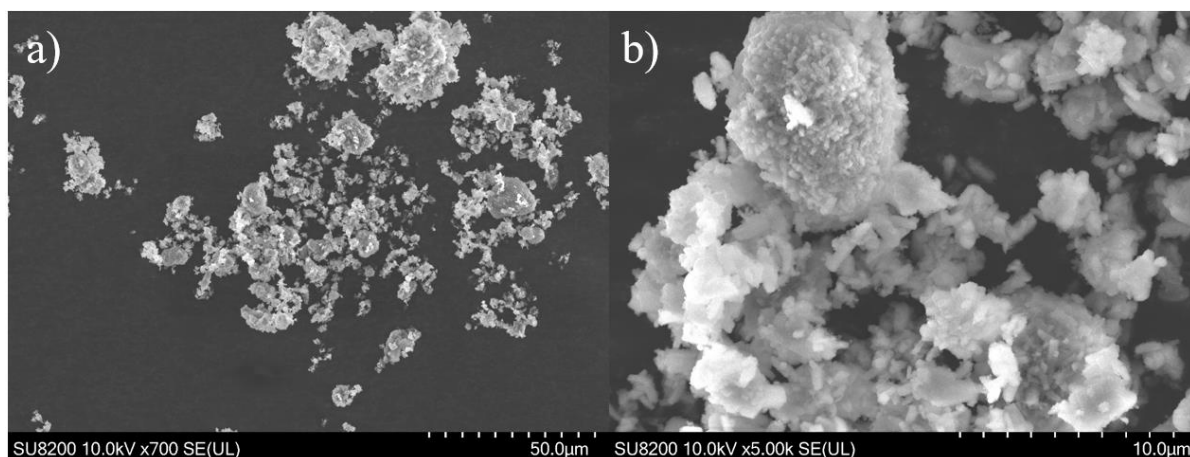


**Figure 5-3 SEM images of commercial SAPO-11 sample a) low magnification and b) at high magnification.**

All synthesized samples were spherical aggregates in the micrometer range. The effect of synthesis conditions as a function of temperature is investigated in Figure 5-4 - Figure 5-7. The static samples presented in Figure 5-4 and Figure 5-5, show an increase in regularity as the temperature increases. Samples at low temperature were significantly larger and contain more amorphous particles. For the samples synthesized under rotational conditions, the particle shape is highly irregular at lower temperatures. For both static and rotational heating, bottom one-third samples show to be more regular than top two-thirds at low temperatures. As the temperature increases, the difference is minimized.

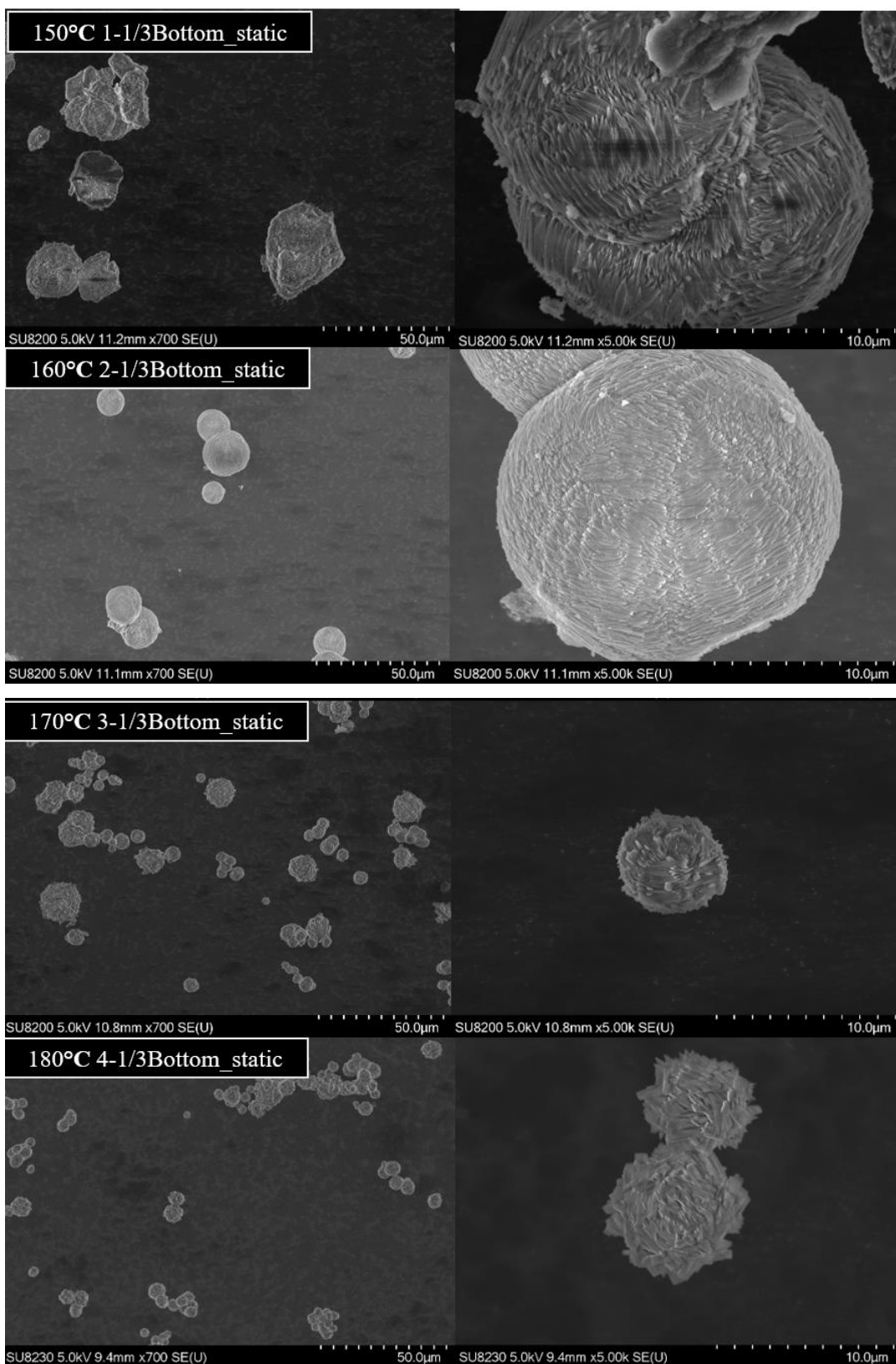


Figure 5-4 SAPO-11 synthesized from 1/3Bottom\_static

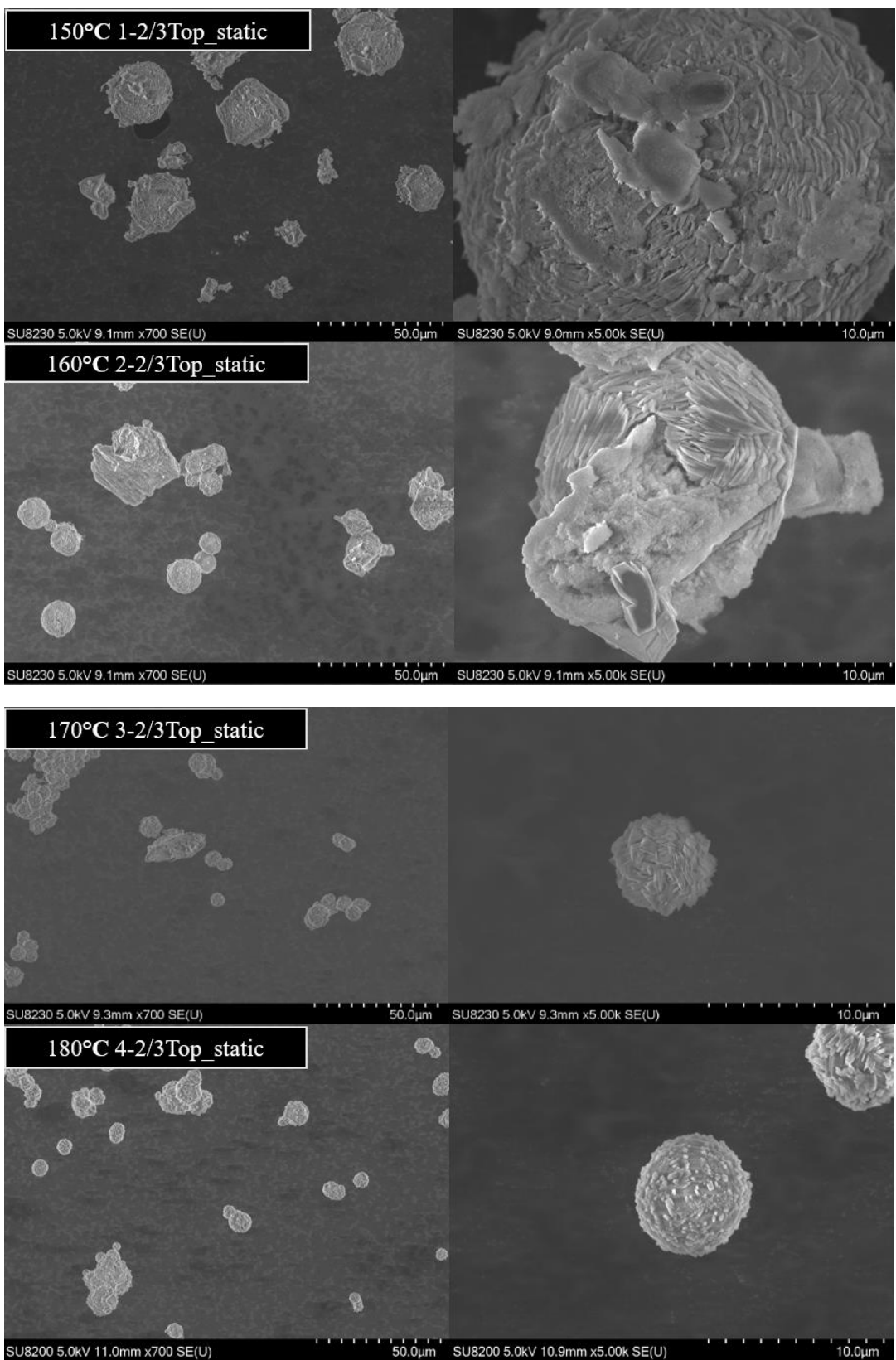


Figure 5-5 SAPO-11 synthesized from 2/3Top\_static.

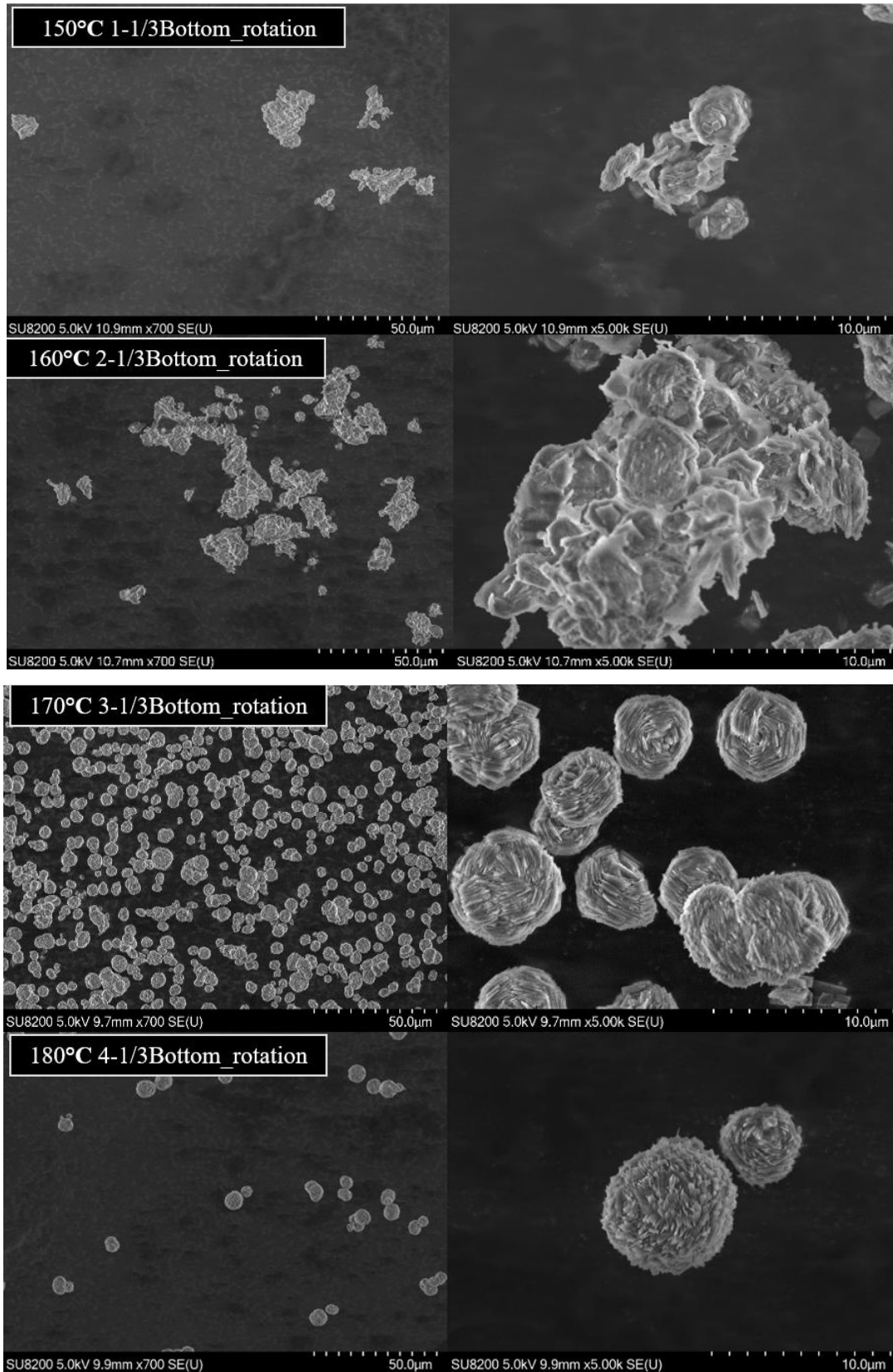


Figure 5-6 SAPO- 11 synthesized 1/3Bottom\_rotation.

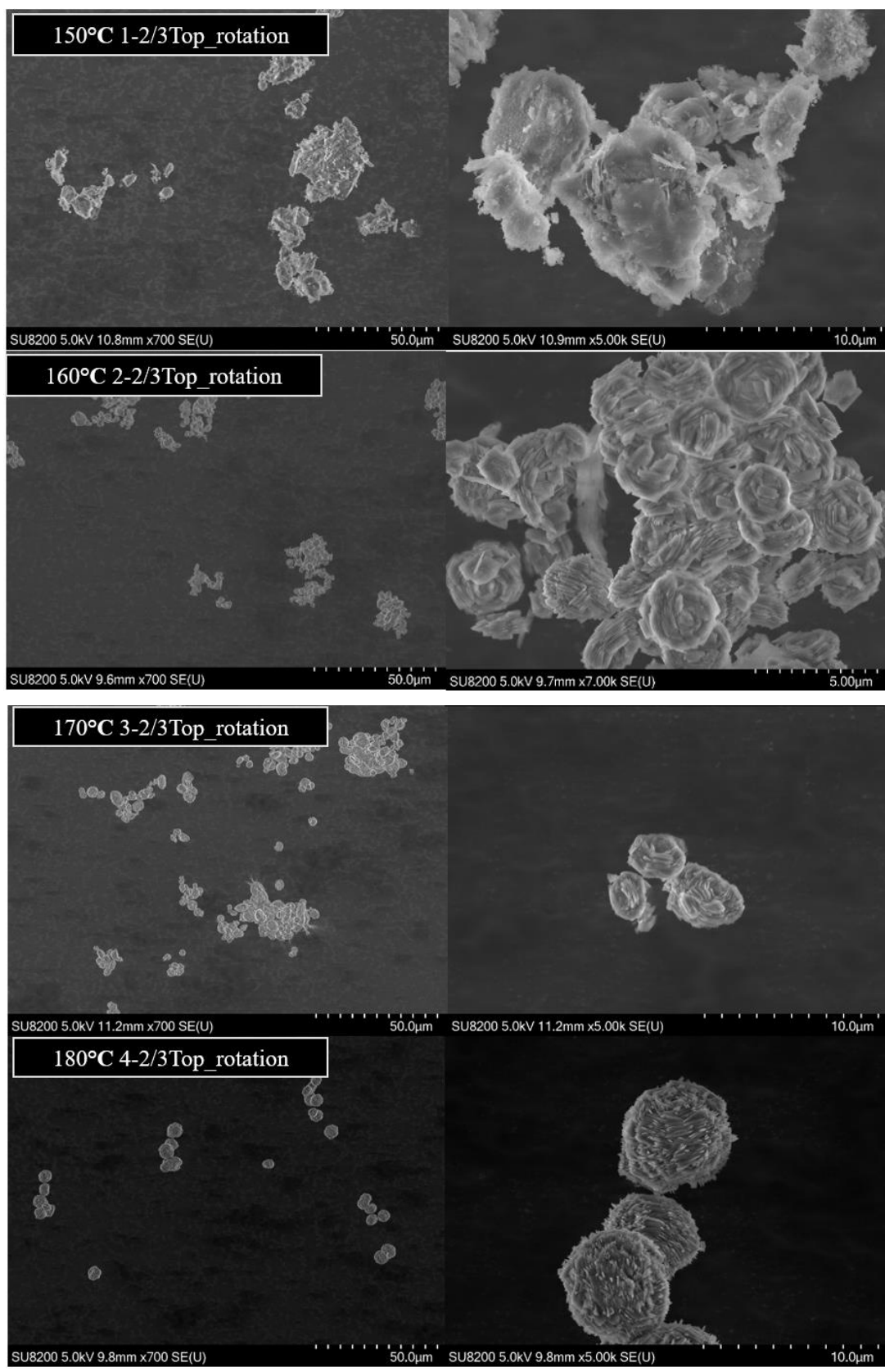


Figure 5-7 SAPO-11 synthesized from 2/3Top\_rotation

This screening provides us with knowledge regarding the particle size and regularity of the different approaches. All experiments 1- 4 provide spherical aggregates with the particle size from 20 – 5  $\mu\text{m}$ . From this imaging, one can suggest that experiment 4 carried out at 180 has the highest regularity and proves to produce the smallest SAPO-11 particles.

The trends for the SAPO-11 observed by scanning electron microscopy can be correlated to the findings obtained from x-ray diffraction. Static synthesis conditions gave clean diffractograms with increased intensity as a function of temperature (Figure 5-1). The SEM images show the particles are more regular and less amorphous as a function of temperature. As for rotational conditions, obtained images reveal low temperatures do not facilitate regular spherical aggregates. All samples provided by rotational conditions are smaller at low temperatures. Furthermore, SEM images revealed that the commercial sample consists of particles in the nano range. This finding can be linked to peak broadening in the collected diffractogram.

#### **HRSEM of SAPO-11**

HRSEM imaging of 4-1/3Bottom\_static from experiment 4 synthesized at 180 °C show that the SAPO-11 spherical aggregates consist of small squared crystals in the nanoscale range (Figure 5-8).

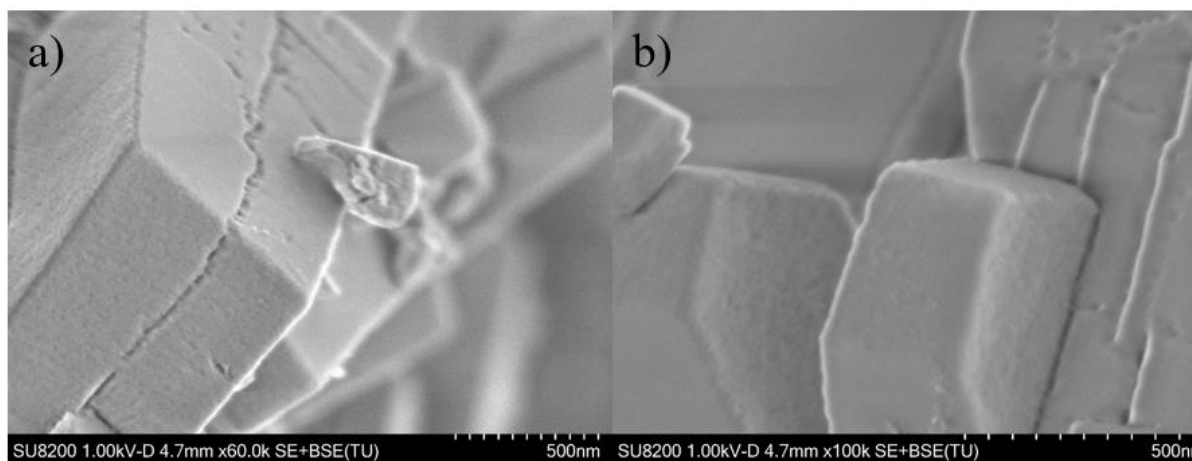


**Figure 5-8 SEM images of 4-1/3Bottom\_static, a) is magnified 60.0k and b) is magnified 100k.**



### 5.2.3 Size distribution

The diameter of the SAPO-11 aggregates was measured and presented in Figure 5-9. Samples crystallized at 150 and 160 °C with rotational heating were not possible to measure and are not presented. 20 particles are counted for each sample. As a control to verify that the amount is sufficient for its purpose and reproducible, 200 particles were calculated for sample 4-1/3Bottom\_static, see Appendix D for histograms and associated standard deviations. The particle size of the agglomerates decreases as a function of increasing temperature under static conditions from 20 to 5µm correlating to observations found by scanning electron microscopy. Under rotational conditions for 170 and 180 °C, the opposite can be visualized. The average particle size shows a small increase at higher temperatures. This value is however not clearly significant (Figure 5-9).

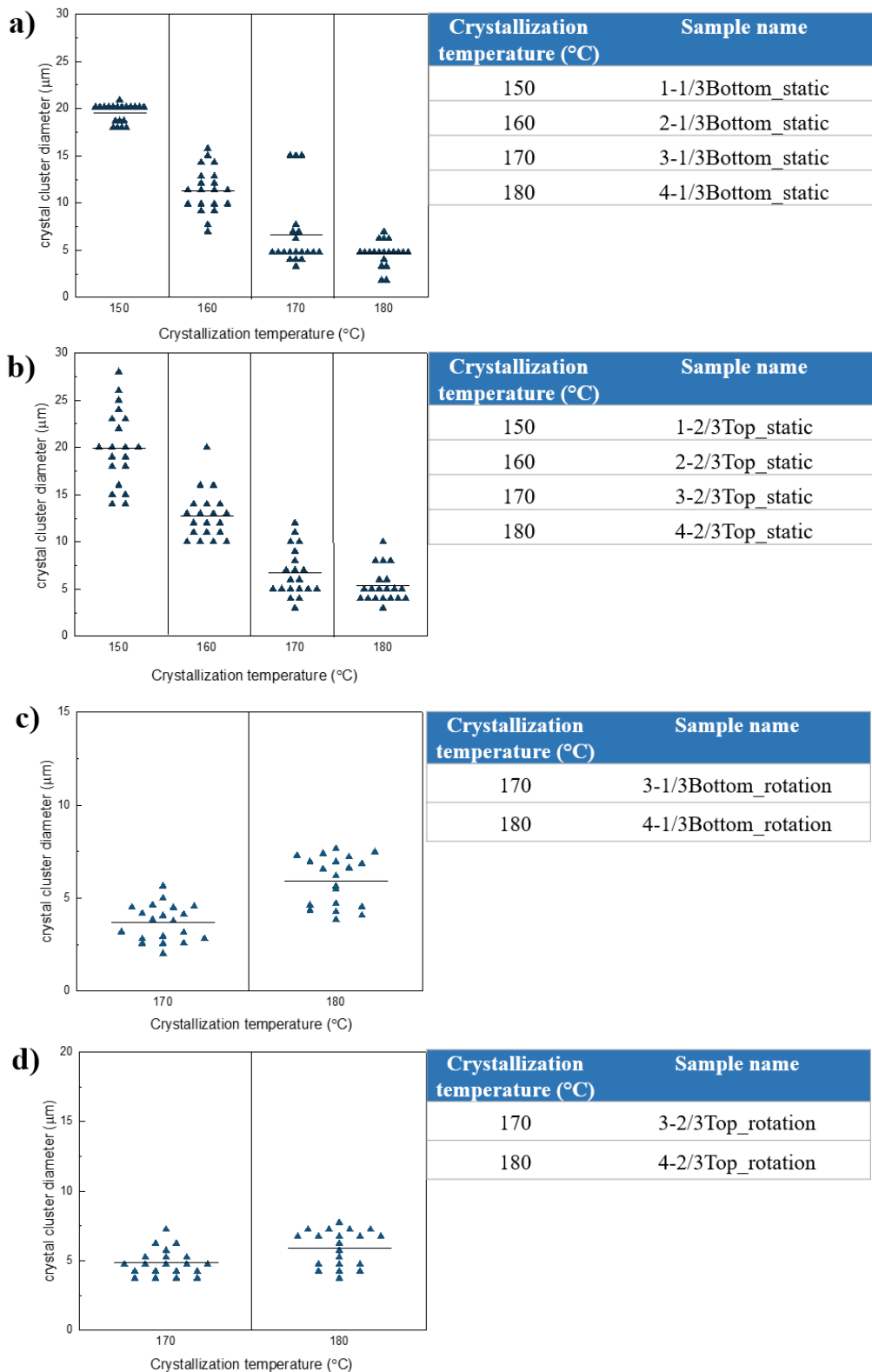


**Figure 5-9** Size distribution of the diameter of SAPO-11 aggregates as a function of crystallization temperature. Blue triangle indicates one single particle that is measured and the black horizontal line indicates the mean value. Figure a) and b) are particles synthesized statically, while c) and d) are from rotational synthesis.

## 5.2.4 Calcination

### Initial calcination route

To investigate the calcination procedure for template removal, the largest (12 $\mu$ m) SAPO-11 aggregates synthesized at 160 °C were initially investigated (Experiment 2). Sample 2-1/3Bottom\_static was attempted calcined at 550 °C in air and oxygen atmosphere. The sample became discolored, most severely after calcination in air indicating incomplete combustion and the presence of carbon (Figure 5-10). Samples crystallized at 160 °C did not prove to lead to the best SAPO-11 samples from investigations with SEM and XRD. Therefore, this sample was not chosen for further calcination experiments.

Sample	Atmosphere	T <sub>calcination</sub> (°C)	Color observation
2-1/3Bottom_static	O <sub>2</sub>	550	Minor discolored, cream
	Air	550	Major discolored, brown

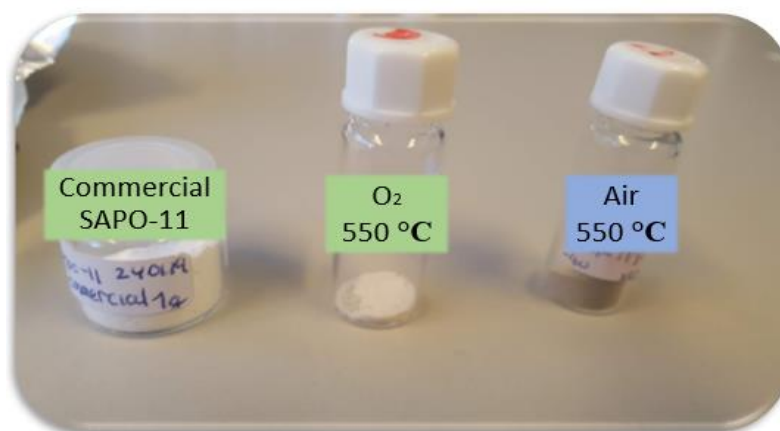


**Figure 5-10** Qualitative observations of selected samples for calcined SAPO-11 2-1/3Bottom\_static at 550°C after calcination in the atmosphere of oxygen and air. The latter is heavily discolored. This visualization includes commercial sample to the left as a color reference.

### Optimized calcination route

Smallest SAPO-11 aggregates (5 $\mu$ m) synthesized in experiment 4 at 180°C were calcined in four different routes to map out the best calcination pathway to assure a template free catalyst. Figure 5-11 shows qualitative observations for selected sample 4-1/3Bottom\_static after calcination. The samples calcined in air at T<sub>1</sub> (550°C) was discolored to a minor degree. Also,

sample calcined in air at  $T_2$  ( $600^\circ\text{C}$ ) was discolored. For the samples calcined under pure oxygen flow at  $600^\circ\text{C}$ , no discoloration was obtained.

Sample	Atmosphere	$T_{\text{calcination}} (^\circ\text{C})$	Color observation
4-1/3Bottom_static	Air	550	Minor discolored, cream
	Air	600	Minor discolored, cream
	$\text{O}_2$	550	Minor discolored, white
	$\text{O}_2$	600	Clear white

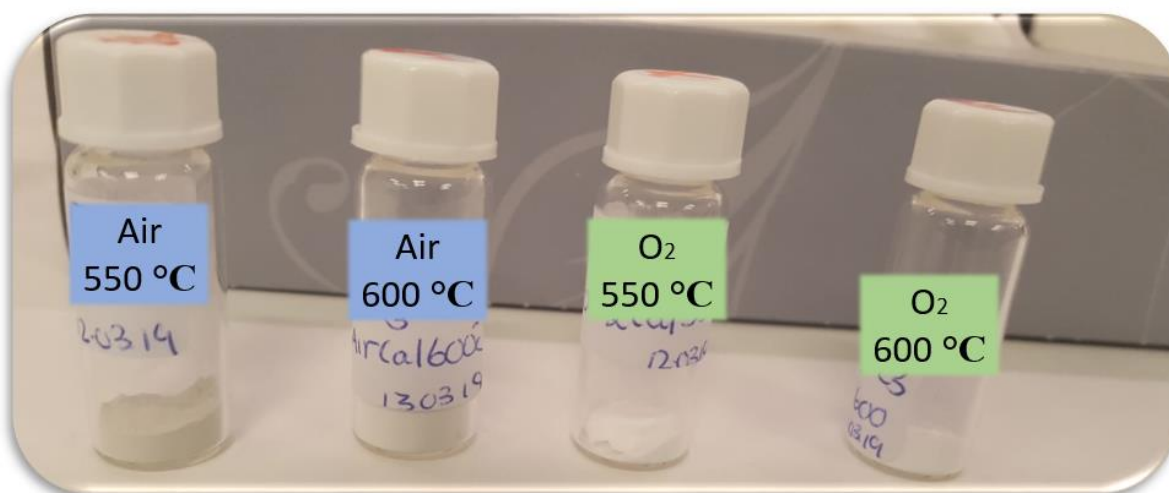


**Figure 5-11** Qualitative observations of selected samples for calcined SAPO-11 4-1/3Bottom\_static at  $T_1=550^\circ\text{C}$  and  $T_2 = 600^\circ\text{C}$  in air and oxygen atmosphere. Samples calcined in air are visibly discolored.

To investigate the impact of the different synthesis requirements, all four samples were investigated with PXRD and SEM. All samples showed comparable results. Therefore, Rietveld refinement is only shown for the selected sample SAPO-11 4-1/3 Bottom\_static (Figure 5-2) before calcination treatment a) and after b). These data collected before calcination were recorded on a full plate sample holder and are thus of high quality. After calcination the sample was measured on a glass plate covered with a polypropylene film, resulting in lower data quality. The glass plate sample holder was employed due to the limitations in the calcination procedure (Section 4.1.4). From the diffractograms (Figure 5-2), several considerations are made. XRD samples prepared on a glass plate sample holder are expected to show a broad peak at  $2\theta$  of  $22.5^\circ$ . This is attributed to the plastic film covering

the sample holder and is observed in diffractogram b). From the diffractograms, one can observe a peak at  $2\theta$  angle of 5 and 31. This can be linked to the presence of an impurity in the sample. The weighed profile R-factor ( $R_{WP}$ ) is lower in diffractogram a) vs b). The R factor, provides here an indication of how well the measured data is fitted to the calculated values. One can clearly see the quality of the fitting is poorer for the calcined sample which is reasonable with the presented considerations taken into account.

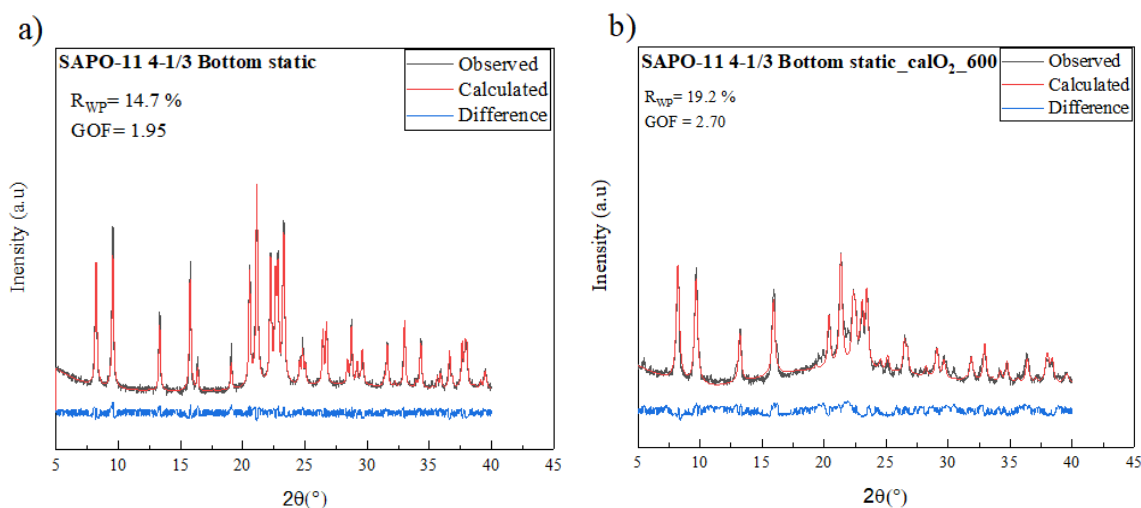
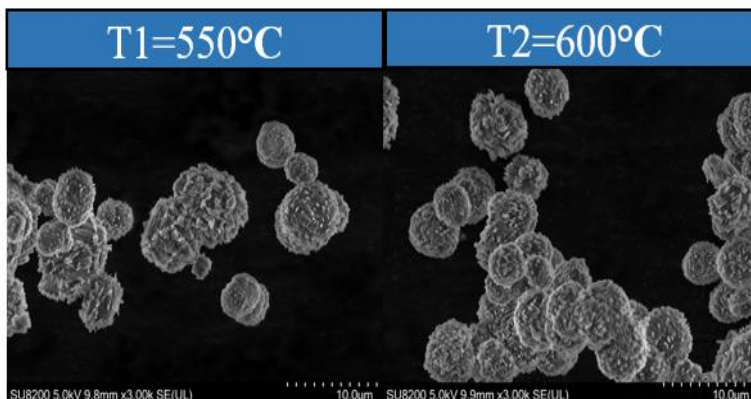
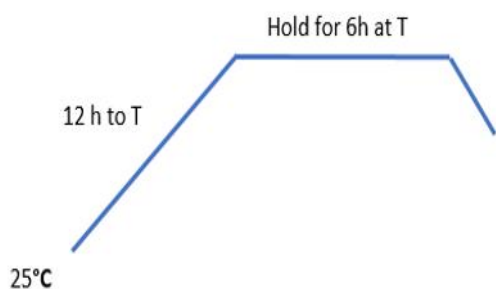


**Figure 5-12 Rietveld refinement for a) uncalcined SAPO-11 4-1/3 Bottom static, and b) calcined SAPO-11 4-1/3 Bottom static under oxygen flow at 600°C.**

All samples were investigated visually with SEM after calcination (Figure 5-13). We refer to Figure 5-4 for images of uncalcined samples. The samples persisted their morphology after treatment and maintained the spherical aggregates. However, samples calcined in air show some rupture of clusters. SAPO-11 samples calcined at 600°C under oxygen flow proves to give the clearest, best-maintained particles. The best calcination route was determined to be at temperature 600 °C under oxygen flow.

Atmosphere : Air



Atmosphere : Oxygen

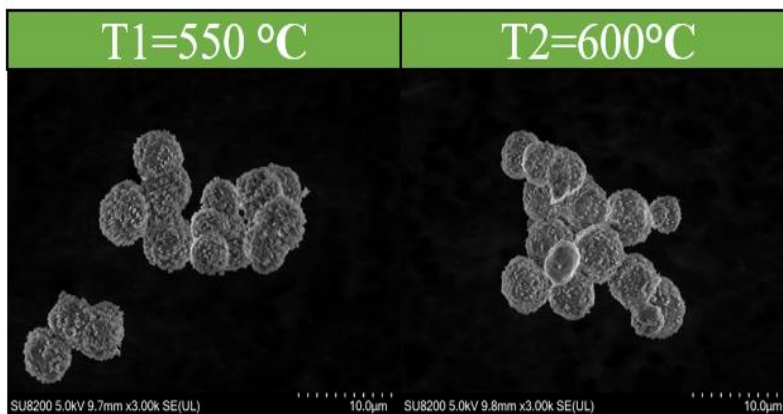
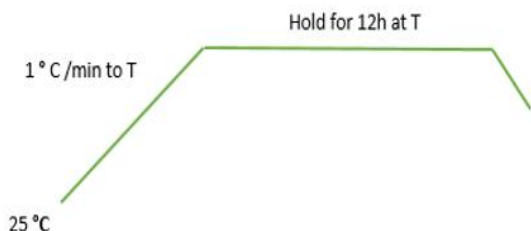


**Figure 5-13 SEM images after different calcination procedures for sample SAPO-11 4-1/3 Bottom\_static. Blue is in air atmosphere at T<sub>1</sub> and T<sub>2</sub>, and green is in oxygen atmosphere at same temperature.**

### 5.2.5 Thermogravimetric analysis

To investigate template removal quantitatively, TGA was performed on selected samples. The sample SAPO-11 4-1/3Bottom\_static from the optimized calcination route was measured before and after calcination. Figure 5-14 shows a) uncalcined and b) calcined sample at different calcination conditions. Template removal is visible in the regime from 200 - 600°C. The plateau seen in the uncalcined sample is non-existing after calcination procedures. This shows the template is removed for all conditions. There are indications of a small difference in the stability of the calcined samples as a function of temperature and atmosphere. Samples calcined at 600 °C in oxygen atmosphere appears to be most stable together with the sample treated in air at 550°C. From the scale of the y-axis ( Figure 5-14 b), one can observe the

difference is minor. For further investigation and to rule out operator errors or instruments drifts, the measurements requires several reproducibility tests. This was not performed.

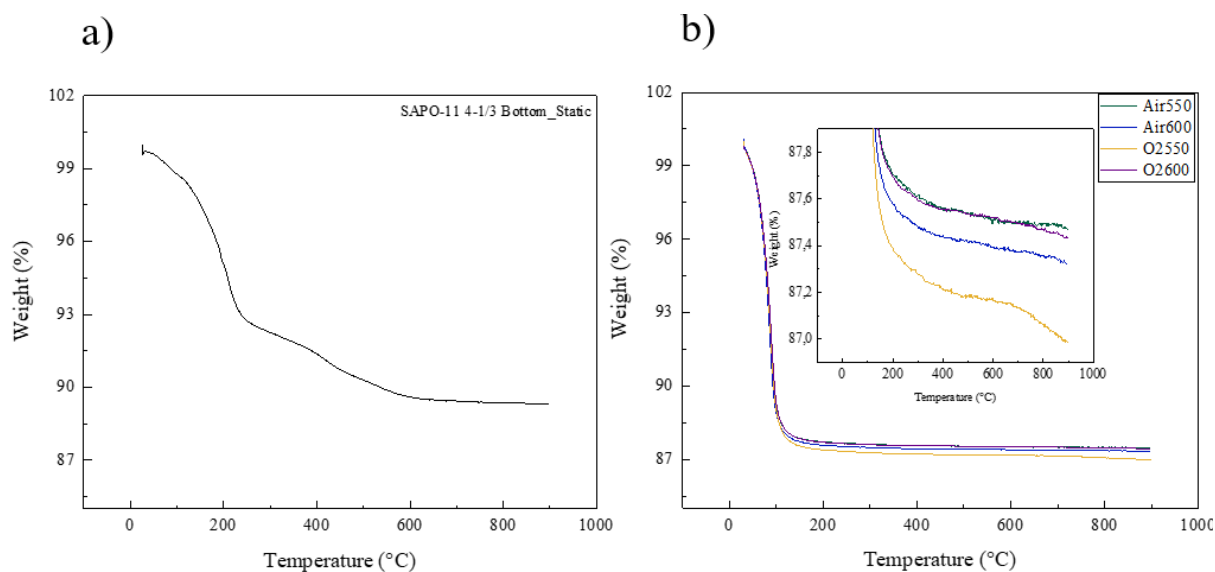


**Figure 5-14 TGA curves for sample SAPO-114-1/3Top\_static. Where a) is the unclaimed sample, and b) is the calcined sample under different conditions.**

## 5.3 Selective characterization for acidity and framework

### 5.3.1 N<sub>2</sub> - physisorption and surface area simulations

Selected samples from experiment 4, crystallized at 180 degrees were calcined with the optimized route under oxygen flow at 600 degrees. N<sub>2</sub> physisorption was performed on in-house SAPO-11 samples and the commercial sample (Table 5-2). The surface area was empirically calculated from measured isotherms by the BET and t-plot method. The commercial sample had a surface area of 90 m<sup>2</sup>/g (BET), while the four different samples from experiment 4 have a BET surface area of approximately 200 m<sup>2</sup>/g with calculations attained from both methods. The t-plot method gives an indication of the pore size, revealing all samples contain both micro and mesoporous character, where mesoporosity seems to be dominating. The mesoporosity was also calculated with the DH-method for validation and is in agreement with results from the t-plot. Isotherms in Figure 5-15 show features from isotherm 1 at low pressures, isotherm type IV at higher pressures (69). The hysteresis is

characteristic of mesoporous materials, where adsorption and desorption do not overlap. This indicates the presence of different pore sizes that fill differently. The voids between the aggregates must also be taken into consideration and gives supposedly a contribution. Simulations obtained by Monte Carlo give an solvent accessible solvent surface area calculated to be 260 m<sup>2</sup>/g and isotherm simulations give 200 m<sup>2</sup>/g as presented in Table 5-3. Connolly surface area is not chosen to be a suitable method as previously stated and discussed in the work of Düren et al (64).

**Table 5-2 Surface area (m<sup>2</sup>/g) and pore volume (cm<sup>3</sup>/g) for SAPO-11 samples.**

Sample	Surface area (m <sup>2</sup> /g)				Pore Volume (cm <sup>3</sup> /g)			
	BET <sup>a</sup>	t-plot <sup>b</sup>	External <sup>b</sup>	Pore <sup>b</sup>	Total <sup>c</sup>	Micropore <sup>b</sup>	Mesopore	Mesopore <sup>d</sup>
SAPO-11 Commercial	90	97	53	44	0,177	0.017	0,160	0,150
SAPO-11 4-1/3Bottom_static	167	190	37	153	0,148	0.052	0,096	0,091
SAPO-11 4-2/3Top_static	202	246	40	206	0,171	0,066	0,105	0,105
SAPO-11 4-1/3Bottom_rotation	209	245	39	206	0,168	0,068	0,100	0,100
SAPO-11 4-2/3Top_rotation	204	202	29	172	0,146	0,075	0,071	0,080

<sup>a</sup> BET method

<sup>b</sup> t-plot method

<sup>c</sup> Volume absorbed method p/p<sub>0</sub> = 0,99

<sup>d</sup> DH method



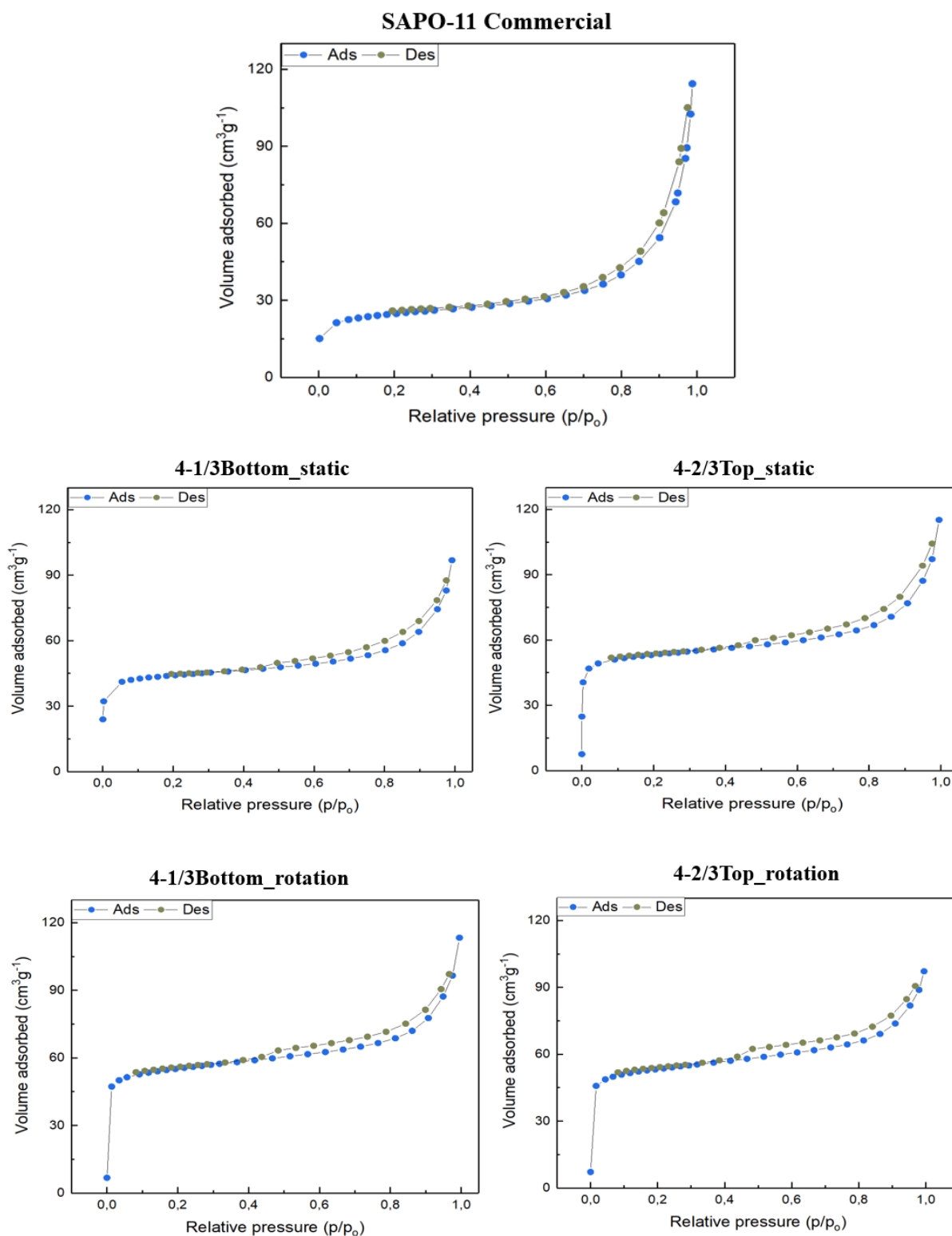


Figure 5-15 shows the adsorption/desorption isotherms for the commercial SAPO-11 and the four synthesized samples at 180 °C.

**Table 5-3 simulated Monte Carlo surface area**

Surface area (m <sup>2</sup> /g)		
Conolly	Accessible Solvent	Sorption simulation
1107	260	200

### 5.3.2 Elemental analysis with MP-AES and EDS

Elemental analysis was performed for all samples from experiment 4 (crystallized at 180 °C) and for the commercial sample. The fraction of T atoms are given in moles normalized to Al (Table 5-4). All four synthesized samples inhibit a similar element composition. It indicates that gel separation and heating conditions do not have a significant effect on the synthesis. Furthermore, it is observed that the Si content for the synthesized samples is 40% of the gel composition. It indicates that not all Si has been incorporated into the structure. A comparison between the commercial sample and synthesized samples, reveals the commercial sample has a ten times higher silicon content. A high silicon content facilitates Si substitution into the framework and is linked to the activity of the material (1). As a control, to verify the results from the analysis, both methods MP-AES and EDS have been applied and show to be in good agreement with each other (Table 5-4).

**Table 5-4 Elemental analysis of as-synthesized samples and supplied SAPO-11 presented as (S<sub>x</sub>Al<sub>y</sub>P<sub>z</sub>)O<sub>2</sub>.**

Sample	Method	Si	Al	P	Al+P / Si
<b>SAPO11-Commercial</b>	Supplier	0,250	1,0	0,50	3,00
	EDS	0,447	1,0	0,96	3,14
	MP - AES	0,390	1,0	0,88	3,26
<b>SAPO-11-4 1/3Bottom_Static</b>	Gel	0,100	1,0	1,00	11,0
	EDS	0,040	1,0	0,98	25,6
	MP - AES	0,040	1,0	1,02	26,5
<b>SAPO-11-4 2/3Top_Static</b>	Gel	0,100	1,0	1,00	11,0
	EDS	0,043	1,0	1,07	25,7
	MP - AES	0,039	1,0	1,03	27,6
<b>SAPO-11-4 1/3Bottom_Rotation</b>	Gel	0,100	1,0	1,00	11,0
	EDS	0,042	1,0	1,02	25,6
	MP - AES	0,045	1,0	1,31	30,3
<b>SAPO-11-4 2/3Top_Rotation</b>	Gel	0,100	1,0	1,00	11,0
	EDS	0,042	1,0	1,02	25,2
	MP - AES	0,035	1,0	1,01	29,7

### 5.3.3 CO probing with FT-IR

FT-IR was performed on two selected samples, supplied SAPO-11 (Figure 5-16) and synthesized SAPO-11 (Figure 5-17) from synthesis experiment 4. (Static conditions, 180°C) Their Brønsted acidity was investigated prior to catalytic testing. OH-region of the supplied SAPO-11 (Figure 5-16) shows characteristic Si-OH, P-OH and Si(OH)Al stretching modes with low-intensity peaks (70). Species detected in the OH-region were compared to an appropriate and more extensively studied SAPO material, SAPO-34 (Table 5-5).

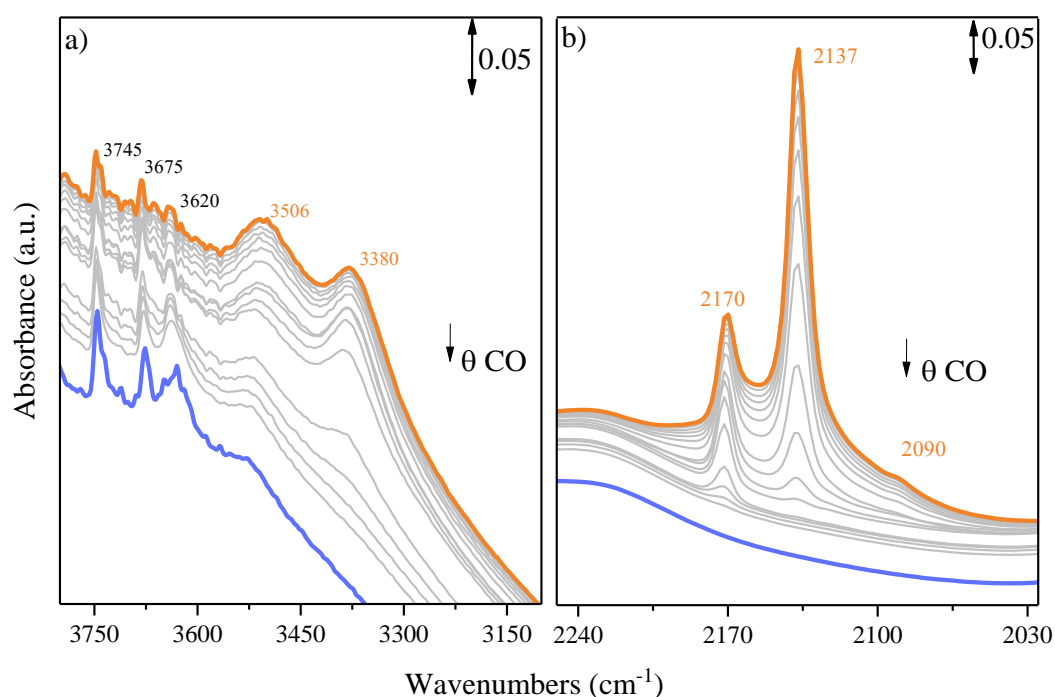


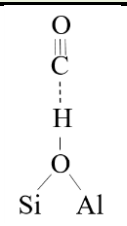
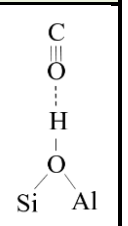
**Figure 5-16** IR spectra of decreasing CO dosages at 100K on SAPO-11 commercial. a) OH stretching region and b) CO-region. Blue line indicates collected spectra for the activated sample at 400 °C. Orange line indicates maximum CO dosage.

**Table 5-5 Overview of bands found in this study and their assignment based on similar zeotype presented in literature.**

SAPO-11 (cm <sup>-1</sup> ) Measured	Previous characterized SAPO SAPO-34(cm <sup>-1</sup> ) from (70)	Assignment
3745	3748	Si-OH
3675	3676	P-OH
3620		Si(OH)Al

The P-OH and Brønsted site bands are visible shifted in the spectra indicating the perturbing of basic CO. The intensity of the Si-OH band is clearly decreased at maximum dosage. However, no shift for the Silanol group is present. The CO region show 3 peaks. An evident blue shift of the CO stretching mode from 2143 cm<sup>-1</sup> (stretching of the free molecule ) to 2170 is ascribed to strong polarization of the CO molecule when interacting with Brønsted OH groups (OH-C≡O stretching) (Table 5-6). The peak at 2137 cm<sup>-1</sup> corresponds to liquidlike CO (70). Furthermore, a weak signal can be observed at 2090 cm<sup>-1</sup>. This is likely attributed to CO-interaction through oxygen and correspond to OH-O≡C stretching (71).

Table 5-6 shows assigned peaks to Figure 5-16 for the subscript a) OH stretching region and subscript b) CO-region. Subscript a indicates peaks in spectra a showing the OH-region, and subscript b indicates spectra b showing the CO-region.

<sup>a</sup> Si-OH (cm <sup>-1</sup> )	<sup>a</sup> P-OH (cm <sup>-1</sup> )			<sup>a</sup> Si(OH)Al (cm <sup>-1</sup> )			<sup>b</sup> CO (cm <sup>-1</sup> )		
vOH	vOH	vOH <sub>COst</sub>	ΔvOH	vOH	vOH <sub>COst</sub>	ΔvOH	vCO Si(OH)Al		
3745	3675	3506	-171	3620	3380	-240	2170	2137	2090

FT-IR for the synthesized sample (Figure 5-17) shows a higher signal to noise ratio. The high level of scattering can be described by the larger aggregates size compared to the particle size in supplied SAPO-11. The overall intensity of the spectra is critically reduced. The silanol group is not visible in spectra. However, we observe the band of the P-OH group clearly. From Figure 5-17b) it is evident that CO is perturbed from the Brønsted sites in the material, even though the corresponding OH mode was not clearly visible in the OH stretching region.

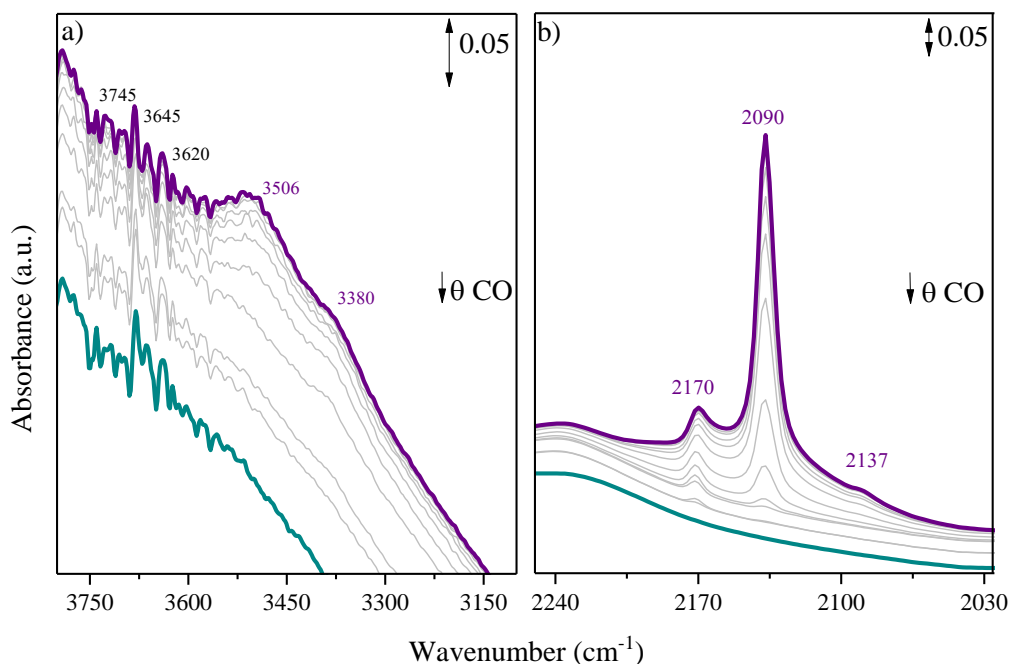


**Figure 5-17** IR spectra of decreasing CO dosages at 100K on SAPO-11 4-1/3Bottom\_Static a) OH stretching region and b) CO-region. Blue line indicates collected spectra for the activated sample at 400 °C. Orange line indicates maximum CO dosage.

To correlate the results obtained by FT-IR to the elemental analysis performed, the commercial sample had a significantly higher silicon content than the synthesized samples (Table 5-4). This corresponds well with not observing a clear visible Si-OH band for the synthesized samples.

## 5.4 Performance tests

### 5.4.1 Activity

Activity tests were performed on samples from experiment 4 crystallized at 180 °C as well as the supplied sample (Figure 5-18). The commercial catalyst has a 67 % conversion at 5 min TOS before gradually deactivating as a function of time on stream. The four synthesized samples inhibit a similar conversion reactivity compared to the commercial sample. Initial conversion is at 40 % for samples synthesized in static conditions, and 30 % for samples synthesized under rotational conditions. Reactivity of the synthesized samples overlap as a function of time. The stability of the commercial sample is significantly higher compared to

synthesized samples. Methanol conversion of the commercial sample reaches 30 % conversion after 1000 min TOS. The synthesized samples are fully deactivated after 500 min TOS.

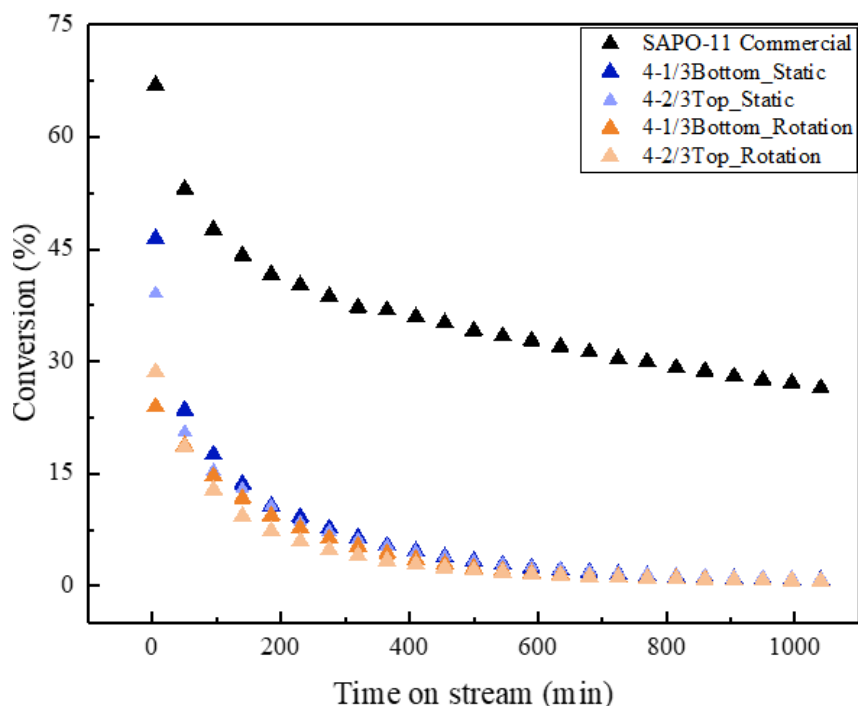


Figure 5-18 Conversions vs Time on Stream

### 5.4.2 Selectivities

Testing of the catalysts showed all samples are most selective to  $C_{5+}$  hydrocarbons. The highest methanol conversion achieved over the commercial sample is approximately 60% towards hydrocarbons after 45 min TOS (Figure 5-19). The selectivity to light olefins  $C_2-C_4$  (green, blue and yellow line) is between 2-15 %, decreasing after 50 min TOS. Overall selectivity towards hydrocarbons is stable as a function of time on stream.

The synthesized samples show similar trends in selectivity towards hydrocarbons. The highest methanol conversion over the synthesized samples is measured to be 45 % after 45 min. The selectivity towards the light olefins is significantly higher than the commercial sample. Selectivity towards  $C_2$  is  $< 7.5$  % for the commercial sample, and  $7.5 < 15$  % for synthesized samples.  $C_3$  selectivities are similar for both commercial and synthesized samples, while the  $C_4$  selectivities are higher for the synthesized samples. There is not a significant difference in the stability of the samples synthesized under different conditions. The small variations in

selectivity percentage observed may be related to operator or instrument sources of error, and will therefore not be discussed further.

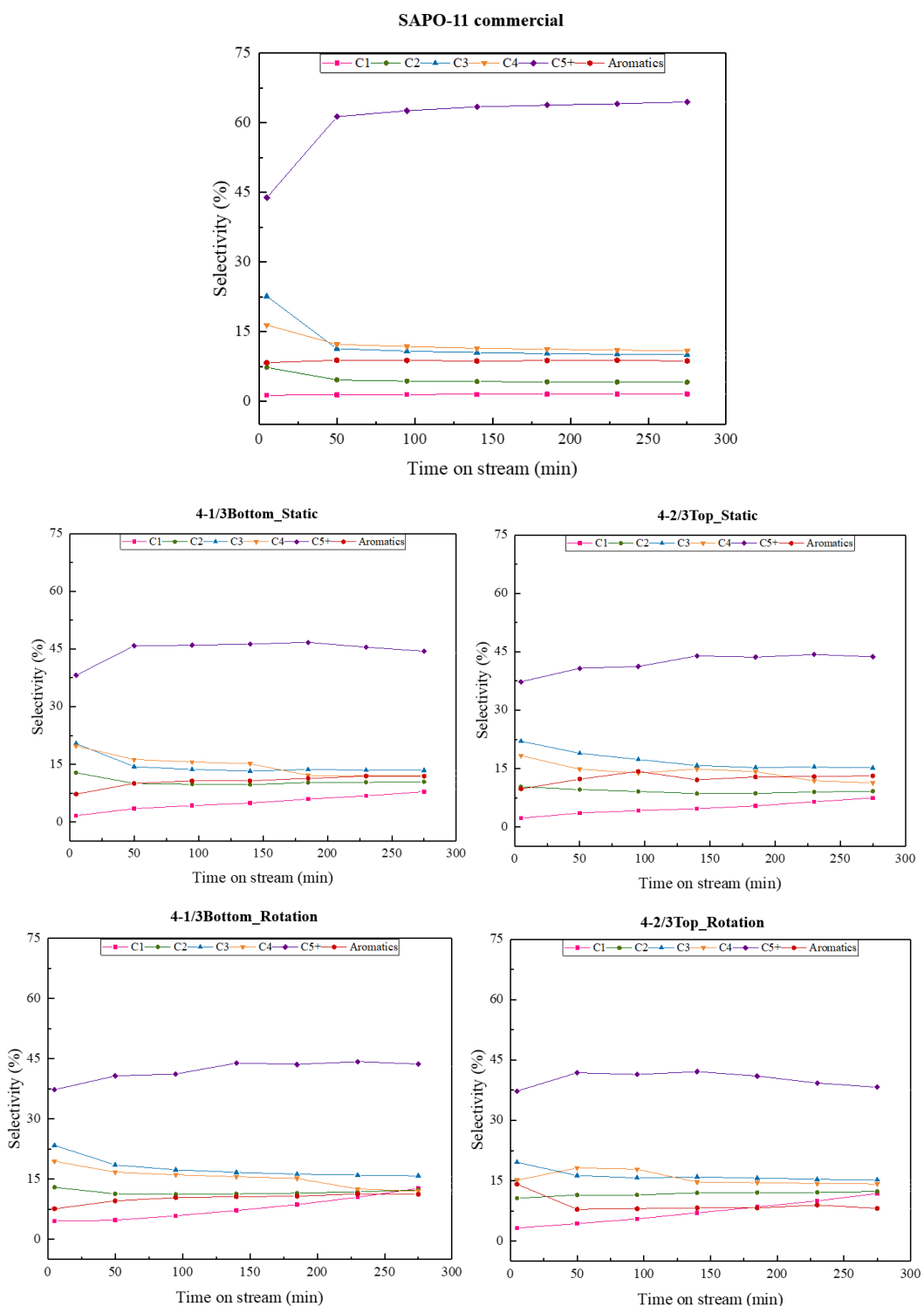


Figure 5-19 Selectivity as function of time on stream for selected synthesized samples and commercial SAPO-11.

## 6 Discussion

The aim of this thesis was to investigate the synthesis route of conventional SAPO-11 to explore the potential of SAPO-11 for the methanol to olefins reaction. As this catalyst was briefly studied in literature and not previously synthesized or tested in the catalysis group, a commercial sample was in addition supplied for catalyst comparison. This section will discuss three different topics.

- i) Screening of the synthesis route for SAPO-11
- ii) Acidity and framework aspects of the SAPO-11 materials
- iii) Performance tests for the MTO reaction

### 6.1 Screening of the synthesis route for SAPO-11

The initial method attempted for the synthesis of SAPO-11 carried out at 150 °C under static conditions was unsuccessful and provided amorphous products. The rapid reactant mixing during synthesis inhibited the development of a homogeneous synthesis mixture that was visually observed where the bottom part formed a denser layer. A low crystallization temperature gives rise to slow kinetics of the molecules, resulting in an overall slow reaction. The visual observations supported the methodology presented (gel separation of top and bottom) at 150 °C of Lok et al. Experiments in the initial method showed that crystallization of bottom part of synthesis mixture produced more crystalline SAPO-11 aggregates. This finding initiated the exploration of the synthesis approach where the gel mixture is separated into top and bottom part.

Tuning of the reaction conditions during the modified CHT method revealed the impact of

- i) Temperature
- ii) Top and bottom separation of the synthesis mixture
- iii) Static or rotational crystallization



## Temperature

Temperature had the greatest influence on the synthesis. Low temperatures (150 and 160 °C), did not facilitate a homogeneous SAPO-11. The SAPO-11 aggregates were in the range of 20-15 µm and amorphous phases were identified. (Figure 5-4-Figure 5-7) An increase in temperature facilitated the formation of smaller, regular SAPO-11 aggregates, where the smallest (5 µm) aggregates were formed at 180 °C under both static and rotational conditions. The effect of the temperature is strongly related to the nucleation and growth rate in the material. Cejka et al. (33) reported that an increase in temperature facilitates larger crystals due to the increased growth rate. However, it is the aggregate size and not crystal size that is reported in this thesis.

The findings revealed the reported crystallization temperature 150 °C from Lok et al (51), was not preferable for the synthesis of SAPO-11. Low (150 °C) and high (195°C) crystallization temperatures are reported in the work of Lopez et al (42), where the low temperature SAPO-11 obtained was spherical and significantly amorphous after 6 h crystallization. The SAPO-11 crystallized for 4 h at 195°C exhibited considerably smaller SAPO-11 spherical aggregates with higher crystallinity, where particles were irregularly shaped. The study varies both the crystallization time and temperature simultaneously inhibiting a clear systematic trend of the separated effects. Nevertheless, it shows a similar trend to the observed results where the aggregates size decreases as a function of temperature.

Liu et al. reported regular spherical SAPO-11 synthesized at 180 °C for 48 h (38), while Wu et al. obtained partly regular spherical aggregates at 185 °C crystallized at 48 h (37). Studies based on higher crystallization temperature resulting in spherical SAPO-11 aggregates, were conducted by Bing et al. at 200 °C resulting in irregular particle size (39). Similarly, a study from 2018 by Liu et al. crystallized at 200°C showed irregular SAPO-11. A crystallization temperature set to 200 °C was found to be unfavorable also when conducted with an unconventional hydrothermal method (18, 35).

Based on empirical results and the literature analysis presented, a temperature trend can be proposed, in which low temperature facilitate spherical SAPO-11 with amorphous phases, intermediate temperature favors crystalline, regular and spherical SAPO-11, while high temperature give crystalline but irregular SAPO-11. Other morphologies than spherical aggregates are only reported at crystallization temperatures above 190 °C (25, 45, 46) (Table

3-1).

Systematic studies on the synthesis of SAPO-11 at controlled temperature ranges as presented in this thesis are so far not well defined in literature. However, it is evident to say that the separated studies presented at distinct temperatures support the argument of 180 °C being the preferable temperature to obtain both regular, highly crystalline and spherical SAPO-11 aggregates.

### **Top and bottom separation of the synthesis mixture**

SEM and PXRD revealed that separating the synthesis mixture in the top and bottom had an impact on the crystallinity at low crystallization temperatures (150 and 160 °C). At low temperatures, the top part of the synthesis mixture resulted in more regular particles (SEM) and crystallinity (PXRD). At higher temperatures, the difference was diminished. The patent of Lok et al. (51) describes a synthesis procedure at 150 °C, and not higher temperature ranges. The separation of top and bottom of the synthesis mixtures is not investigated in other literature found.

### **Static or rotational crystallization**

At low temperature (150 and 160 °C), the highest crystallinity was obtained for samples prepared through static crystallization. There was not a significant effect of the crystallization method at high temperatures. Both static and rotational crystallization resulted in similar crystallinity (Figure 5-1), morphology (Figure 5-4-Figure 5-7), particle size (Figure 5-9). There are no previous studies found on the effect of static or rotational crystallization for the synthesis of SAPO-11.

It is clear from this screening that the preferable synthesis conditions are obtained during static conditions, at 180 °C from the bottom part of the synthesis mixture corresponding to experiment 4, and sample 4-1/3Bottom\_static. Compared to the secondary study of earlier published work on the synthesis of SAPO-11 (Table 3-1), this synthesis route has a crystallization time at 133h which is higher than times presented in literature (24-48h) (25, 37).

Calcination proved to be challenging for the SAPO-11 materials. It became evident that pore blocking occurred for the SAPOs synthesized at 160 °C due to severe discoloration from white to brown (Figure 5-10). Calcination was successfully performed for samples synthesized at 180 °C (Experiment 4). Shifting the atmosphere from air to pure oxygen and increasing the temperature from 550 to 600 °C proved to be sufficient for complete combustion and template removal. A study on unidirectional 10-ring H-ZSM-22 by Tekedel et al. reported a two-step calcination route where the samples were first calcined in static air, followed by calcination in pure oxygen (72). This study supports the challenges observed in our study and shows the requirement of pure oxygen atmosphere for template removal.

## **6.2 Acidity and framework aspects of the SAPO-11 materials**

FT-IR with CO dosing revealed that the as-synthesized sample had a higher signal to noise ratio compared to the commercial sample. This is likely to occur from scattering due to particle size as previously stated (Section 5.3.3). Spectra of both activated samples were compared for peak identification. Figure 6-1 verifies the presence of species in the OH-region for both samples, where  $\nu$ P-OH and  $\nu$ Si-OH-Al bands are well defined, but  $\nu$ Si-OH is not present for the as-synthesized sample.

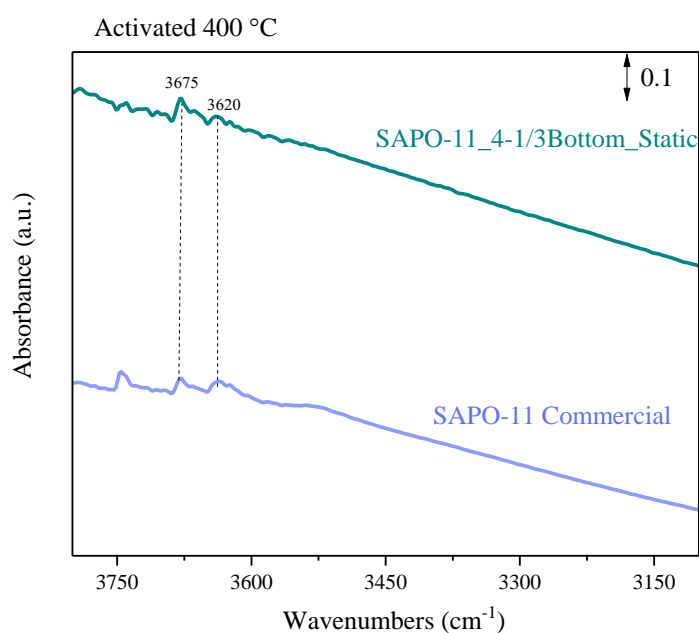


**Figure 6-1** IR spectra of activated samples at 400°C under vacuum for SAPO-11 commercial and as-synthesized sample SAPO-11\_41/3Bottom\_Static. The dotted line indicates the peak positions.

The CO-shifts observed for the commercial and synthesized samples occur at equivalent wavenumber intervals. The equivalent shifts imply both samples inhibit similar acidity for each acid site (Figure 5-16).

However, it was clearly observed from the spectra in Figure 5-16 that the intensity of the CO shift related to the Brønsted sites was significantly higher for the commercial sample. The high peak intensity is here attributed to a higher acid site density suggested by elemental analysis (Table 5-4). Si content (0,45mole fraction) in the commercial sample is higher than for the synthesized samples by a factor of ten. The low Brønsted acidity observed for the synthesized sample can be correlated to the low amount of Si content in the sample (0,04 mole fraction). A low Si content results in less Si being substituted into the framework, which limits the number of Brønsted sites being formed.

The overall acidity strength can be compared to i) zeolites and ii) zeotypes. Upon interaction with CO, the Brønsted acidic bands shift to lower frequencies. The observed redshift is directly proportional to the acidic strength (Table 6-1) (70). For corresponding blue shifts of CO, the readers are referred to the references in Table 6-1. CO-FTIR studies for SAPO-11 were not found covered in the literature. Therefore, other zeolites and SAPOs are presented

for comparison and acid strength identification. A study from Bordiga et al. (70) revealed zeolite H-SSZ-13 exhibits a stronger acid density than equivalent framework type (CHA) SAPO-34. The studies reported both materials showed a high and low-frequency Brønsted band related to their structural properties. However, this could not be distinguished in the observed redshift. Westgård et al. reported moderate acid sites for the 12-ring in SAPO-5 (73). The difference in acidity relies on the complexity of zeolite features, and is up to date not fully understood.

**Table 6-1 Previous work on CO FT-IR for zeolites and zeotypes. The table shows reported redshifts obtained by different references for the acidity identification of measured SAPO-11. The acidity scale is determined by literature and visualized in the color red to blue, where red is strong and blue is mild.**

Reference	Material	Framework type and dimensionality	Si(OH)Al (cm <sup>-1</sup> )			Acidity
			$\nu$ OH	$\nu$ OH <sub>COst</sub>	$\Delta\nu$ OH	
Bordiga et al. (70)	H-SSZ13	CHA 3	3616 <sup>HF</sup> 3584 <sup>LF</sup>	3300	-316	Strong
Otero et al. (62)	ZSM-5	MFI 3	3614	3312	-302	Strong
Bordiga et al. (70)	SAPO-34	CHA 3	3627 <sup>HF</sup> 3603 <sup>LF</sup>	3357	-270	Moderate
Westgård et al. (73)	SAPO-5	AFI 1	3626	3358	-268	Moderate
<b>Measured</b>	<b>SAPO-11</b>	<b>AEL 1</b>	<b>3620</b>	<b>3380</b>	<b>-240</b>	<b>Mild</b>

HF = High-frequency band (70)

LF = Low-frequency band (70)

The acidity of the 10-ring SAPO-11 is determined with CO FT-IR. Compared to related materials reported in the literature, SAPO-11 samples exhibit a moderate to mild acidity. This study highlights the structural complexity of zeolitic materials, which are revealed in the band frequencies observed for different zeolitic materials. Furthermore, the results obtained support and confirm that the number of Brønsted acid sites in the commercial SAPO-11 is significantly higher than for the as-synthesized samples. The acidity and framework aspects elaborated in this separated study will further be discussed related to i) catalytic performance

of SAPO-11 with different number of acid sites. ii) SAPO-11 as a potential catalyst for the MTO reaction.

### 6.3 Performance tests for the MTO reaction

Performance tests for commercial and synthesized SAPO-11 (Section 5.4.1) revealed there was a significant difference in the activity for the commercial SAPO-11 (0.45 mole fraction Si) and synthesized samples (0.04 mole fraction Si) from experiment 4 (synthesized at 180 °C). This trend is observed for SAPO-18 reported by Zhu et al. (1), where high Si content increases the activity and decreases the deactivation of the catalyst. This correlates well with the results obtained, in which the commercial catalyst had significantly higher activity. An opposite trend was reported for SAPO-34. The finding was attributed to the rate of coke formation which increases with higher Brønsted acid density. Zhu et al. proposed that SAPO-34 deactivate more rapidly at higher Si content due to the overall higher Brønsted acidity in the material. An in-depth explanation was however not presented.

Furthermore, our results show that there was no significant difference in catalytic activity for the synthesized samples. This is in agreement with the elemental analysis presented in Table 5-4, which reported minor differences in T-atoms content. Therefore, the synthesized SAPO-11 samples are expected to have a similar number of active sites. There are few studies covering the behavior of SAPO-11 for the methanol to olefins reaction. Literature found suffers the disadvantage of variable reaction conditions and parameter representation. To discuss the behavior of SAPO-11 related to previous work, a selection of studies are presented at the same reaction temperature, 400 °C (Table 6-2). Presented studies operate at different space velocities (WHSV), which has a direct effect on the contact time and catalyst lifetime. In general, it is expected that high space velocities result in shorter lifetime due to shorter contact time with the catalyst. Space velocity ( $h^{-1}$ ) is expressed as the mass of methanol feed per hour divided by the mass of catalyst and is for clarity presented in Equation (6-1).

$$WHSV(h^{-1}) = \frac{\text{mass of MeOH per hour}}{\text{mass of the catalyst}} \quad (6-1)$$

Wang et al. reports obtaining 65 % hydrocarbon conversion after 5 min TOS at 3  $h^{-1}$  WHSV. The catalyst is slowly deactivated and reaches 40 % after 200 min (Table 6-2). Compared to commercial and synthesized samples presented in this work at 0.5  $h^{-1}$  WHSV, Wang et al.

provide a more active catalyst. The finding reveals SAPO-11 in their study performs better despite the increase in space velocity. The surface area presented in the work is in the same range as samples provided in our study. However, the catalyst composition reveals a surprisingly low value of Si content in their study. The effect of the silicon content is not in agreement with the expected behavior of a material with estimated low Brønsted acidity. To understand the behavior of the reported SAPO-11 catalyst to a greater extent, the synthesis procedure applied should be further investigated. The study of Campelo et al. report an overall low conversion rate towards low hydrocarbons, where DME is highly favored at all TOS (Table 6-2).

**Table 6-2 A presentation of the major differences in means of surface area (m<sup>2</sup>/g), composition and conversion at selected TOS for different SAPO-11 and previously reported parameters. TOS is given at two different times indicated by t.**

Reference	Catalyst	Composition (Si <sub>x</sub> Al <sub>y</sub> P <sub>z</sub> )O <sub>2</sub>	S <sub>BET</sub> (m <sup>2</sup> /g)	t <sub>reaction</sub> (°C)	WHSE (h <sup>-1</sup> )	Conversion (%) at TOS (min)	
Author	SAPO-11 Commercial	Si <sub>0.45</sub> Al <sub>1.0</sub> P <sub>0.96</sub> *	90	400	0.5	t=5	t=200
						67	40
Author	SAPO11 4- 1/3Bottom_Static	Si <sub>0.04</sub> Al <sub>1.0</sub> P <sub>0.98</sub> *	167	400	0.5	t=5	t=200
						46	10
Wang et al. (26)	SAPO-11	Si <sub>0.014</sub> Al <sub>0.5</sub> P <sub>0.48</sub> **	191	400	3	t=5	t=200
						64	50
Zhu et al. (1)	SAPO-11	Si <sub>0.028</sub> Al <sub>0.493</sub> P <sub>0.479</sub>	-	400	1.25	t=	t=
						-	-
Campelo et al. (74)	SAPO-11	Si <sub>0.03</sub> Al <sub>0.52</sub> P <sub>0.45</sub>	110	400	0,06	t=0	t=600
						72***	28****
						2.88*****	0.17*****

\* Determined from EDS analysis. Presented in Table 5-4

\*\* Calculated from the Brønsted acid density (mmol/g) in the reference (26).

\*\*\* DME is included in the methanol conversion calculation reported in reference (74).

\*\*\*\*Methanol conversion given subtracted DME (wt. %) for comparative purposes.

In terms of selectivity, the performance of commercial and synthesized SAPO-11 can be discussed. The hydrocarbon selectivity, reveals the in-house synthesized samples inhibit a higher selectivity towards the low hydrocarbons and a lower selectivity towards C<sub>5+</sub> (Figure 5-19) compared to the commercial sample. It can be speculated that the results are correlated

to the aggregates size. The commercial SAPO-11 is in the nanometer range, and the synthesized SAPO-11 aggregates are in the micrometer range. Small aggregates will have a shorter diffusion path, in which larger molecules can diffuse out. A larger aggregate size facilitates a longer diffusion path. Therefore, it is expected that the diffusion of the larger hydrocarbons chains will decrease. Hence, it is expected that low hydrocarbons will escape easier due to their shorter chain length. Overall the synthesized catalysts deactivate faster but provide a higher selectivity towards desired products (C<sub>2</sub>-C<sub>4</sub>).

To correspond best possible to existing literature, hydrocarbon selectivity will further on be given for C<sub>5+</sub>, C<sub>4</sub>, Propene and ethene. In an attempt to overcome the data limitation for the MTO reaction over SAPO-11 and to provide an extended discussion where other literature is included, selected data from literature has been replotted for comparative purposes. The reader is referred to the references in Figure 6-2 for their original representation. Figure 6-2 shows the selectivity of the commercial sample at highest methanol conversion (67 %) as well as highest methanol conversion obtained for the synthesized samples (46 %). The selectivity towards light olefins is shown to be highest for the synthesized sample at 46 % methanol conversion. In the study from Wang et al. they found the selectivity favors C<sub>5+</sub> within the range of 40-70% methanol conversion, which is in line with the results obtained in this work. Zhu et al. report similar trends for ethene, propene and C<sub>4</sub>. Greatest selectivity obtained is for propene and C<sub>4</sub>. The value of C<sub>5+</sub> is however not reported. Despite the variance in reaction conditions, both studies correlate well to the results found for the SAPOs investigated in this thesis, providing a measure of expected performance for the material. The work from Campelo et al. is not in agreement with our studies or other literature discussed. Reported values include DME as a product of the reaction. When DME is viewed as a hydrocarbon product, the calculated methanol conversion increases (Equation(4-1)) and selectivity decreases (Equation (4-2)). Therefore, this study is not directly comparable with our studies.



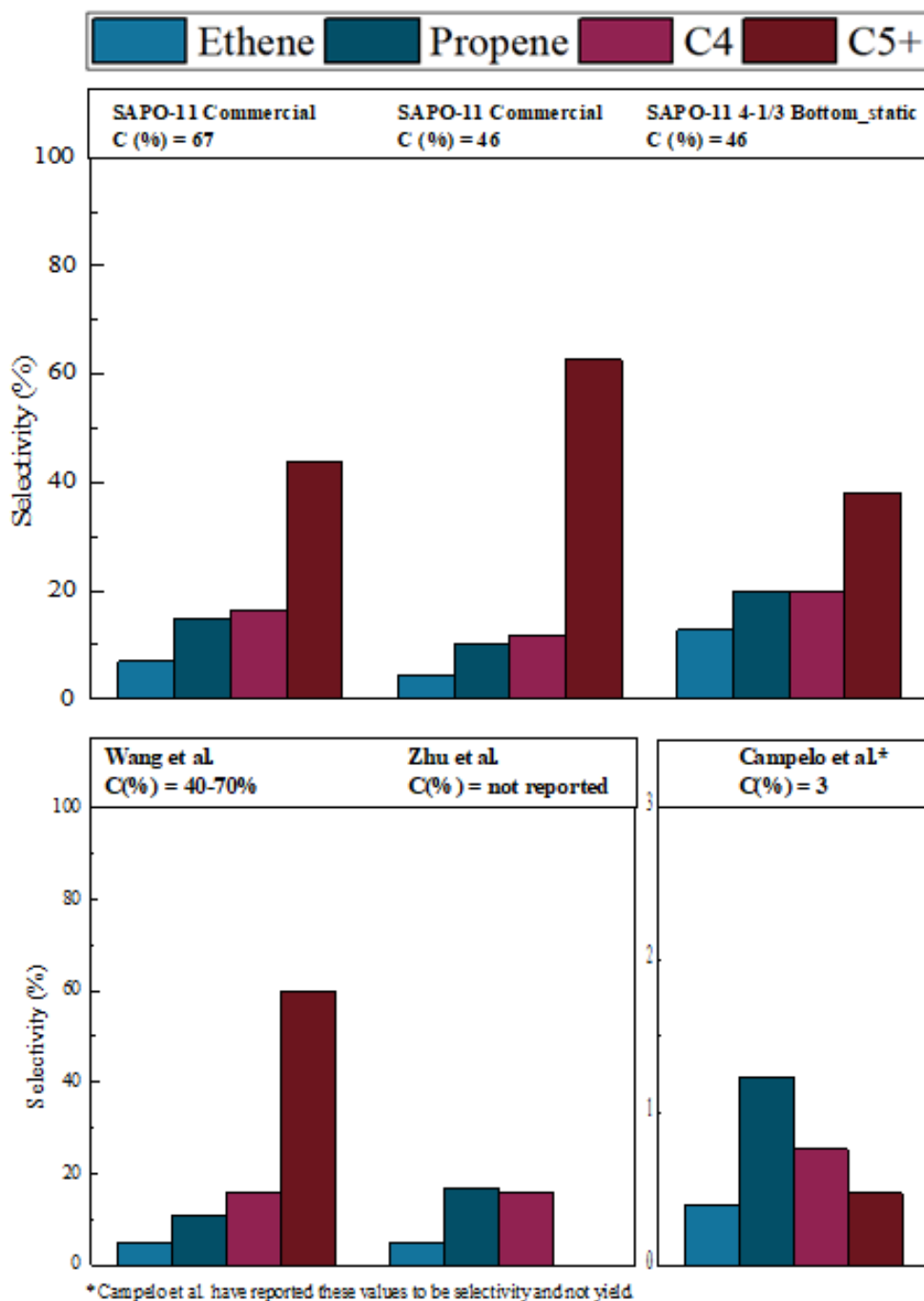
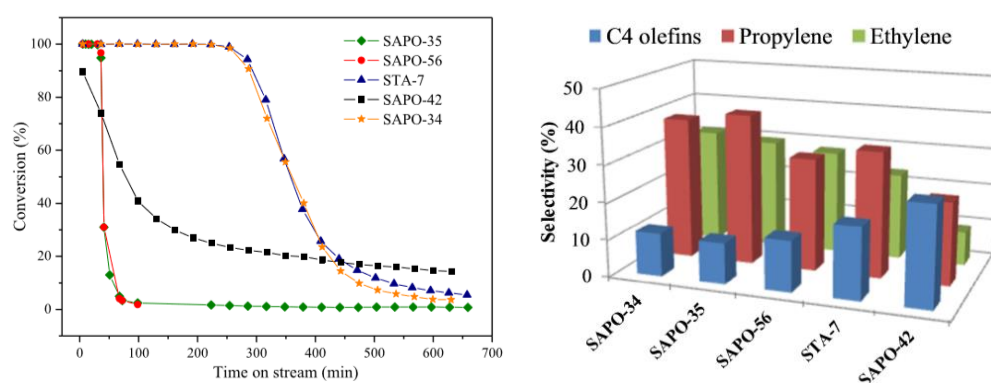


Figure 6-2 Above: The selectivity for Commercial SAPO-11 and synthesized SAPO-11 4-1/3 Bottom\_static. The commercial sample is shown at highest methanol conversion (67%) as well as for the highest methanol conversion obtained for the synthesized sample (46 %). Below: The selectivity found in the literature of Wang et al (26), Zhu et al. where C<sub>5+</sub> selectivity is not included (1) and Campelo et al. (74) Here the y-axis (selectivity, %) has a different scale, and only goes to 3 %. The results are most likely yields and not selectivity.

The provided analysis of the product distributions seen for SAPO-11 reveals significant differences in the selectivity towards light olefins. The synthesized samples in this work show the highest selectivity towards light olefins. This finding has been correlated to Si content in the catalysts as well as the aggregate size show to be the key parameter for the performance for the unidirectional material. To further investigate the performance of SAPO-11 and quantify the activity of the active sites, it could be appropriate to study the turnover frequencies and compare them with literature. Due to the limitations of existing literature, this was not performed.

To finalize the discussion of SAPO-11 as a catalyst for the MTO reaction, we will discuss the performance of the catalyst compared to other zeolitic materials studied. Pinilla-Herrero et al. (66) studied in 2017 five different catalysts under comparable experimental conditions  $t=400^{\circ}\text{C}$  and WHSE  $0.35\text{h}^{-1}$  (Figure 6-3). The experiments were performed in the catalysis group of the University of Oslo. From the study provided by Pinilla-Herrero et al., it is evident to say SAPO-11 does not reach full methanol conversion compared to other tested SAPOs. However, the lifetime of the catalyst is significantly higher than SAPO-56 and SAPO-35. In terms of both conversion and selectivity, SAPO-11 resembles the behavior of SAPO-42. The activity of SAPO-11 provides a lower methanol conversion, but a comparable lifetime. The selectivity of the light olefins in SAPO-11 behave in an increasing order where  $\text{C}_4 > \text{C}_3 > \text{C}_2$  similar to the trend obtained for SAPO-42. To identify the differences and correlate to structural aspects of the nature of the materials, further control studies are needed.



**Figure 6-3 Left: Conversion vs TOS (min). Right: Selectivity obtained at full methanol conversion over SAPO-35, SAPO-56, STA-7, SAPO-42 and SAPO-34 under the same experimental conditions  $t=400^{\circ}\text{C}$  and WHSE  $0.35\text{h}^{-1}$ . Taken from (66).**

## 7 Conclusion

A systematic study on the synthesis of zeotype SAPO-11 has been carried out with multiple techniques. Screening selected at temperatures and crystallization conditions revealed high crystallinity SAPO-11 can be synthesized at 180 °C under static conditions. High crystallization temperatures facilitated the formation of uniform SAPO-11 aggregates with 5µm average aggregate size, while low crystallization temperatures favored the existence of amorphous and asymmetric spherical aggregates. The screening showed there is an effect of gel separation as previously reported by Lok et al in 1982. The separation of synthesis mixture to two-thirds of the top layer and one-thirds of the bottom layer showed one-thirds bottom resulted in more crystalline particles at low temperatures. The variance was diminished at higher crystallization temperatures stabilizing the dominant zeotype phase. The overall synthesis yield was relatively high and in the range of 65-85 % and presents a different approach for the synthesis of SAPO-11 with low silicon content and high surface area. Pore blocking in the unidirectional medium-pore materials was evident during the calcination process for 15 µm aggregates and the materials were unsuccessfully calcined in both air and oxygen atmosphere. Complete combustion and template removal were successfully accomplished for synthesized samples crystallized at 180 °C (5 µm) in the atmosphere of oxygen flow. This study highlights the challenges related to the calcination procedure in unidirectional zeotypes. Efficiency is limited by the amount of sample introduced 200-400mg/24h to the setup. Therefore, the procedure requires further study to increase the overall calcination efficiency.

Furthermore, a comparative study of synthesized and supplied SAPO-11, indicated the difference in acidity and particle size for the catalysts had a critical impact on their catalytic behavior in the methanol to olefins reaction. The materials were characterized for structural and acidity aspects with N<sub>2</sub>-physisorption, MP-AES, EDS and FT-IR. Performance tests for the catalysts showed supplied SAPO-11 catalyst had a significantly higher lifetime than the synthesized samples. The behavior was directly correlated to acid site density where the silicone content was determined to be 10 times higher in the commercial catalyst compared to synthesized samples. The commercial catalyst provided a higher selectivity towards C<sub>5+</sub> hydrocarbons, whereas the synthesized catalyst was more selective to light olefins (C<sub>2</sub>-C<sub>4</sub> hydrocarbons). From this study it clear that SAPO-11 suffers the disadvantage of overall low conversion (< 50 %) as a function of time on stream, and is not sufficiently selective towards

the desired product. However the study shows, it is possible to tune the selectivity towards desired product formation in terms of modifying the acid sites or particle size. In a larger scope, further research is needed to locate a SAPO-11 catalyst that has the potential for industrial application for i) methanol to olefins, and in prospect ii) CO<sub>2</sub> to olefins.

## 8 Perspectives

The study provided in this project motivates in principle three independent studies that can be combined to form a valuable study on SAPO-11. The lack of extensive studies on the behavior of SAPO-11 for methanol to olefins reaction gives rise to the following suggestions;

- i) Extending the screening of SAPO-11 at the conditions determined by this work to cover different Si/Al ratios with identical synthesis procedures.
- ii) Incorporating metal into the framework of SAPO-11, creating a Bi-metallic catalyst. The metal content should be varied at constant Si/Al ratios as a controlled study.
- iii) Testing the catalytic activity of a range of selected synthesized samples in terms of activity and selectivity for CO<sub>2</sub> conversion.

Performing the presented screening will identify optimal Si/Al of conventional SAPO-11 for the MTO reaction. Furthermore, incorporating a metal at different concentrations will show optimal conditions of metal loading that can be further applied for the CO<sub>2</sub> to olefins reactions, where methanol is the intermediate in the reaction.

# Appendix

## Appendix A - Molar ratios calculation

Molar ratios were recalculated to validate the recipe before choosing the synthesis approach. Presented here are calculations from example 18 (Table A-2, Table A-3) and example 15 (Table A-4, Table A-5) from patent US4, 440,871 (51). Both recipes prepare a synthesis mixture that is separated into two different fractions of synthesis gel (given in percentages). The template is only added to one of the separated fractions. The part of the synthesis mixture that has the template added, is further used. Due to error considerations, the ratios are calculated for the whole mixture without template and when the mixture is separated with template addition.

**Table A- 1 List of chemicals applied in the synthesis methods.**

Chemicals	Chemical formula
Phosphoric acid (85%)	H <sub>3</sub> PO <sub>4</sub>
Aluminum isopropoxide	Al(OC <sub>3</sub> H <sub>7</sub> ) <sub>3</sub>
95% fumed silica	SiO <sub>2</sub>
Dipropylamine (DPA)	C <sub>6</sub> H <sub>15</sub> N

Formulas applied:

$$n = \frac{m}{Mm} \quad (\text{A-1})$$

Where n is number of moles, m is the mass and Mm is the molar mass.

**Table A- 2 Molar calculations for example 18 - the entire mixture. The table shows the reactants, masses and molar masses and selected ratios. The real masses indicate the total mass after subtraction or addition of water.**

Reactants	Mass(g)	Molar mass(g/mole)	100% reactant	Real mass	moles	Ratio	Oxide ratio
<b>H<sub>3</sub>PO<sub>4</sub> 85%</b>	57,8	98,0	<b>H<sub>3</sub>PO<sub>4</sub></b>	49,1	0,50	Si/Al 0,30	0,6
<b>H<sub>2</sub>O</b>	33,5	18,0	<b>H<sub>2</sub>O</b>	63,2		Al/P 1,0	1,0
<b>Al(OC<sub>3</sub>H<sub>7</sub>)<sub>3</sub></b>	102,1	204,3	<b>Al(OC<sub>3</sub>H<sub>7</sub>)<sub>3</sub></b>	102,1	0,50	H <sub>2</sub> O /Al 7,0	14,1
<b>SiO<sub>2</sub> 30%</b>	30,1	60,1	<b>SiO<sub>2</sub></b>	9,0	0,15		
SUM	223,5						
<b>SDS</b>							
<b>DPA</b>	6,7	101,2					

It is stated that DPA is added to 65.7 g of mixture. This equals 29.4 % of the total mixture. If this is taken into consideration. Reactants mass is only 29.4% of total synthesis mixture.

**Table A- 3 Molar ratios for 29.4 % of the total mixture as stated in example 18.**

100% reactant	29,4% of real mass (g)	moles	Ratio	Oxide Ratio
<b>H<sub>3</sub>PO<sub>4</sub></b>	14,4	0,147	Si/Al 0,30	0,6
<b>H<sub>2</sub>O</b>	18,6	1,033	Al/P 1,00	1,0
<b>Al(OC<sub>3</sub>H<sub>7</sub>)<sub>3</sub></b>	30,0	0,147	H <sub>2</sub> O/Al 7,03	14,1
<b>SiO<sub>2</sub></b>	2,7	0,044		
<b>SDS</b>				
<b>DPA</b>	6,7	0,07	DPA/Al 0,45	0,9

Molar ratios given in example 18: **0.9 Pr<sub>2</sub>NH: 0.6 SiO<sub>2</sub>: Al<sub>2</sub>O<sub>3</sub>: P<sub>2</sub>O<sub>5</sub>: 57H<sub>2</sub>O**. The H<sub>2</sub>O/Al is incorrect. Therefore, example 15 was chosen and recalculated as seen in Table A-4.

**Table A- 4 Molar calculations for example 15 - the entire mixture. The table shows the reactants, masses and molar masses and selected ratios. The real masses indicate the total mass after subtraction or addition of water.**

Reactants	Mass(g)	Molar mass(g/mole)	100% reactant	Real mass	moles	Ratios	Oxide ratio	
<b>H<sub>3</sub>PO<sub>4</sub></b>								
85%	51,3	98	<b>H<sub>3</sub>PO<sub>4</sub></b>	43,6	0,4	Si/Al	0,05	0,1
<b>H<sub>2</sub>O</b>	160	18	<b>H<sub>2</sub>O</b>	167,8	9,3	Al/P	0,1	1,0
<b>Al(OC<sub>3</sub>H<sub>7</sub>)<sub>3</sub></b>	90,7	204,3	<b>Al(OC<sub>3</sub>H<sub>7</sub>)<sub>3</sub></b>	90,7	0,4	H <sub>2</sub> O/Al	20,1	42,0
<b>SiO<sub>2</sub> 95%</b>	1,4	60,1	<b>SiO<sub>2</sub></b>	1,3	0,02			
<b>SDS</b>								
<b>DPA</b>	7,4	101,2						

Recipe states template is only added to 1/3 of the mixture. Calculations are presented in Table A-5.

**Table A-5 Molar ratios for 1/3 of the total mixture as stated in example 15.**

100%reactant	1/3 mass (g)	moles	Ratio	Oxide ratio	
<b>H<sub>3</sub>PO<sub>4</sub></b>	14,5	0,15	Si/Al	0,05	0,10
<b>H<sub>2</sub>O</b>	55,9	3,1	Al/P	1,00	1,00
<b>Al(OC<sub>3</sub>H<sub>7</sub>)<sub>3</sub></b>	30,2	0,15	H <sub>2</sub> O/Al	21,0	42,0
<b>SiO<sub>2</sub></b>	0,44	0,0074			
<b>SDS</b>					
<b>DPA</b>	7,4	0,073	DPA/Al	0,5	1,0

Molar ratios in example 15: **1.0Pr<sub>2</sub>NH:0.1SiO<sub>2</sub>:Al<sub>2</sub>O<sub>3</sub>:P<sub>2</sub>O<sub>5</sub>:42H<sub>2</sub>O**, this corresponds well to what is presented in the published work. It is evident to say this is correct.

## Appendix B – Initial synthesis of SAPO – 11

The initial attempts of the synthesis of SAPO -11 were not successful. 16 crystallization processes were attempted. The samples were characterized by PXRD and SEM. PXRD indicates the material is not crystalline. No diffraction pattern is visible as seen in Figure B- 1. SEM imaging shows indication of an irregular amorphous material as seen in Figure B- 2



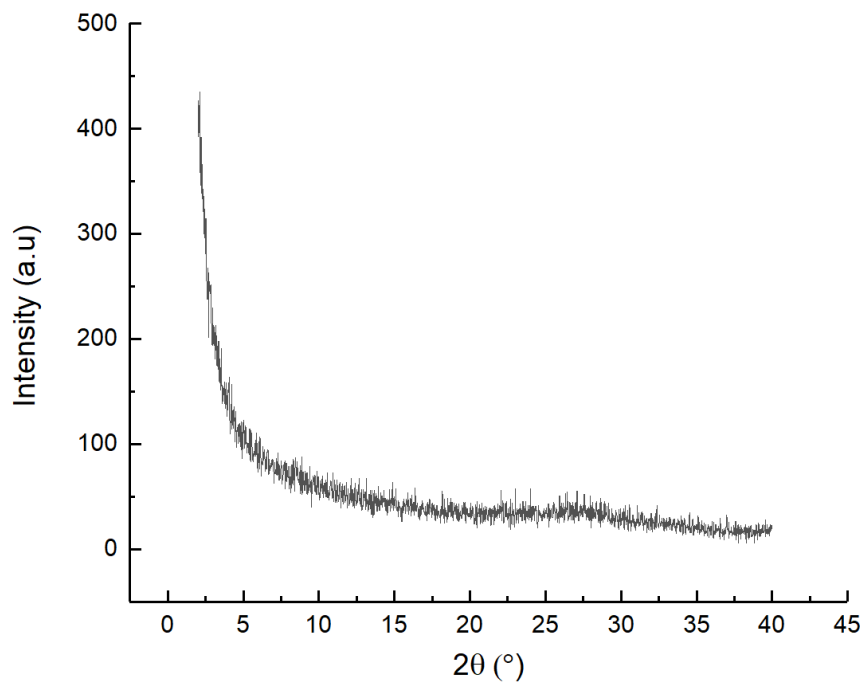


**Figure B- 1 PXRD pattern of sample from initial synthesis.**

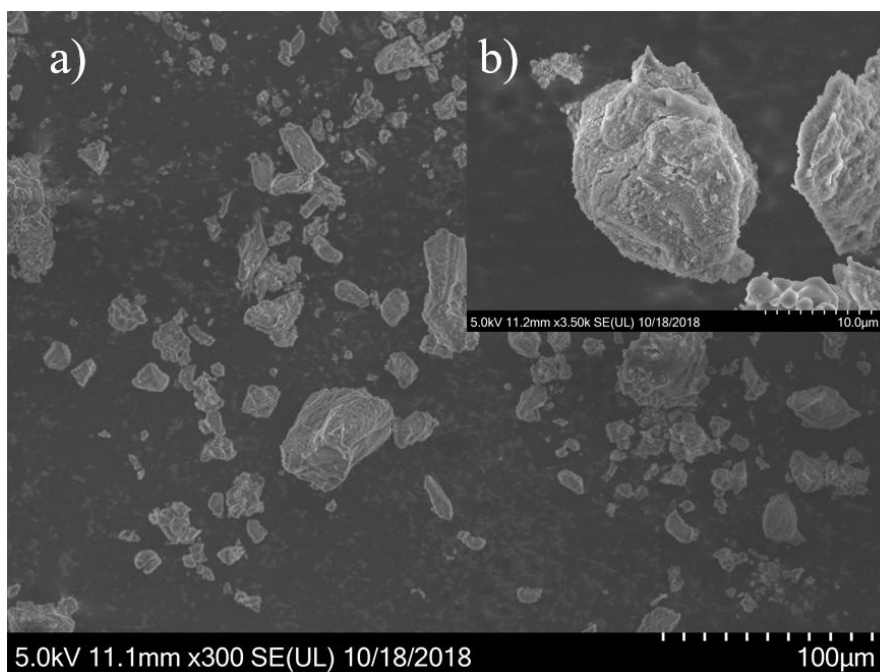


**Figure B- 2 SEM images of sample from initial synthesis. a) is in low magnification and b) is in high magnification.**

## Appendix C – Yield Calculations

The yield of the synthesis was estimated. This was done stepwise.

- i) The theoretical mass of TO<sub>2</sub> obtained after synthesis is calculated from the reactant masses in the synthesis mixture (Table C-1).

**Table C- 1 Calculation for the theoretical mass of TO<sub>2</sub> obtained from synthesis. The table includes chemical masses, with wt% considerations (Real mass), molar masses of reactants, calculated reactant moles, molar masses for the TO<sub>2</sub> elements and calculation of the theoretical mass of TO<sub>2</sub>.**

Chemicals	Mass weighed (g)	Real mass (g)	Molar mass(g/mole)	Moles reactant
Water	160,0	169,5	18,0	9,4
Aluminum isopropoxide 98 %	90,7	88,9	204,3	0,44
Phosphoric acid 85 %	51,3	43,6	98,0	0,44
Fumed silica	1,4	1,4	60,2	0,02

Elements	
<b>P</b>	31,0
<b>Si</b>	28,1
<b>Al</b>	27,0
<b>O</b>	16,0

Theoretical mass of TO <sub>2</sub>		
	T	O
mole	0,9	1,8
mass(g)	26,2	28,9
sum T+2*O (g)	55,1	

- ii) The total theoretical mass of the synthesis mixture is obtained by first calculating the mass of the synthesis mixture without the template and then with the template addition. (Table C-2)

**Table C- 2 Masses of synthesis mixture without and with template addition. Real mass is the reactant mass with wt% considerations.**

<b>Total Mass os synthesis mixture without template</b>		
Chemicals	Real Mass(g)	
water	169,5	
Aluminum isopropoxide	88,9	
Phosphoric acid	43,6	
Synthetic hydrated amorphous silica	1,4	
Total Mass without template	303,4	
<b>Total mass of synthesis mixture with addition of Template</b>		
Parts of synthesis mix	1/3Bottom	2/3Top
Mass (g)	101,1	202,3
Addition of DPA (g)	7,4	14,8
Sum mass (g)	108,5	217,1

The total mass of the entire mixture (mtotal synthesis mixture) is 325.6g

- iii) The theoretical dried product is calculated by Equation. C-1 and presented in Table C-3

$$\text{Dried product}_{\text{theoretical}} = \frac{mTO_2 \times \text{filling degree(g) in the liner}}{m_{\text{total synthesis mixture(g)}}} \quad (\text{C-1})$$

- iv) Yield is calculated by Equation.C-2 and presented in Table C-3

$$\text{Yield} = \frac{\text{Dried product}_{\text{Real}}}{\text{Dried product}_{\text{Theoretical}}} \times 100\% \quad (\text{C-2})$$

**Table C- 3 Yield of synthesis for the different sample presented in this thesis. Presented is the sample name, crystallization temperature filling degree (g) in liner, theoretical calculated mass of dried and real product and the yield in percent.**

Sample name	T <sub>crystal</sub> (°C)	Real filling in liner (g)	Theoretical product (g)	Real product(g)	Yield (%)
1-1/3Bottom _static	150	14,4	2,44	1,55	64
2-1/3 Bottom _static	160	20,7	3,50	3,20	91
3-1/3 Bottom _static	170	21,7	3,66	3,03	83
4-1/3 Bottom _static	180	18,7	3,16	2,40	76
1-2/3 Top _static	150	19,6	3,32	1,50	45
2-2/3 Top _static	160	20,4	3,45	2,03	59
3-2/3 Top _static	170	21,1	3,58	2,19	61
4-2/3 Top _static	180	18,7	3,16	2,70	85
1-1/3 Bottom _rotation	150	5,3	0,89	0,73	82
2-1/3 Bottom _rotation	160	5,3	0,90	0,54	60
3-1/3 Bottom _rotation	170	6,8	1,14	0,95	83
4-1/3 Bottom _rotation	180	7,3	1,24	0,80	65
1-2/3 Top _rotation	150	5,4	0,91	0,66	73
2-2/3 Top _rotation	160	5,5	0,93	0,78	84
3-2/3 Top _rotation	170	6,4	1,07	0,90	84
4-2/3 Top _rotation	180	6,4	1,09	0,75	69

## Appendix D – Reproducibility and impurities

The sample SAPO-11 4-1/3Bottom\_Static was reproduced two times with a different aluminum source purchased from Fluka. The reproduced PXRD data shows the presence of an impurity in the system. For rep 1 this occurs at 2theta angle of 5 and for rep 2 it occurs at 2theta angle of 8.7. The reproduced samples are measured in glass plate sample holders while the original sample is measured in a full plate sample holder. Due to the timescale of this thesis and low amounts of impurities observed, it was not further investigated.

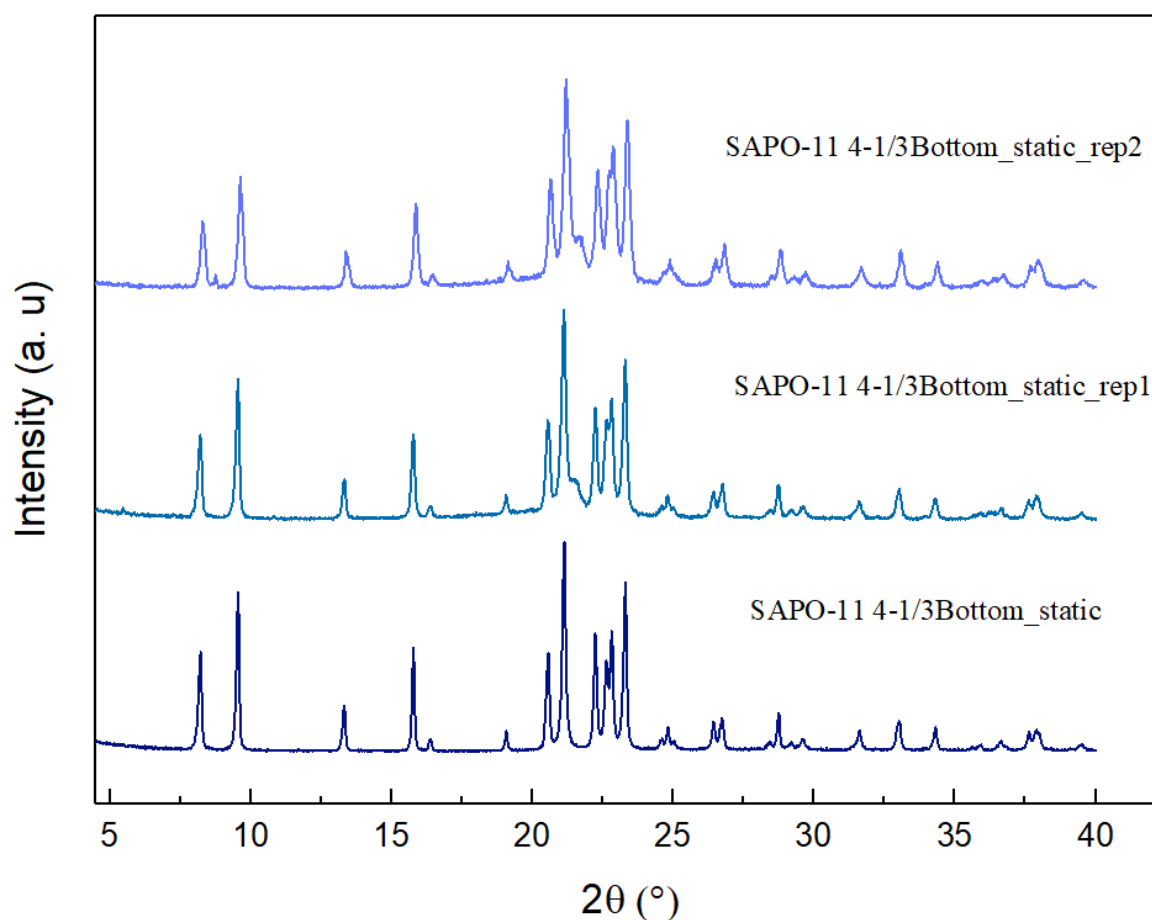


**Figure D- 1** PXRD for SAPO-11 4-1/3Top\_static and reproduced 1 and reproduced 2.

To validate that 20 counts per SAPO-11 aggregate are sufficient in the indication of average diameter size, 200 particles were calculated for the sample SAPO-11 4-1/3Bottom\_static and for the first reproduction. The average value of the diameter is 4.9  $\mu\text{m}$  for both and the standard deviation is 1.2 and 1.4. Figure D- 2 shows histograms for the original sample a) as well as for the reproduced sample b). The reproduced sample also contains a magnified image of impurity present in the system.

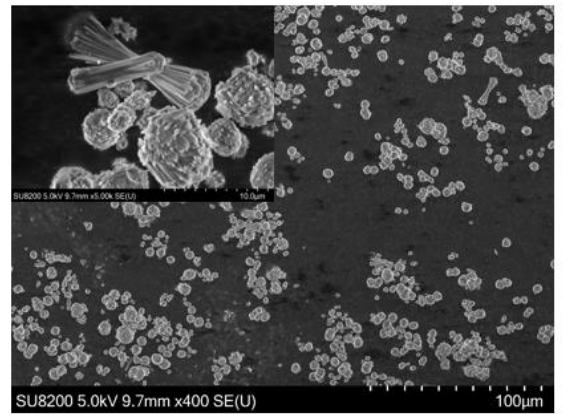
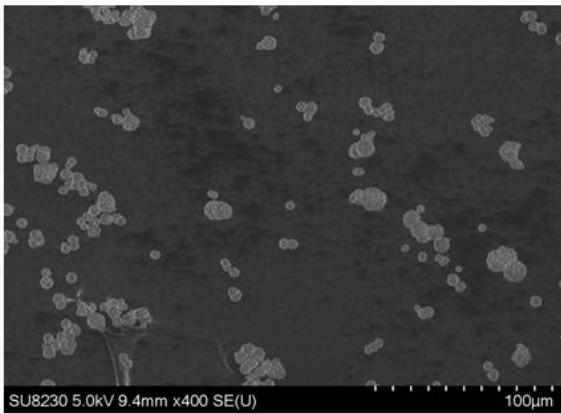
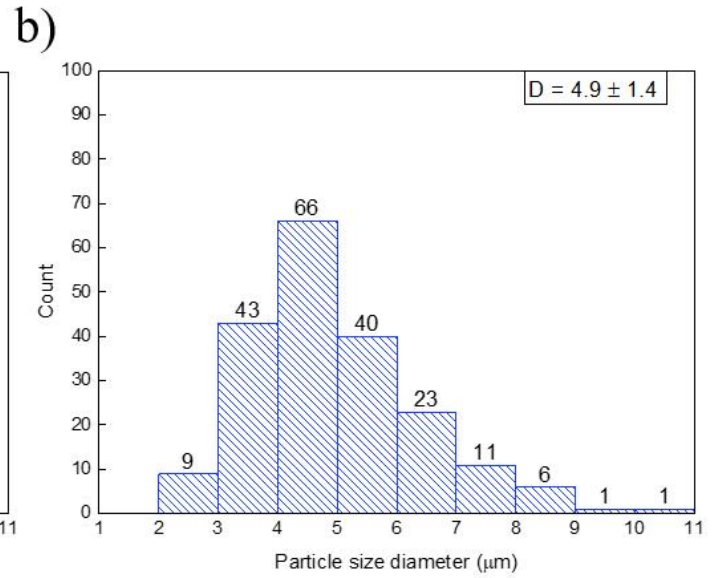
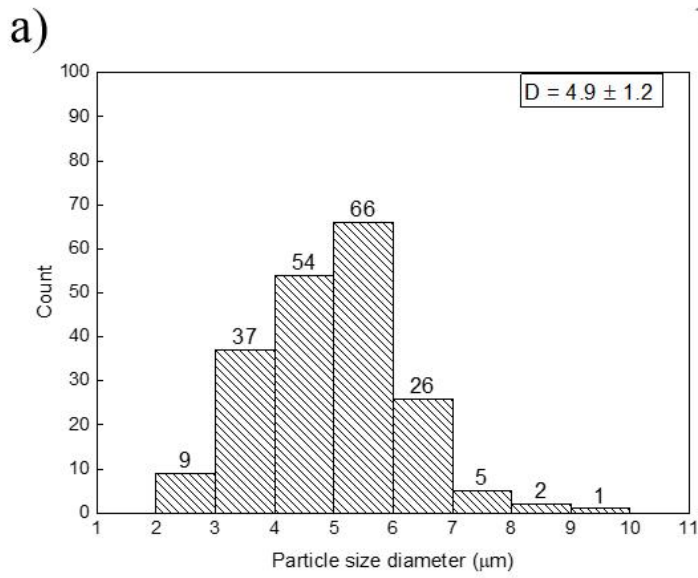


Figure D- 2 Size distribution for a) SAPO-11 4-1/3Bottom\_static and b) SAPO-11 4-1/3Bottom\_static reproduced 1. The size distributions is given with the average value of the aggregate diameter ( $\mu\text{m}$ ) and the standard deviation.

# References

1. Zhu Z, Hartmann M, Kevan L. Catalytic conversion of methanol to olefins on SAPO-n (n=11, 34, and 35), CrAPSO-n, and Cr-SAPO-n molecular sieves. *Chem Mat.* 2000;12(9):2781-7.
2. Miljødirektoratet. Olje- og gassvirksomheten er Norges økonomisk sett viktigste næring. Næringen er den største enkeltkilden til utslipp av klimagasser i Norge. 2019 [updated 25.06.2019. Available from: <https://miljostatus.miljodirektoratet.no/tema/hav-og-kyst/olje-og-gass/>.
3. IPCC. Special report: global warming of 1.5 °C [updated 05.10.19; cited 2019 05.09.19]. Available from: <https://www.ipcc.ch/sr15/chapter/spm/>.
4. Carbonengineering. Direct air capture [Available from: <https://carbonengineering.com/>.
5. Visconti CG, Martinelli M, Falbo L, Infantes-Molina A, Lietti L, Forzatti P, et al. CO<sub>2</sub> hydrogenation to lower olefins on a high surface area K-promoted bulk Fe-catalyst. *Applied Catalysis B: Environmental.* 2017;200:530-42.
6. Dang S, Gao P, Liu Z, Chen X, Yang C, Wang H, et al. Role of zirconium in direct CO<sub>2</sub> hydrogenation to lower olefins on oxide/zeolite bifunctional catalysts. *Journal of Catalysis.* 2018;364:382-93.
7. Zhao D, Wan Y, Zhou W. 1 - Introduction. *Ordered mesoporous materials.* Weinheim: John Wiley & Sons; 2012. p. 1-4.
8. McCusker L, Baerlocher C. Chapter 2 - Zeolite Structures. In: Čejka J, van Bekkum H, Corma A, Schüth F, editors. *Studies in Surface Science and Catalysis.* 168: Elsevier; 2007. p. 13-37.
9. Breck DW. Chapter One - Introduction. *Zeolite molecular sieves : structure, chemistry and use.* New York: Wiley; 1974. p. 1-19.
10. Smart LE, Moore EA. 7 - Zeolites and Related Structures. *Solid State Chemistry.* 3rd ed. London: CRC Press; 2005. p. 259-91.
11. Ma X-L, Lin JX-S. Chapter 24 - The Frontier of Inorganic synthesis and Preparative Chemistry(1)- Biomimetic Synthesis. In: Ruren Xu WP, Qisheng Huo, editor. *Modern Inorganic Synthetic Chemistry.* 2nd ed: Elsevier Science; 2010. p. 607-702.
12. Millini R, Bellussi G. Chapter 1 - Zeolite Science and Perspectives. In: Čejka J, Morris RE, Nachtigall P, Royal Society of C, editors. *Zeolites in catalysis : properties and applications.* 28. London: Royal Society of Chemistry; 2017. p. 1-28.
13. van Bekkum H, Flanigen EM, Jansen JC. Chapter 2- Zeolites and molecular sieves an historical perspective. *Studies in surface science and catalysis.* 58. Amsterdam: Elsevier; 1991. p. 39-104.
14. Association SCotIZ. Database of Zeolite Structures: The International Zeolite Association; 2018 [updated 10.04.19; cited 2019 05.06.19]. Available from: <http://europe.iza-structure.org/>.
15. Smeets S, Zou X. Chapter 2 - Zeolite Structures. In: Čejka J, Morris RE, Nachtigall P, Royal Society of C, editors. *Zeolites in catalysis : properties and applications* 28. London: Royal Society of Chemistry; 2017. p. 37-70.
16. Association SCotIZ. Zeolite Framework Types: The International Zeolite Association; 2017 [updated 10.04.19; cited 2019 06.06.19]. Available from: [http://europe.iza-structure.org/IZA-SC/ftc\\_table.php](http://europe.iza-structure.org/IZA-SC/ftc_table.php).

17. Flockhart BD, McLoughlin L, Pink RC. Evidence for the redox nature of zeolite catalysts. *Journal of Catalysis*. 1972;25(3):305-13.
18. Lyu Y, Liu Y, He X, Xu L, Liu X, Yan Z. The regulation of Si distribution and surface acidity of SAPO-11 molecular sieve. *Applied Surface Science*. 2018;453:350-7.
19. Forsido ST, Universitetet i Oslo Kjemisk i. Shape selective conversion of methanol to hydrocarbons over uni-dimensional 10-ring zeolites. Oslo: Department of Chemistry, Faculty of Mathematics and Natural Sciences, University of Oslo; 2013.
20. Rothenberg G. 1 - Introduction Catalysis: concepts and green applications: John Wiley & Sons; 2017. p. 43-85.
21. Rothenberg G. 2 - The basics of catalysis. *Catalysis: concepts and green applications*. 2nd ed: John Wiley & Sons; 2017. p. 1-41.
22. Chorkendorff I, Niemantsverdriet JW. Introduction to catalysis - 1. Concepts of modern catalysis and kinetics. Third, completely revised and enlarged edition. ed. Weinheim, Germany: Wiley-VCH; 2017.
23. Abdo S, Wilson S. Chapter 9 - Zeolites in industrial catalysis. In: Čejka J, Morris RE, Nachtigall P, Royal Society of C, editors. *Zeolites in catalysis : properties and applications* 28. London: Royal Society of Chemistry; 2017. p. 310-44.
24. Martens JA, Souverijns W, Verrelst W, Parton R, Froment GF, Jacobs PA. Selective Isomerization of Hydrocarbon Chains on External Surfaces of Zeolite Crystals. 1995;34(22):2528-30.
25. Blasco T, Chica A, Corma A, Murphy WJ, Agúndez-Rodríguez J, Pérez-Pariente J. Changing the Si distribution in SAPO-11 by synthesis with surfactants improves the hydroisomerization/dewaxing properties. *Journal of Catalysis*. 2006;242(1):153-61.
26. Wang J, Li J, Xu S, Zhi Y, Wei Y, He Y, et al. Methanol to hydrocarbons reaction over HZSM-22 and SAPO-11: Effect of catalyst acid strength on reaction and deactivation mechanism. *Chinese Journal of Catalysis*. 2015;36(8):1392-402.
27. Calvo F. Chapter 6 - Kinetic aspects: nucleation, mixing, coalescence. 2013. In: *Nanoalloys : from fundamentals to emergent applications* [Internet]. Amsterdam: Elsevier.
28. Cubillas P, Anderson M. Chapter 1 - Synthesis Mechanism: Crystal Growth and Nucleation. In: Čejka J, Corma A, Zones S, editors. *Zeolites and catalysis: synthesis, reactions and applications*: John Wiley & Sons; 2010. p. 1-50.
29. Smith RL, Cavka JH, Lind A, Akporiaye D, Attfield MP, Anderson MW. In-Situ Atomic Force Microscopy Study of the Dissolution of Nanoporous SAPO-34 and SAPO-18. *The Journal of Physical Chemistry C*. 2015;119(49):27580-7.
30. Anderson MW, Gebbie-Rayet JT, Hill AR, Farida N, Attfield MP, Cubillas P, et al. Predicting crystal growth via a unified kinetic three-dimensional partition model. *Nature*. 2017;544(7651).
31. Smart LE, Moore EA. 3 - Preparative methods. *Solid State Chemistry*. 3rd ed. London: CRC Press; 2005. p. 125-53.
32. Schubert U, Hüsing N. 4 - Formation of solids from solutions and melts. *Synthesis of inorganic materials*. 3rd compl. rev. and enl. ed. Weinheim: Wiley; 2012. p. 111-207.
33. McCusker LB, Baerlocher C. Chapter 2 - Zeolite structures. In: Čejka J, Bekkum VH, Corma A, Schüth F, editors. *Introduction to Zeolite Molecular Sieves*. 3rd ed. Burlington: Elsevier Science; 2007.
34. Zhang P, Liu H, Yue Y, Zhu H, Bao X. Direct synthesis of hierarchical SAPO-11 molecular sieve with enhanced hydroisomerization performance. *Fuel Processing Technology*. 2018;179:72-85.
35. Du Y, Feng B, Jiang Y, Yuan L, Huang K, Li J. Solvent-Free Synthesis and n-Hexadecane Hydroisomerization Performance of SAPO-11 Catalyst. *European Journal of Inorganic Chemistry*. 2018;2018(22):2599-606.



36. Liu Y, Lyu Y, Zhao X, Xu L, Mintova S, Yan Z, et al. Silicoaluminophosphate-11 (SAPO-11) molecular sieves synthesized via a grinding synthesis method. *Chem Commun.* 2018;54(78):10950-3.
37. Wu Q, Narthey Oduro I, Huang Y, Fang Y. Synthesis of hierarchical SAPO-11 via seeded crystallization. *Microporous and Mesoporous Materials.* 2015;218:24-32.
38. Liu M, Wu W, Kikhtyanin OV, Xiao L, Toktarev AV, Wang G, et al. Alkylation of naphthalene with methanol over SAPO-11 molecular sieve synthesized by different crystallization methods. *Microporous and Mesoporous Materials.* 2013;181:132-40.
39. Bing L, Tian P, Qi Y, Zhang L, Xu S, Su X, et al. Study of crystallization process of SAPO-11 molecular sieve. *Chin J Catal.* 2013;34(3):593-603.
40. Song C-M, Feng Y, Ma L-L. Characterization and hydroisomerization performance of SAPO-11 molecular sieves synthesized by dry gel conversion. *Microporous and Mesoporous Materials.* 2012;147(1):205-11.
41. Zhang S, Chen S-L, Dong P. Synthesis, Characterization and Hydroisomerization Performance of SAPO-11 Molecular Sieves with Caverns by Polymer Spheres. *Catalysis Letters.* 2010;136(1):126-33.
42. López CM, Escobar V, Arcos ME, De Nobrega L, Yáñez F, Garcia LV. Synthesis, characterization and catalytic behaviour of SAPO-11 obtained at low crystallization times and with low organic agent content. *Catalysis Today.* 2008;133(1-4):120-8.
43. Liu P, Ren J, Sun Y. Synthesis, characterization and catalytic properties of SAPO-11 with high silicon dispersion. *Catalysis Communications.* 2008;9(9):1804-9.
44. Zhang S, Chen S-L, Dong P, Yuan G, Xu K. Characterization and hydroisomerization performance of SAPO-11 molecular sieves synthesized in different media. *Applied Catalysis A, General.* 2007;332(1):46-55.
45. Zhang S, Chen S-L, Dong P, Ji Z, Zhao J, Xu K. Synthesis, characterization and hydroisomerization catalytic performance of nanosize SAPO-11 molecular sieves. *Catalysis Letters.* 2007;118(1):109-17.
46. Wang Z, Tian Z, Wen G, Teng F, Xu Y, Xu Z, et al. Synthesis and characterization of SAPO-11 molecular sieves from alcoholic systems. *Reaction Kinetics and Catalysis Letters.* 2006;88(1):81-8.
47. Hu Y, Wang X, Guo X, Sun H, Li S. Effect of the template on synthesis of SAPO-11 for hydroisomerization of n -octane. *Reaction Kinetics and Catalysis Letters.* 2005;86(1):45-50.
48. Walendziewski J, Pniak B. Synthesis, physicochemical properties and hydroisomerization activity of SAPO-11 based catalysts. *Applied Catalysis A, General.* 2003;250(1):39-47.
49. Sinha AK, Sainkar S, Sivasanker S. An improved method for the synthesis of the silicoaluminophosphate molecular sieves, SAPO-5, SAPO-11 and SAPO-31. *Microporous and Mesoporous Materials.* 1999;31(3):321-31.
50. Singh PS, Bandyopadhyay R, Rao BS. Characterization of SAPO-11 synthesized conventionally and in the presence of fluoride ions. *Journal of the Chemical Society, Faraday Transactions.* 1996;92(11):2017-26.
51. Lok BM, Messina CA, Patton RL, Gajek RT, Cannan TR, Flanigen EM, inventors; Union Carbide Corporation (Danbury, CT), assignee. Crystalline silicoaluminophosphates. United States 1984.
52. Leng Y. Chapter 2- X-ray Diffraction Methods. *Materials characterization: Introduction to microscopic and spectroscopic methods: Second edition.* 2nd ed 2013. p. 47-82.

53. Leng Y. Chapter 4 - Scanning electron Microscopy. *Materials characterization: Introduction to microscopic and spectroscopic methods: Second edition*. 2nd ed 2013. p. 127-59.
54. Jeol. Scanning Electron Microscope A to Z Tokyo: Jeol Ltd; [Available from: [https://www.jeol.co.jp/en/applications/pdf/sm/sem\\_atoz\\_all.pdf](https://www.jeol.co.jp/en/applications/pdf/sm/sem_atoz_all.pdf)].
55. Leng Y. Chapter 10 -Thermal analysis. *Materials characterization: Introduction to microscopic and spectroscopic methods: Second edition*. 2nd ed 2013. p. 353-60.
56. Yu L. Chapter 3 - Synthesis of zeolites. In: Čejka Jí, Bekkum VH, Corma A, Schüth F, editors. *Introduction to zeolite science and practice*. 168. 3rd ed. Amsterdam: Elsevier; 2007. p. 39-105.
57. Goel A. Chapter 1 - Surface chemistry. *Surface chemistry*. New Delhi: Discovery publishing house; 2006. p. 1-100.
58. Hesse M, Meier H, Zeeh B. 2 - Infrared and Raman spectroscopy. In: Enders D, Noyori R, Trost BM, editors. *Spectroscopic methods in organic chemistry*. Stuttgart: Thieme; 1997. p. 29-70.
59. Lercher JA, Jentys A. Chapter 13 - Infrared and raman spectroscopy for characterizing zeolites. In: Čejka Jí, Bekkum VH, Corma A, Schüth F, editors. *Introduction to zeolite science and practice*. 168. 3rd rev. ed. ed. Amsterdam: Elsevier; 2007. p. 435-77.
60. Hadjiivanov KI, Vayssilov GN. Characterization of oxide surfaces and zeolites by carbon monoxide as an IR probe molecule. 2002.
61. Datka J, Kozyra P, Kukulska-Zajac E, Szutiak M, Kumar N. The ir studies of the status of Cu + ions in CuZSM-5 CuBeta and in CuMCM-41. *Studies in Surface Science and Catalysis - STUD SURF SCI CATAL*. 2004;154:1655-60.
62. Otero Areán C, Turnes Palomino G, Escalona Platero E, Peñarroya Mentrut M. Zeolite-supported metal carbonyls: sensitive probes for infrared spectroscopic characterization of the zeolite surface. *Journal of the Chemical Society, Dalton Transactions*. 1997;0(5):873-80.
63. Technologies A. Microwave plasma atomic emission spectroscopy (MP-AES): Agilent Technologies; [updated 01.09.16. Available from: [https://www.agilent.com/cs/library/applications/5991-7282EN\\_MP-AES-eBook.pdf](https://www.agilent.com/cs/library/applications/5991-7282EN_MP-AES-eBook.pdf)].
64. Düren T, Millange F, Férey G, Walton KS, Snurr RQ. Calculating Geometric Surface Areas as a Characterization Tool for Metal–Organic Frameworks. *The Journal of Physical Chemistry C*. 2007;111(42):15350-6.
65. Möller K, Bein T. Mesoporosity a new dimension for zeolites. *Chem Soc Rev*. 2013;42(9):3689-707.
66. Pinilla-Herrero I, Olsbye U, Márquez-Álvarez C, Sastre E. Effect of framework topology of SAPO catalysts on selectivity and deactivation profile in the methanol-to-olefins reaction. *Journal of Catalysis*. 2017;352:191-207.
67. Pluth JJ, Smith JV, Richardson JW. Crystal structure of the as-synthesized precursor (MnAl<sub>9</sub>)P<sub>10</sub>O<sub>40</sub>.cndot.C<sub>6</sub>H<sub>16</sub>N to molecular sieve MnAPO-11. *The Journal of Physical Chemistry*. 1988;92(10):2734-8.
68. Toby BH. R factors in Rietveld analysis: How good is good enough? *Powder Diffraction*. 2006;21(1):67-70.
69. Sotomayor F, Cychosz K, Thommes M. *Characterization of Micro/Mesoporous Materials by Physisorption: Concepts and Case Studies*. 2018.
70. Bordiga S, Regli L, Cocina D, Lamberti C, Bjorgen M, Lillerud K. Assessing the acidity of high silica chabazite H-SSZ-13 by FTIR using CO as molecular probe: Comparison with H-SAPO-34. *J Phys Chem B*. 2005;109(7):2779-84.

71. Ugliengo P, Garrone E, Ferrari AM, Zecchina A, Arean CO. Quantum chemical calculations and experimental evidence for O-bonding of carbon monoxide to alkali metal cations in zeolites. *Journal of Physical Chemistry B*. 1999;103(23):4839.
72. Teketel S, Svelle S, Lillerud KP, Olsbye U. Shape-Selective Conversion of Methanol to Hydrocarbons Over 10-Ring Unidirectional-Channel Acidic H-ZSM-22. *ChemCatChem*. 2009;1(1):78-81.
73. Westgård Erichsen M, Svelle S, Olsbye U. The influence of catalyst acid strength on the methanol to hydrocarbons (MTH) reaction. *Catalysis Today*. 2013;215:216-23.
74. Campelo J, Lafont F, Marinas J, Ojeda M. Studies of catalyst deactivation in methanol conversion with high, medium and small pore silicoaluminophosphates. *Appl Catal A-Gen*. 2000;192(1):85-96.